N-05-68-1 • NOVEMBER 1968

N-05-68-1

THERMAL AND STRUCTURAL MODELING OF A LARGE APERTURE SPACE TELESCOPE

FACILITY FORM 602

N69-16957
(ACCESSION NUMBER)

293
(PAGES)

CR 98241
(NASA CR OR TMX OR AD NUMBER)

(THRU)

(CODE)

3
(CATEGORY)



Lockheed

PALO ALTO RESEARCH LABORATORY

LOCKHEED MISSILES & SPACE COMPANY • A GROUP DIVISION OF LOCKHEED AIRCRAFT CORPORATION
PALO ALTO, CALIFORNIA

November 1968

Technical Summary Report for Period

22 June 1968 to 22 September 1968

THERMAL AND STRUCTURAL MODELING OF A LARGE APERTURE SPACE TELESCOPE

NAS 8-20411

By

R. E. Rolling

K. N. Marshall

D. O. Murray

Aerospace Sciences Laboratory
Lockheed Palo Alto Research Laboratory
LOCKHEED MISSILES & SPACE COMPANY
A Group Division of Lockheed Aircraft Corporation
Palo Alto, California

PRECEDING PAGE BLANK NOT FILMED.

FOREWORD

This report was prepared by the Lockheed Palo Alto Research Laboratory of Lockheed Missiles & Space Company, for George C. Marshall Space Flight Center of the National Aeronautics and Space Administration. The work was performed under Contract NAS 8-20411 and was administered by the Space Sciences Laboratory of Marshall Space Flight Center, with Mr. B. P. Jones as contract officer's technical representative.

The Technical Summary Report describes work performed from 22 June 1966 to 22 September 1968.

PRECEDING PAGE BLANK NOT FILMED.

CONTENTS

Section		Page
	FOREWORD	iii
	ILLUSTRATIONS	vii
	TABLES	xi
1	INTRODUCTION	1-1
2	PROTOTYPE DESIGN	2-1
3	THERMAL ANALYSES	3-1
	3.1 Introduction	3-1
	3.2 Node and Properties Selection	3-2
	3.3 Thermal Properties	3-11
	3.4 Mathematical Analysis	3-11
4	THERMAL MODELING OF THE OTES MULTILAYER INSULATION SYSTEM	4-1
	4.1 Introduction	4-1
	4.2 Approach	4-2
	4.3 Description of Insulation Test Models	4-6
	4.3.1 Test Configuration 1	4-7
	4.3.2 Test Configuration 2	4-17
	4.3.3 Test Configuration 3	4-17
	4.3.4 Test Configuration 4	4-19
	4.4 Test Program	4-25
	4.4.1 Chamber Installation	4-25
	4.4.2 Energy Sources	4-25
	4.4.3 Instrumentation	4-27
	4.4.4 Test Procedures	4-29
	4.5 One-Dimensional Heat Flow Test Results	4-35
	4.5.1 Configuration 1 Test Results	4-35

Section		Page
	4.5.2 Configuration 3 Test Results	4-39
	4.5.3 Configuration 4 Test Results	4-43
	4.5.4 Insulation Design for the 1/6.43-Scale Model	4-48
	4.6 Transient Performance Test Results	4-50
	4.7 Conclusions	4-62
5	TELESCOPE MODEL	5-1
	5.1 Modeling Criteria	5-1
	5.2 Model Design	5-5
	5.2.1 Primary Mirror Design	5-6
	5.2.2 Secondary Mirror Support Rod Design	5-9
	5.2.3 Multilayer Insulation	5-11
	5.2.4 Manned Support Structure Interface	5-15
	5.2.5 Surface Coatings	5-16
	5.3 Model Fabrication Assembly	5-16
	5.3.1 Model Instrumentation	5-19
	5.3.2 Chamber Installation	5-22
	5.4 Control and Readout Instrumentation	5-26
	5.4.1 Test Operation	5-27
	5.5 Results	5-27
6	DISCUSSION	6-1
7	CONCLUSIONS	7-1
8	REFERENCES	8-1
Appendix		
A	TABULAR RESULTS	A-1

ILLUSTRATIONS

Figure		Page
1	Two-Meter OTES Concept	2-3
2	Thermal Expansion of Fused Quartz	2-4
3	Two-Meter Telescope Thermal Design	2-6
4	Two-Meter Telescope Model Node Definition	3-3
5	Node Designation, Barrel Section A (+Z to Earth)	3-4
6	Node Designation, Barrel Section B (+Z to Earth)	3-4
7	Node Designation, Barrel Section C (+Z to Earth)	3-5
8	Node Designation, Barrel Section D (+Z to Earth)	3-5
9	Node Designation, Barrel Section E (+Z to Earth)	3-6
10	Node Designation, Barrel Section F (+Z to Earth)	3-6
11	Node Designation, Barrel Section H (+Z to Earth)	3-7
12	Node Designation, Primary Mirror (+Z to Earth)	3-8
13	Node Designation, Manned/Experiment Section	3-9
14	Typical Conduction and Radiation Coupling, Zone A to Zone H	3-10
15	Selected Orbital Configuration	3-15
16	Analytically Predicted Transient Thermal Behavior Section A	3-17
17	Analytically Predicted Transient Thermal Behavior Section B	3-17
18	Analytically Predicted Transient Thermal Behavior Section C	3-18
19	Analytically Predicted Transient Thermal Behavior Section D and Primary Mirror	3-18
20	Configuration 1: One-Dimensional Test Arrangement	4-8
21	Configuration 1: Transient Test Arrangement	4-8
22	Chamber Ins llation of Full-Scale Insulation Test Object	4-11
23	Interior of Full-Scale Insulation Test Object	4-12
24	Detail of Insulation Button Attachment Method	4-13
25	Detail of Multilayer Insulation Axial Overlap Joint	4-15

Figure		Page
26	Detail of Multilayer Insulation Circumferential Overlap Joint	4-15
27	Configuration 3: One-Dimensional Test Arrangement	4-18
28	Configuration 3: Transient Test Arrangement	4-18
29	One-Half Scale Model – Transient Test Arrangement	4-22
30	End View of Half-Scale Model's One-Dimensional Test Arrangement	4-23
31	Chamber Installation of the Half-Scale Model's One-Dimensional Test Arrangement	4-24
32	Section A Lamp Bank Location	4-26
33	Thermocouple Locations for System Performance Tests	4-28
34	Section A Temperature Distributions, °K	4-34
35	Test Configuration 1; Exterior Temperatures for One-Dimensional Heat Flow Test	4-37
36	Comparison of Exterior Temperatures for One-Dimensional Heat Flow – Test Configurations 1 and 3	4-40
37	Insulation Thermal Conductivities for the Full-Scale Interior and Exterior Wraps	4-42
38	Comparison of Exterior Temperatures for One-Dimensional Heat Flow – Test Configurations 3 and 4	4-45
39	Insulation Thermal Conductivities for the Full- and Half-Scale Interior Wraps	4-47
40	Correlation of Internal Temperatures for One-Dimensional Heat Flow; Test Configurations 3 and 4	4-47
41	Configuration 1 Transient Temperatures; Section A Cycled and Top Exterior of Sections B, C, and D Subjected to Average Heat Flux	4-51
42	Configuration 2 Transient Temperatures; Section A Cycled and Top Exterior of Sections B, C, and D Subjected to Average Heat Flux	4-52
43	Configuration 3 Transient Temperatures; Section A Cycled and Top Exterior of Sections B, C, and D Subjected to Average Heat Flux	4-53
44	Configuration 4 Transient Temperatures; Section A Cycled and Top Exterior of Sections B, C, and D Subjected to Average Heat Flux	4-54

Figure		Page
45	Configuration 1 Transient Temperatures; Top Exterior of Sections B, C, and D Cycled and Section A Held at Fixed Average Temperature	4-58
46	Configuration 2 Transient Temperatures; Top Exterior of Sections B, C, and D Cycled and Section A Held at Fixed Average Temperature	4-59
47	Configuration 3 Transient Temperatures; Top Exterior of Sections B, C, and D Cycled and Section A Held at Fixed Average Temperature	4-60
48	Configuration 4 Transient Temperatures; Top Exterior of Sections B, C, and D Cycled and Section A Held at Fixed Average Temperature	4-61
49	Model Primary Mirror	5-8
50	Thermal Expansion of Pyrex	5-12
51	Model Geometry	5-17
52	Primary Mirror Suspension	5-18
53	Model Thermocouple Locations	5-20
54	Primary Mirror Thermocouples	5-21
55	Assembled Optical System	5-23
56	Optical System, Lamp Bank Arrays, and Movable Shutter System	5-24
57	Assembled Model Prior to Test	5-25
58	Transient Thermal Behavior Section A	5-28
59	Transient Thermal Behavior Section B	5-30
60	Transient Thermal Behavior Section C	5-31
61	Transient Thermal Behavior Section D and Primary Mirror	5-32
62	Temperature History for Prototype Primary Mirror Surrounds	5-33
63	Temperature History for Prototype Secondary Support Rods	5-34
64	Thermal Expansion of Model Secondary Support Rods	5-34

PRECEDING PAGE BLANK NOT FILMED.

TABLES

Table		Page
1	Thermal Properties	3-11
2	Orbit Average Temperature Predictions Temperature, °K	3-16
3	Instrumentation for Insulation Experiments	4-30
4	Internal Power Dissipation for One-Dimensional Tests	4-32
5	Test Conditions for Transient Performance Tests	4-33
6	Summary of One-Dimensional Test Results for Configuration 1	4-39
7	Summary of One-Dimensional Test Results for Configuration 3	4-41
8	Comparison of Measured and Calculated Thermal Conductivity Model Ratios (K*)	4-44
9	Summary of One-Dimensional Test Results Half-Scale Insulation Model (Configuration 4)	4-46
10	Modeling Results for Section A Cycled and Top Exterior at Constant Heat Flux	4-63
11	Modeling Results for Top Exterior Cycled and Section A at Constant Heat Flux	4-64
12	Structural Scaling Laws	5-5
13	Properties of Pyrex and Fused Quartz	5-7
14	Prototype Primary Mirror Temperature History Temperature – °K	5-

Section 1
INTRODUCTION

This report covers work performed during a basic analytical and experimental program on the use of thermal-structural similitude for studies of prototype behavior in the space environment. The work reported herein was supported by the Space Sciences Laboratory, Marshall Space Flight Center, National Aeronautics and Space Administration, Huntsville, Alabama.

Previous studies of thermal similitude (Ref. 1), which were fundamental to the work reported herein, provided experimental evidence that the utilization of thermal modeling techniques held considerable promise as a tool for studies of thermal behavior in the space environment. The most important conclusion reached during that program, which consisted of experimental work on simple geometries, was that thermal models could be constructed of available structural materials for purposes of predicting both the steady-state and transient thermal response of space vehicles. The accuracies of model predictions were forecast to be within the bounds of experimental error or on the order of 1/2 to 1% of the absolute temperature of the flight item. The considerable benefits to be gained by the use of modeling techniques are further substantiated by the results of other workers (Refs. 2–10) who have reported their observations in this respect.

The objective of this program was to further study the utility of thermal modeling for the prediction of thermal performance of spacecraft and, if possible, extend the scope of the study to include considerations of structural performance. To meet this objective required the selection of an existing or planned prototype item whose thermal and structural performance would pose an interesting problem in terms of the program scope.

A preliminary review of planned flight programs resulted in the selection of space telescopes as the most promising class of hardware for use in this study. The geometry, size, and influence of thermal distortions on performance were all considered appropriate in terms of satisfying the stated objectives. A more thorough study of planned optical technology experiments led to the selection of the proposed 2-meter aperture OTES (Optical Technology Apollo Extension System) telescope. The prototype telescope would have an overall length of 12 meters (39.4 ft), tube aperture of 2.38 meters (7.75 ft), and could be accommodated, when properly scaled, within the available test facility. The prototype space environment would be that experienced by a flight object in a 24-hr synchronous orbit.

This report presents the results of an analytical and experimental study of thermal and structural modeling of the 2-meter OTES concept. A thermal analysis was performed with two objectives in mind. The first was to establish predictions of the flight thermal performance for use in establishing required modeling conditions. The second was to clarify the relative importance of certain thermal design parameters such as insulation quality, structural member conductances, thermal control coating surface properties, and sun shutter operating conditions. The required information was obtained by establishment of a detailed thermal-analyzer program based upon the conceptual design of the telescope. Numerous assumptions were necessary for completion of the analytical work due to the fact that actual hardware design had not yet been initiated. Results of the analysis and the assumptions required are presented in Section 3. A major conclusion reached during the analytical work was that passive thermal control techniques were sufficient to provide required absolute temperature levels and to reduce temperature differences in the primary mirror to $\pm 1°K$.

The overall study required the expenditure of considerable effort to establish acceptable techniques for thermal modeling of high performance multilayer insulation. This material was proposed as an inner liner on the interior of the telescope tube for purposes of damping out external thermal transients and maintenance of uniform temperatures in the primary optic. In view of the prototype size as compared to the available test chamber size, it was apparent that a scale ratio between one-fifth and

one-sixth would be necessary for model construction. It would also be necessary to use a temperature ratio greater than unity for the study since predicted prototype temperatures were very low and could not be achieved using a chamber whose thermal background would be provided by liquid nitrogen cooled walls. The small-scale ratio and necessary increased temperature ratio introduced considerable doubt concerning the procedures to be used to accurately model the multilayer insulation. While the properties of this material (alternate layers of aluminized mylar and dexiglass) have received considerable attention by the Aerospace Industry for purposes of hardware design, very little information was available to guide the selection of an appropriate wrap for use on the model. As a result, a considerable effort was devoted to studying the problem of modeling multilayer insulation under steady state and transient conditions. A wrap identical to that proposed for the 2-meter OTES telescope was constructed and tested under steady state and transient conditions and was then modeled to half scale under similar conditions. The results obtained from the study are presented in Section 4. The major conclusions reached were that criteria can be established for accurate modeling of the perpendicular thermal conductivity of multilayer insulation at a decreased length ratio and increased temperature ratio using identical materials. However, the procedures necessitate considerable geometric distortion, i.e., the number of layers are not decreased according to the length ratio, so that three-dimensional modeling is not achieved. Likewise, since the thermal diffusivity remains the same in materials preservation, the selection of a desired time constant is not possible concurrent with selection of a desired thermal conductivity.

The results obtained from the thermal analysis and multilayer insulation study led to a model design having a length scale ratio of 1/6.42 and absolute temperature ratio of 1/1.86. The model was constructed, instrumented for the determination of thermal and structural performance, and tested under a simulated synchronous orbit. The results of the model tests are presented in Section 5 along with comparisons to the analytical predictions. It was found that the model tests compared favorably with the analytical predictions and reinforced the premise that passive thermal control techniques would be sufficient for thermal control of the telescope interiors.

Agreement between the analytical predictions and model predictions was generally good. The model results forecast a lower average interior temperature than the analytical results while predicted transient variations about the mean were nearly identical. Differences between the model and analytical results were attributed partially to differences in input energy from the tube aperture; however, this could not be established as the sole reason for differences in predicted performance.

Completion of the overall study effort established the feasibility of using small-scale thermal models for prediction of the thermal and structural behavior of large aperture telescope systems in a space thermal environment. The benefits to be gained from the model are that the system lends itself to direct physical measurement of the thermal response of critical components providing more detailed results than are available from analytical methods. The variety of tests that can be performed on a working model offer the thermal designer maximum flexibility in thermal performance studies and permit immediate experimental observations of the influence of proposed design changes.

The effort required to design and construct the model depends considerably upon the input available from the prototype design activity. If the prototype design and thermal analyses are nearly complete, then all inputs required for model design will be available and the overall model effort considerably reduced. Such was not the case during the present study since prototype design activity was in early stages of development. Under these circumstances the model study must assume much of the work normally associated with prototype design and the required total effort is considerably expanded.

Section 2
PROTOTYPE DESIGN

Completion of the program objectives outlined in Section 1 required the selection of a telescope system whose design was sufficiently finalized to provide the needed information on thermal and structural design. A number of programs were reviewed in terms of their potential use in the modeling effort. The designs that were deemed most appropriate for detailed study included a modified GEP (Goddard Experiment Package) in a configuration referred to as the OAP (Optical Astronomy Package) for use in the Apollo Extension System and three configurations under consideration by NASA for use in the proposed OTES (Optical Technology Apollo Extension System) program.

The OAP conceptual design consisted of a 0.965-meter aperture reflective telescope and associated instrumentation for spectral dispersion and detection of incoming energy. This system was proposed for installation on top of the LEM shelter in an altitude-azimuth mount. Astronomical observations would be performed from the lunar surface. Studies of this system for use in the modeling program led to the determination that its geometry would be appropriate. However, the conceptual design of the system was not sufficiently developed to permit a sufficiently detailed thermal analysis of the system for use as an input to the design of a thermal model. Therefore, consideration of the system was discontinued.

The three OTES (Ref. 11) concepts under consideration consisted of a 1-meter aperture telescope integrated with the LEM Lab, a totally contained 2-meter aperture system, with limited manned capability, and a 3-meter aperture system with extended manned capabilities. The small size of the 1-meter system was considered a substantial drawback to its utilization in the model study. Furthermore, it appeared that the larger systems held more promise of being carried to the hardware phase where comparisons might be made between model observations and flight performance.

A detailed thermal analysis was made of the 3-meter concept both for purposes of determining its thermal performance and for evaluating its utility as a prototype system in the model study. The thermal analysis was carried to near completion at which time it was discovered that a decision had been made by the OTES program office to redirect their effort so that all future work would be on the 2-meter concept. In accord with this decision, the model study was changed to an evaluation of the 2-meter concept and a decision made to freeze on the conceptual design in existence at that time.

At the date of this report, the 2-meter OTES concept differs considerably from the design concept used in the modeling program. Numerous improvements have been made in the design as a result of additional studies. However, the present and past concepts are sufficiently similar in geometry and orbital environment to permit useful comparisons between the results reported herein and the anticipated performance of the latest design concept.

The 2-meter system used for this program is shown schematically in Fig. 1. The telescope consists of a 2-meter diameter active optical segment primary mirror arranged in a hexagonal array of 3 regular hexagonal segments. The system provides a Cassegranian f/3 parabolic telescope. The secondary optic is mounted on a supporting system at a distance of approximately 4.76 meters (187 in.) from the primary and is maintained at that distance by 3 quartz spacer rods which also furnish the required structural support during the orbital mission. The telescope barrel consists of five multilayer insulated aluminum honeycomb cylinders and one plastic honeycomb cylinder at the barrel opening. Each cylindrical section collapses over its neighbor toward the primary mirror to minimize volume during the launch phase. The secondary mirror quartz spacer rods are also collapsed and stored during launch. After injection into a 24-hr synchronous orbit, the telescope is erected and placed into operation by a crew of astronauts who dock with the telescope manned support section utilizing a LEM vehicle.

Optimum thermal-optical performance of the telescope requires minimal thermal gradients in the optics, particularly in the primary mirror segments, elimination of

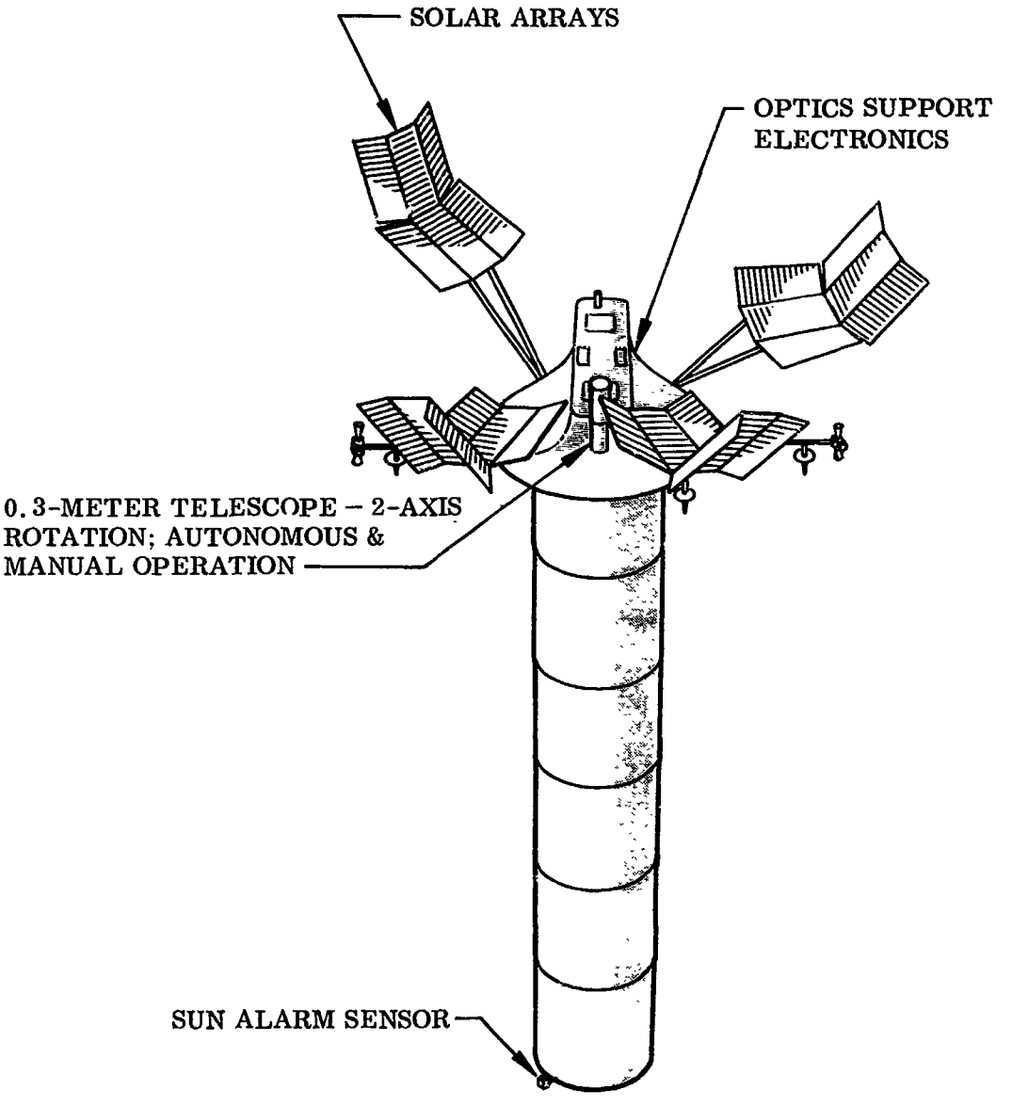


Fig. 1 Two-Meter OTES Concept

thermal transients imposed by the varying thermal inputs during orbit, and an average steady-state temperature near the inversion point of the thermal expansion of fused quartz. The thermal expansion of fused silica (Corning 7940) is shown in Fig. 2 where it can be seen that the coefficient of thermal expansion will be zero at a temperature near 150°K. The benefit of maintaining primary mirror temperatures near this zero expansion point is obvious.

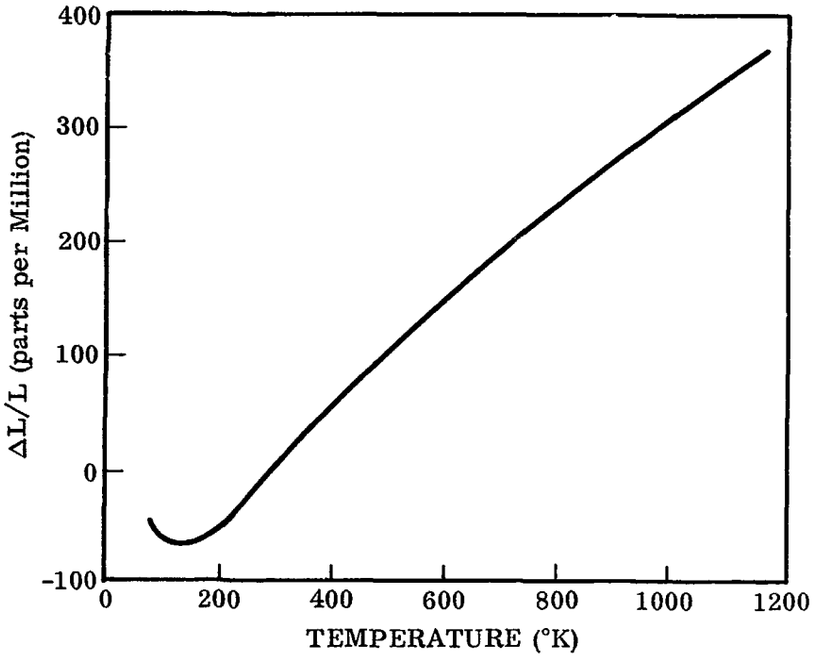


Fig. 2 Thermal Expansion of Fused Quartz

Preliminary thermal design studies, supported by the OTES program office, resulted in a thermal design that could provide near optimal thermal conditions through utilization of passive thermal control techniques in combination with an active sun shutter at the tube opening. The shutter would control the amount of direct solar illumination of the telescope interior.

The thermal requirements were met by use of the following materials and thermal control surfaces (Fig. 3):

(1) The front cylindrical element would be of 2.54-cm (1-in.) thick plastic honeycomb and would mount the sun shutter. The sun shutter would activate in such a manner that direct solar energy could not strike the inner surface of the adjacent cylindrical section.

(2) The remaining five cylindrical sections would consist of 1.27-cm (1/2-in.) thick aluminum honeycomb and would be insulated on the interior with 1.27 cm (1/2 in.) of high performance multilayer insulation.

(3) All exterior surfaces of the telescope tube and mounting platform would be covered with an optical solar reflector (OSR) material having a solar absorptance of 0.05 and infrared emittance of 0.80.

(4) All interior surfaces would be coated with a highly diffuse optical black paint with the exception of the primary mirror and a band of the surrounding telescope tube immediately adjacent to it, surfaces of the primary mirror mounting platform on the telescope interior, and the reflecting surface of the secondary mirror.

(5) Interior surfaces not coated with black paint would be first-surface aluminum.

Unfortunately, no information was available during the thermal study on a final design of the primary mirror active mount with the exception that it would provide 3 degrees of freedom for independent adjustment of focus for each of the three segments. Therefore, it was necessary to make the assumption that the mounts would effectively support the mirrors and at the same time provide conductive isolation from the mounting plate.

In addition, the mechanisms required to support adjacent sections of the telescope tube were not well defined, requiring the assumption that each section would be, within reason, conductively isolated from its neighbor.

The proposed telescope would be placed in a 24-hr synchronous orbit and be utilized in both an earth-oriented and a space-oriented configuration. These orientations result

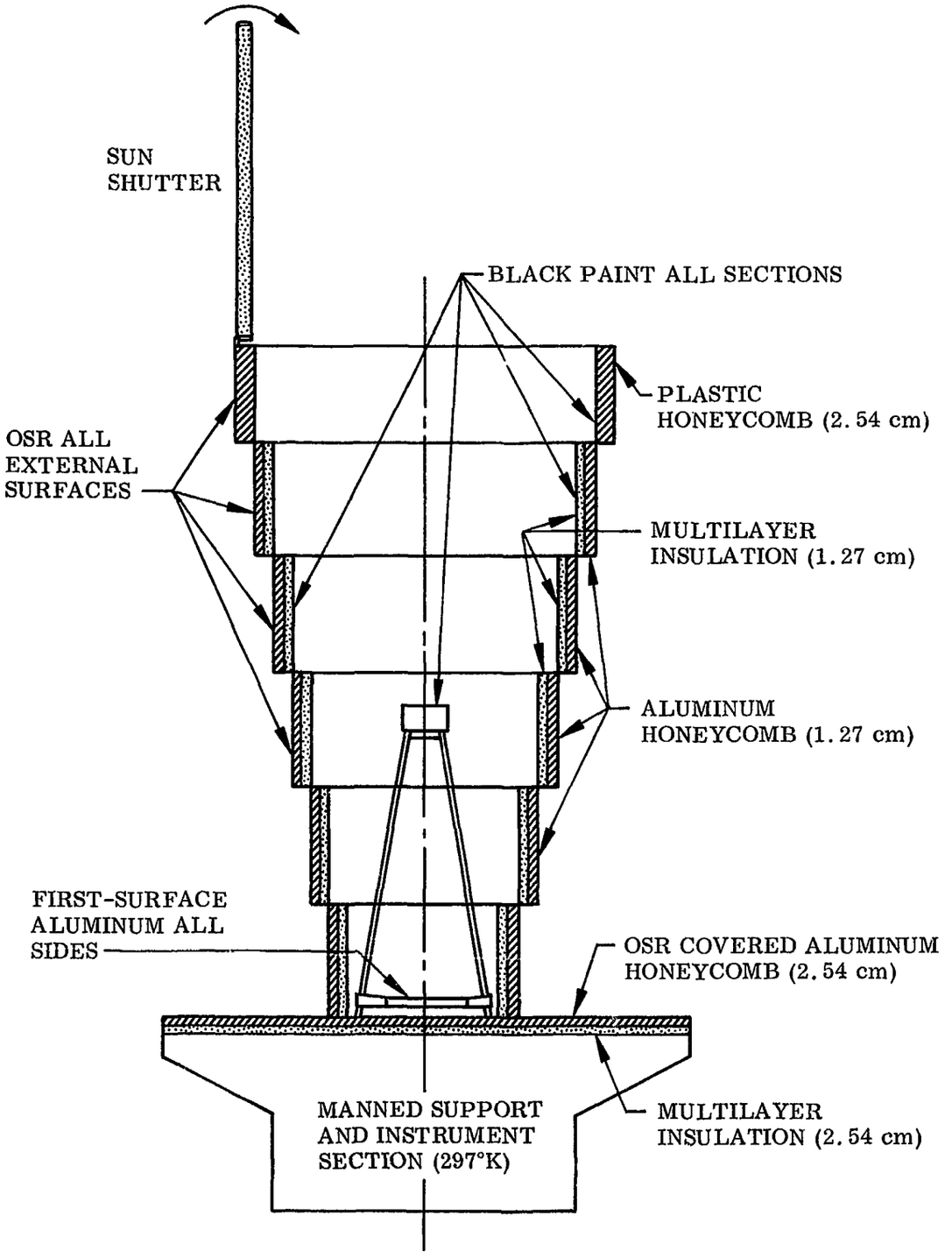


Fig. 3 Two-Meter Telescope Thermal Design

in entirely different thermal responses due to the differences in solar illumination of the exterior and interior surfaces, and operation or lack of operation of the sun shutter. A thermal analysis was performed on the 2-meter system for both orientations for purposes of assisting in the design of a thermal model. The analysis is described in Section 3.

Section 3

THERMAL ANALYSES

3.1 INTRODUCTION

A comprehensive thermal analysis was performed for purposes of predicting the space thermal behavior of the selected 2-meter telescope conceptual design. This study resulted in the creation of an electrical-analog mathematical model containing the influences of all important radiation and conduction heat flow paths and heat storage elements of the telescope.

The mathematical model included the influence of the multilayer insulated tube, the three-segment primary mirror, the secondary mirror and its support structure, the interface between the manned support structure and telescope interior, and the sun shutter.

During development of the mathematical model, it was necessary to establish numerous estimates of actual prototype thermal conditions since the conceptual design had not proceeded sufficiently to definitize all aspects of its construction. The most important of the necessary assumptions were:

(1) Edges of the multilayer insulation were assumed adiabatic.
(2) The primary mirror segments were assumed to be aluminized on all surfaces and to be conductively isolated from each other and from the manned support structure.
(3) The quartz secondary mirror support rods were assumed to be continuous.
(4) The sun shutter was assumed to provide an adiabatic wall when closed.
(5) The manned support structure mounting platform was assumed to be maintained at an invariant temperature of 298°K (75°F).
(6) For simplification, all thermal properties selected for use in the analyses were assumed constant and independent of temperature.

3.2 NODE AND PROPERTIES SELECTION

The telescope was separated into 10 major sections as indicated in Fig. 4. Each cylindrical section was broken into 24 individual nodes as shown in Figs. 5 through 13. A general description of the geometries and properties assumed for the analyses of each section follows.

- Barrel. All sections except Section A have an external layer of 1.27-cm (0.5-in.) thick aluminum honeycomb and an internal layer of 1.27-cm-thick multilayer insulation. Section A is composed of a plastic honeycomb material 2.54-cm (1.0-in.) thick.
- Mirror Section. The mirror is composed of fused quartz glass having the special property of a near-zero thermal expansion coefficient at approximately 150°K. It is a cylindrical body with a paraboloid (f/d = 3.0, diameter = 2.0 meters) contoured onto its upper surface and is assumed to have been cut into three pie-shaped sections.
- Manned Experiment Section. This section is simulated by a 3.30-meter-diameter disc. The disc is made of a 1.27-cm (0.5-in.) thick aluminum honeycomb with a backing of 2.54 cm of multilayer insulation.
- Barrel to Disc Support Members. Support members to connect the barrel to the disc were assumed to be spaced at 12 equiangular positions. The members would be made of a nylon/plastic material and were assumed to be covered with OSR material.
- Quartz Rod/Secondary Optics System. This system consists of three quartz rods running between the primary and secondary mirrors. They are attached firmly to the primary mirror mounting plate and to the secondary mirror platform. The secondary mirror, which is 0.368 meters (1.44 ft) in diameter and 5.08-cm (2-in.) thick, is located at a point 3.95 meters (15.6 ft) from the vertex of the primary mirror.
- Nodal Breakdown. The nodes indicated in Figs. 5 through 13 were interconnected in the radiation-conduction network in a manner similar to that demonstrated by Fig. 14 which shows the connections for a single vertical strip of the telescope.

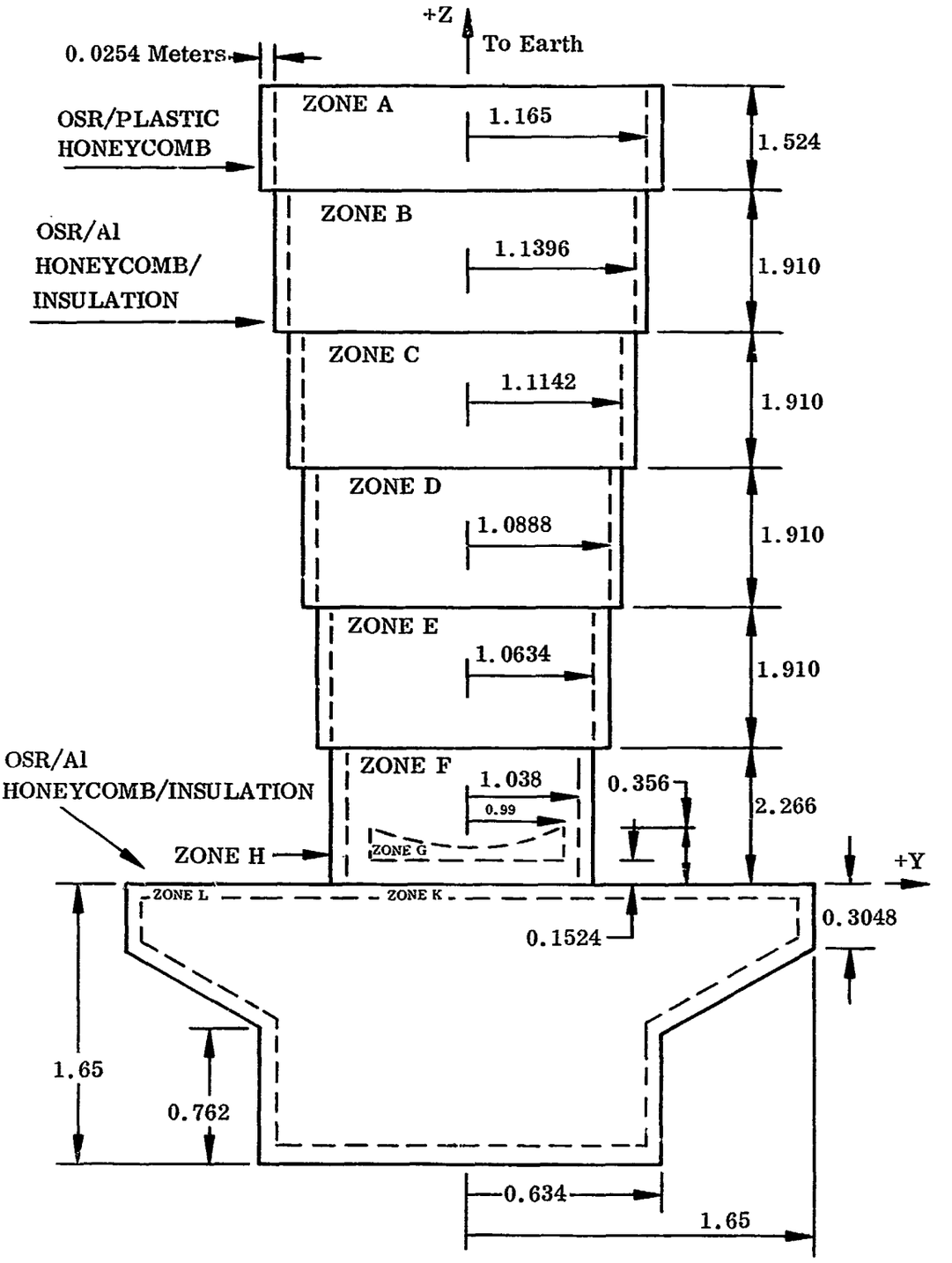


Fig. 4 Two-Meter Telescope Model Zone Definition. (All dimensions in meters)

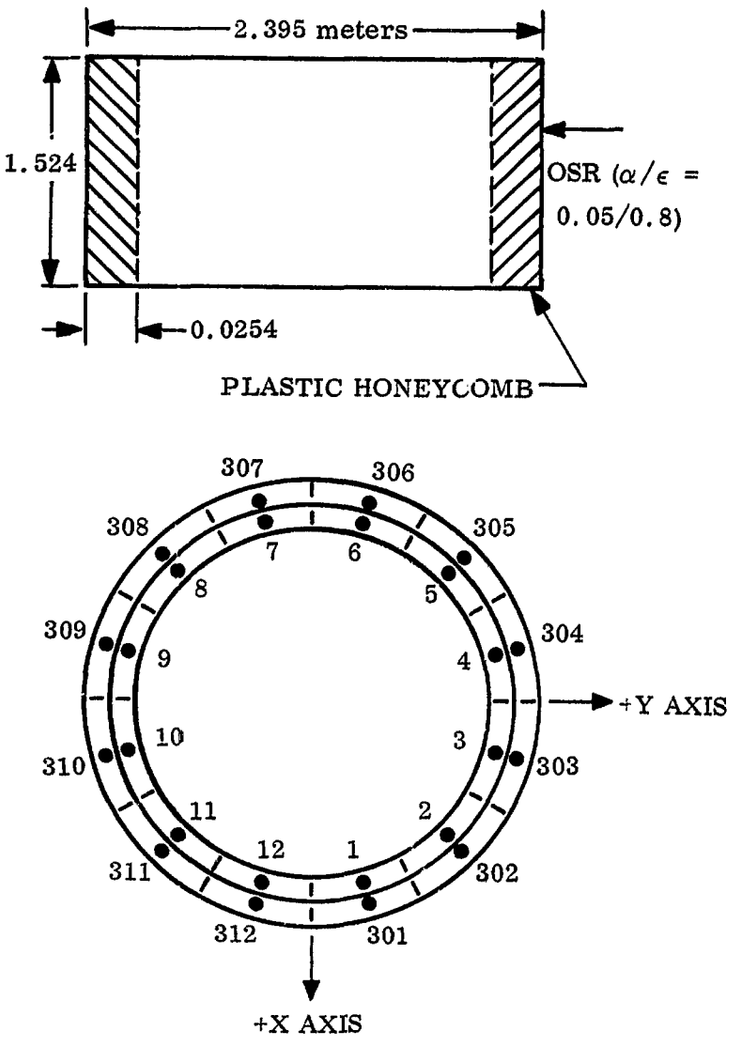


Fig. 5 Node Designation, Barrel Section A (+Z to Earth)

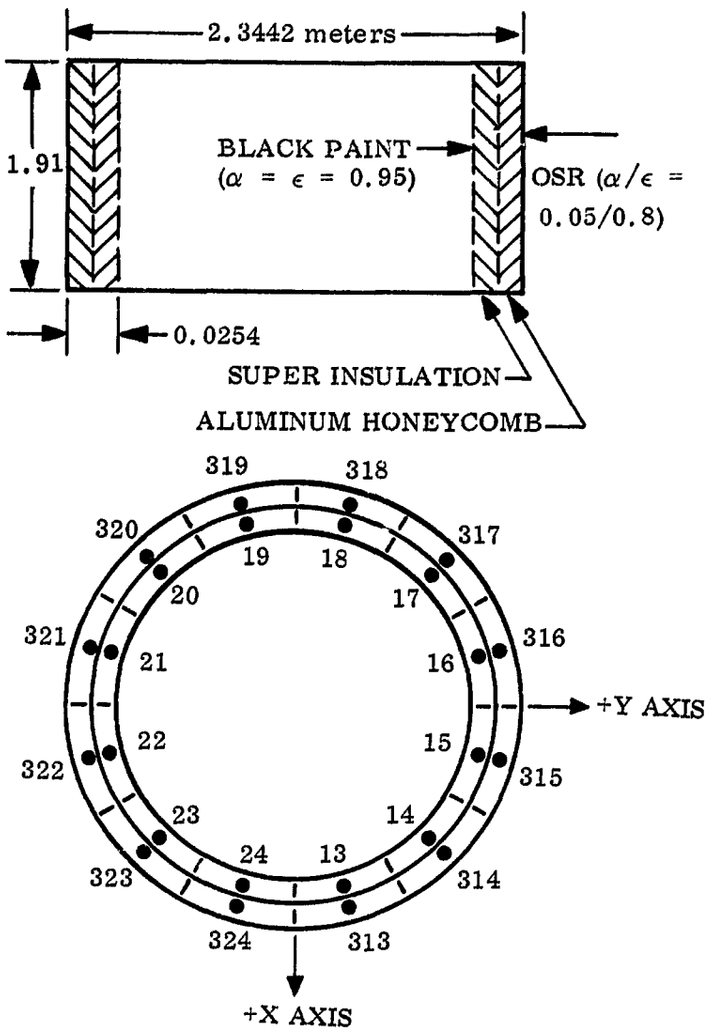


Fig. 6 Node Designation, Barrel Section B (+Z to Earth)

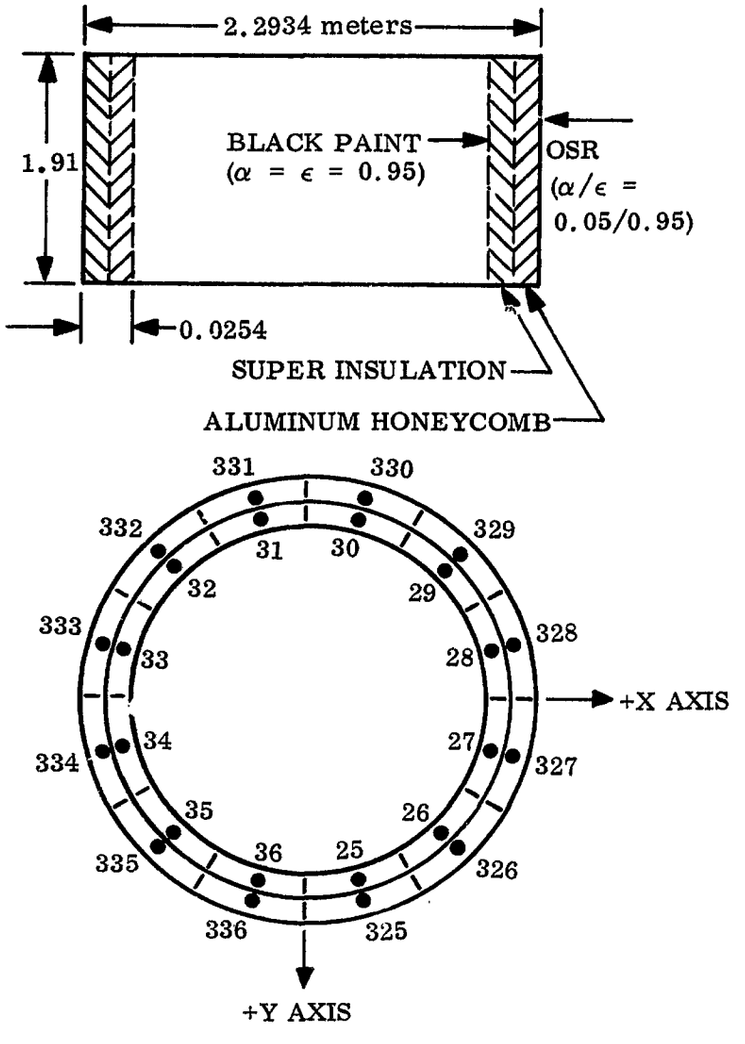


Fig. 7 Node Designation, Barrel Section C (+Z to Earth)

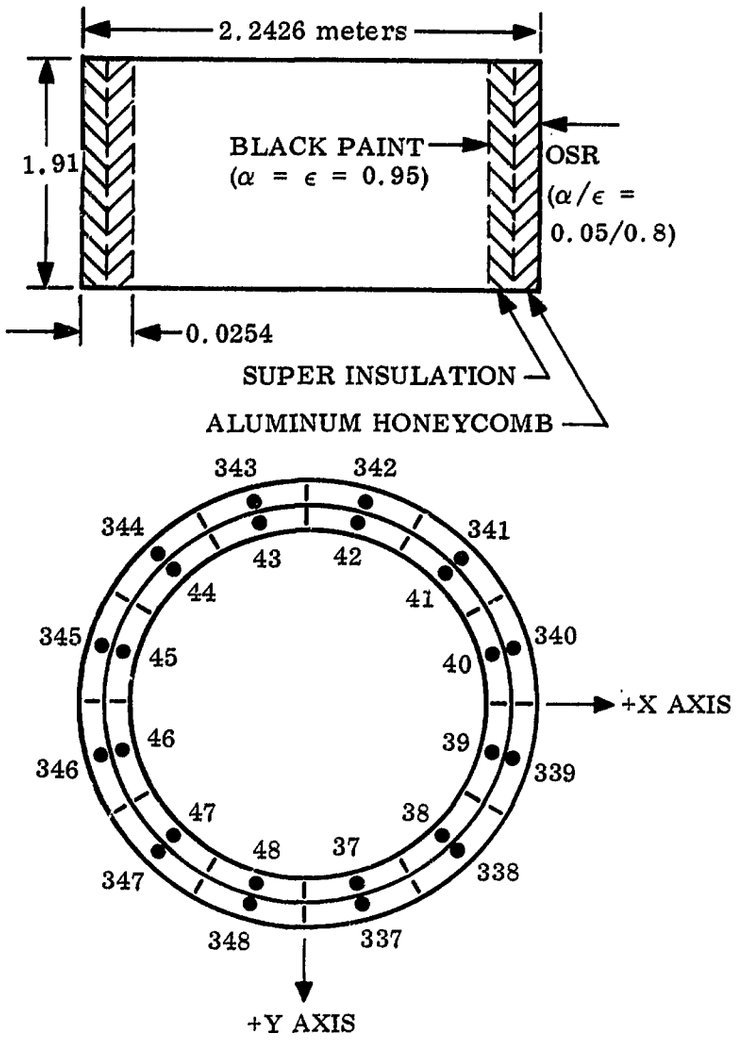


Fig. 8 Node Designation, Barrel Section D (+Z to Earth)

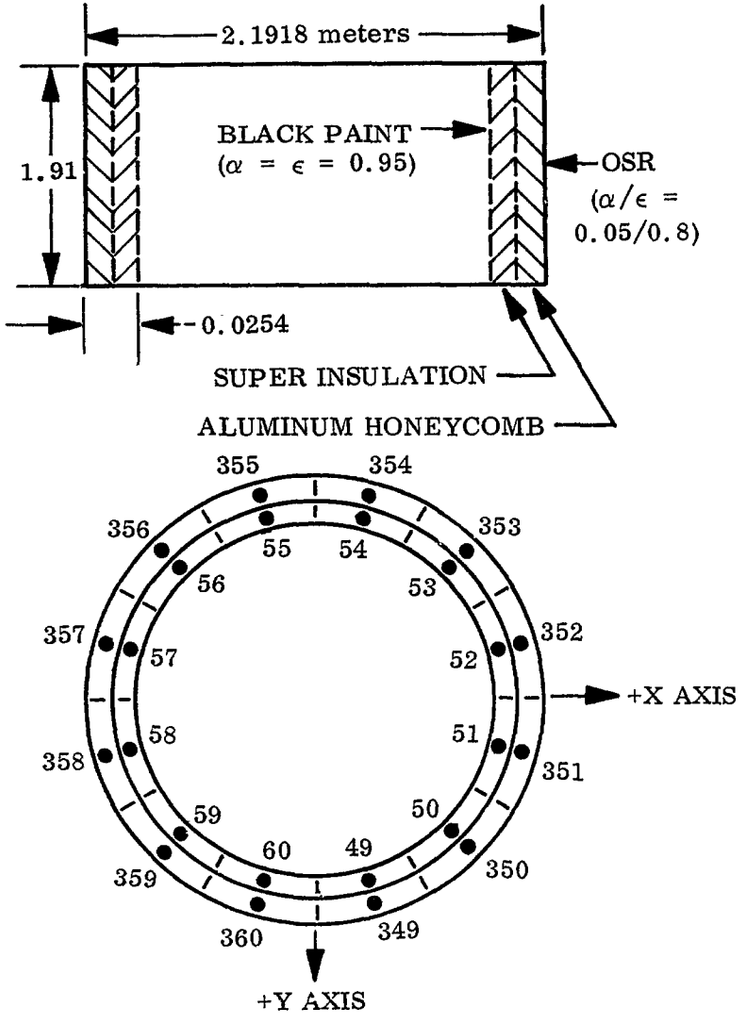


Fig. 9 Node Designation, Barrel Section E (+Z to Earth)

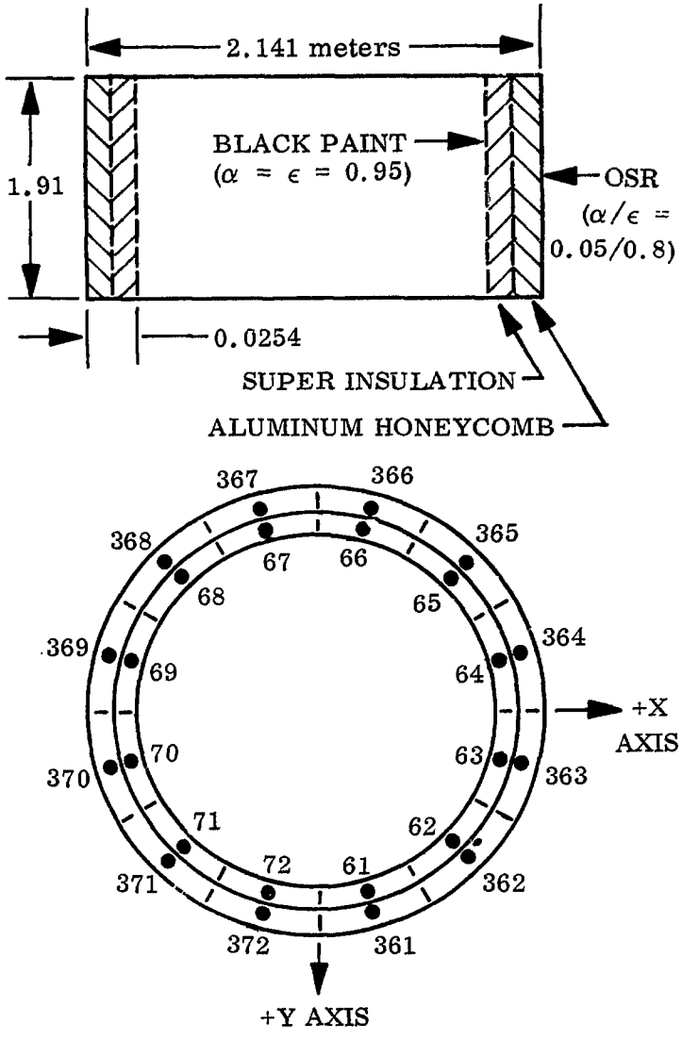


Fig. 10 Node Designation, Barrel Section F (+Z to Earth)

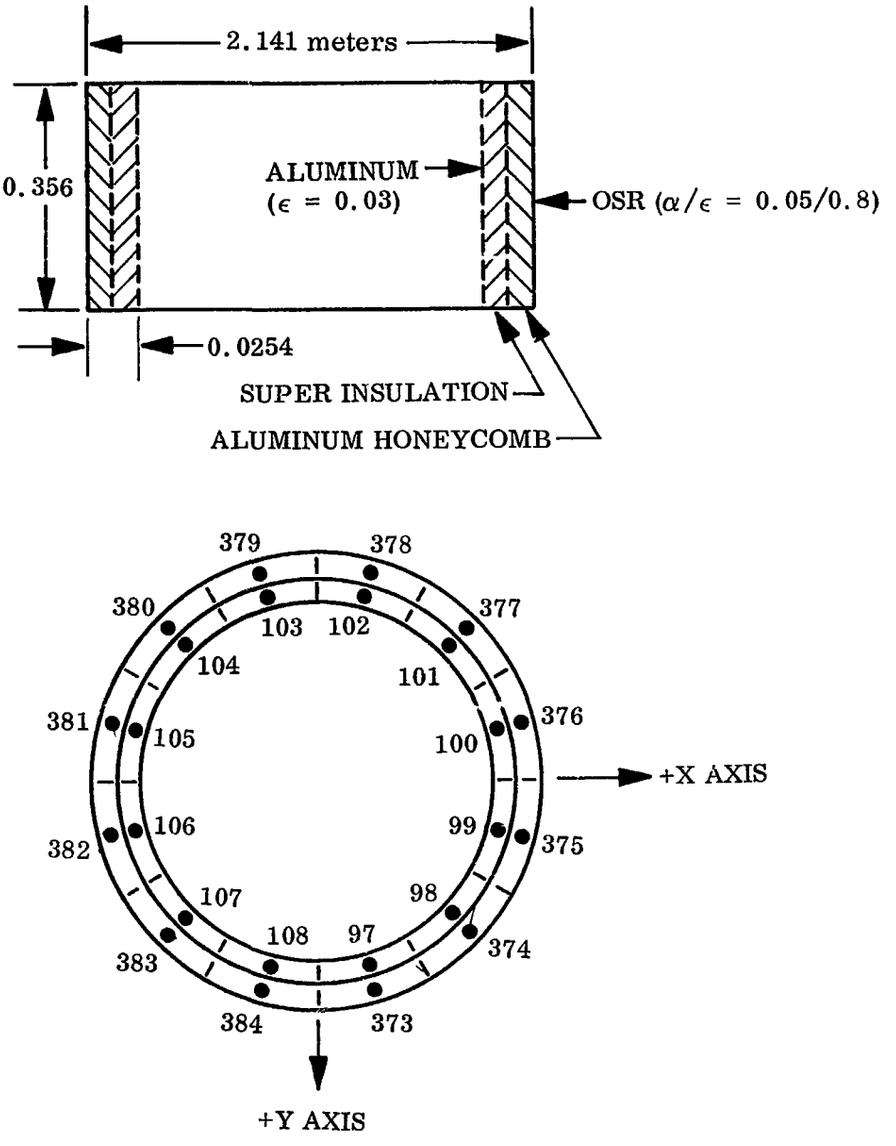


Fig. 11 Node Designation, Barrel Section H (+Z to Earth)

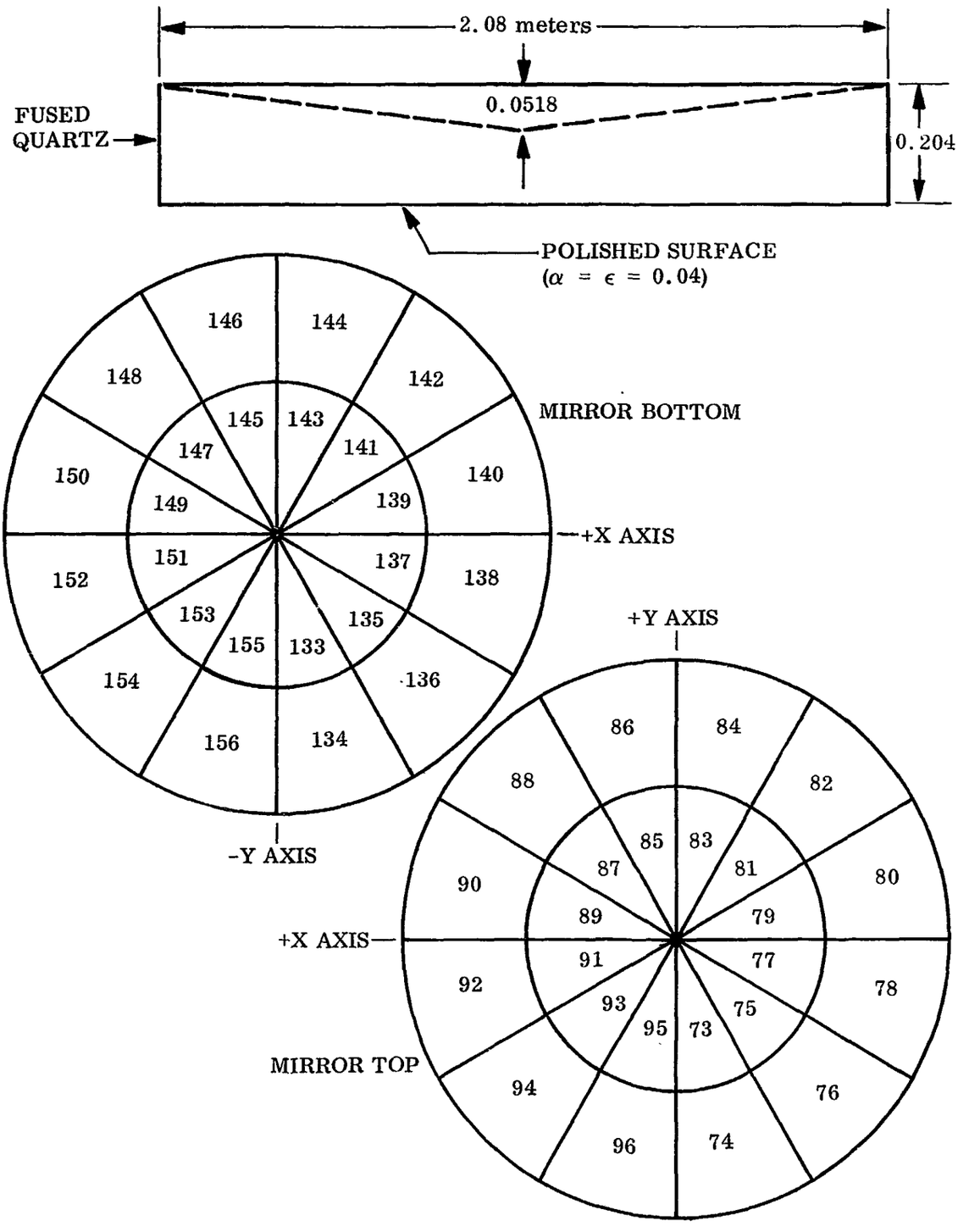


Fig. 12 Node Designation, Primary Mirror (+Z to Earth)

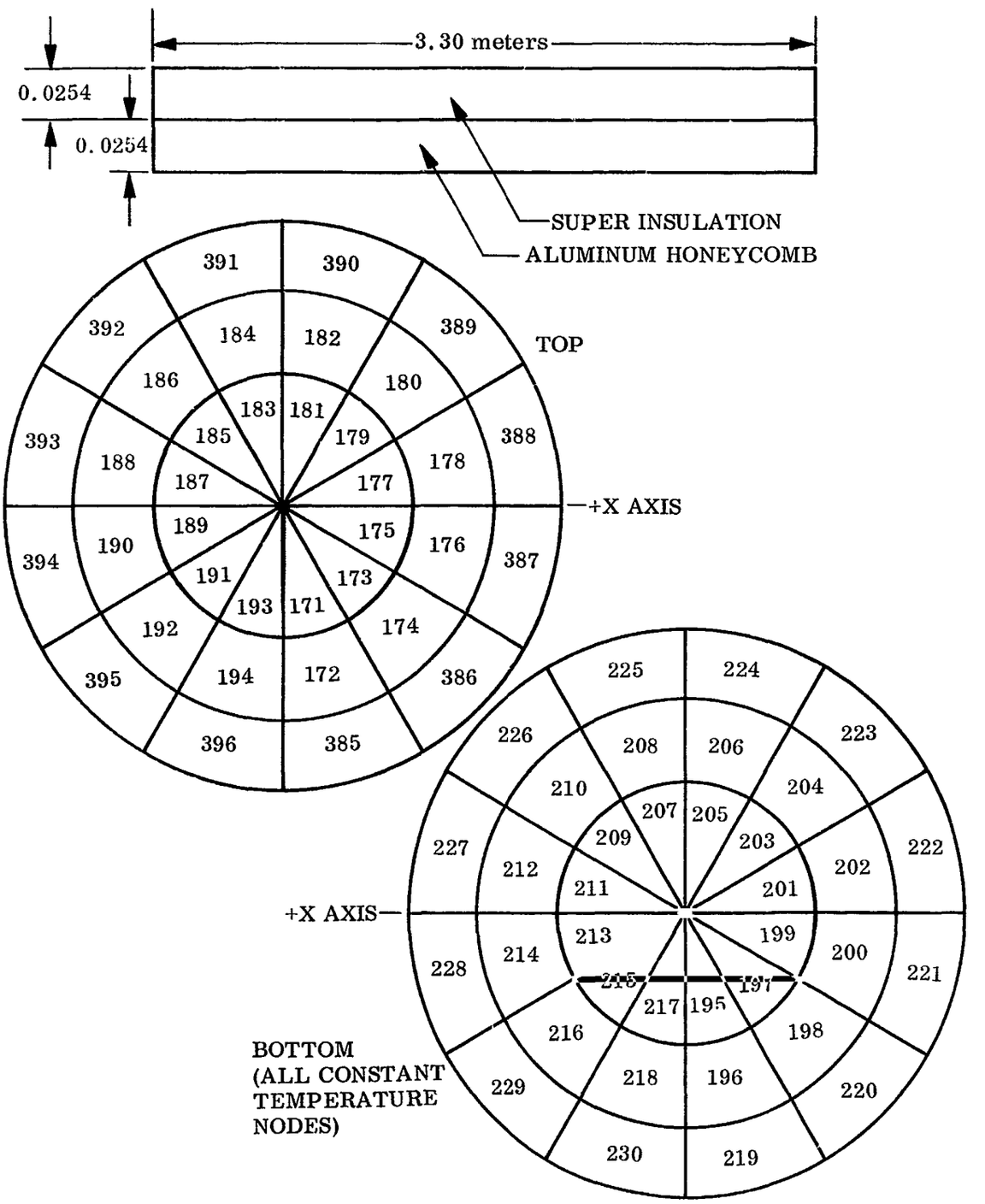


Fig. 13 Node Designation, Manned/Experiment Section

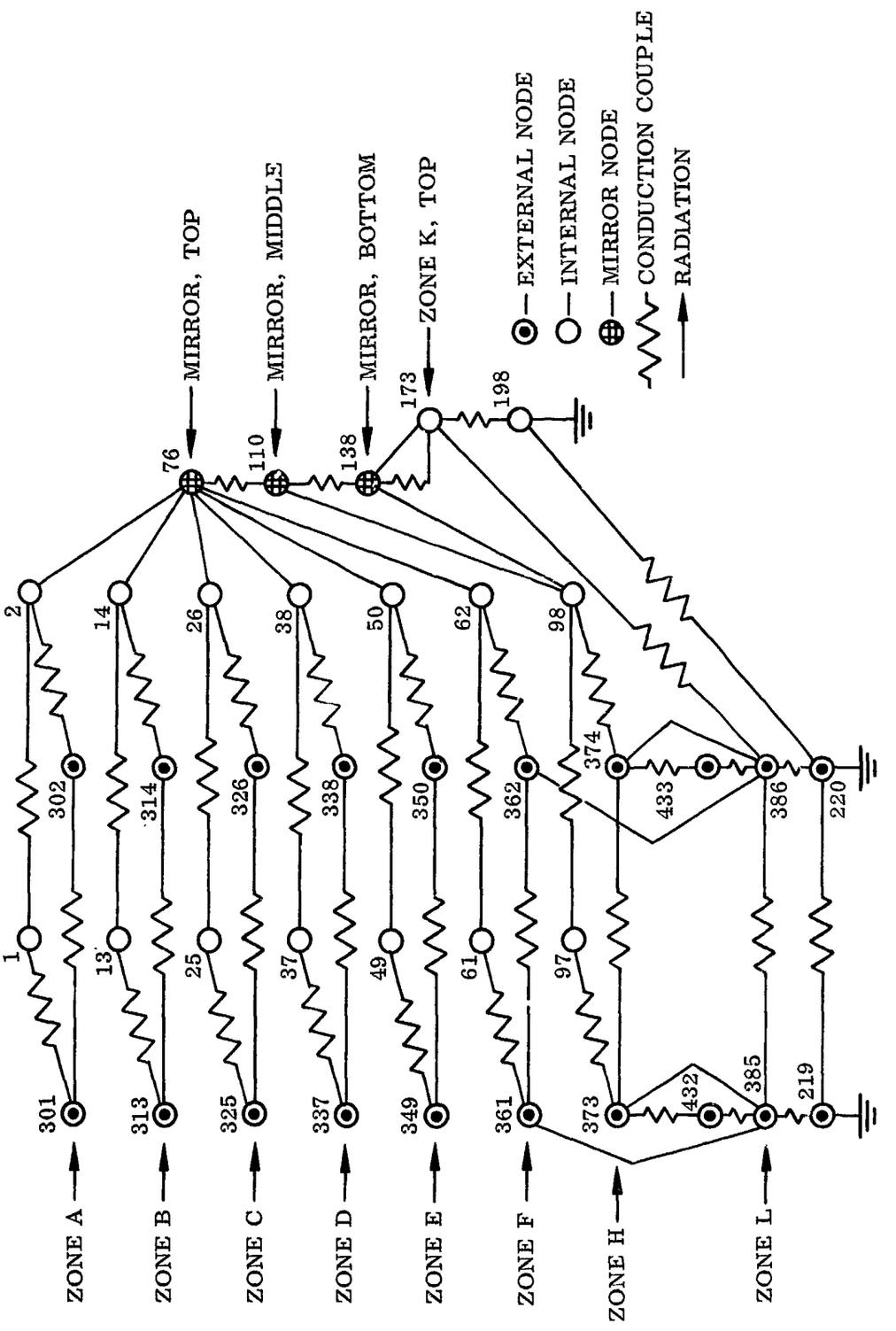


Fig. 14 Typical Conduction and Radiation Coupling, Zone A to Zone H

3.3 THERMAL PROPERTIES

The thermal properties used for purposes of the computation were obtained from available literature and are presented in Table 1. As previously indicated, the properties were assumed invariant with temperature and for this reason limit the accuracy of the predictions. The accuracy of the computations is also in question due to the wide variation in properties found in the literature. This is particularly true for the multilayer insulation and honeycomb materials whose thermal properties are strongly influenced by manufacturing techniques. It is quite clear that flight performance computations made in support of final hardware design will necessarily require laboratory evaluations of the actual materials to be used in hardware construction.

Table 1

THERMAL PROPERTIES

Material	Specific Heat Capacity (J/g°K)	Density (kg/m^3)	Thermal Conductivity (W/°K-m)
Plastic Honeycomb	0.464	144.5	2.88×10^{-2}
Aluminum Honeycomb	0.595	69.2	3.84×10^{-1}
Fused Quartz	0.431	2200.0	3.84
Multilayer Insulation	0.464	64.3	Parallel: 1.9×10^{-2} Perpendicular: 4.8×10^{-5}
Nylon	0.699	1140.0	1.34×10^{-1}
OSR	$\alpha_s = \epsilon = 0.05/0.80$		
Black Paint	$\alpha_s = \epsilon = 0.95$		

3.4 MATHEMATICAL ANALYSIS

The analysis of radiant interchange was accomplished by using an existing computer program that assumes diffuse interchange between reflecting surfaces. This program

utilizes a finite-difference approximation to find the view factor from node I to node J, i.e.,

$$A_I F_{I,J} = A_J F_{J,I} = \sum_I \sum_J \frac{(\Delta\bar{A}_I \cdot \bar{R}_{IJ})(\Delta\bar{A}_J \cdot \bar{R}_{IJ})}{(\bar{R}_{IJ} \cdot \bar{R}_{IJ})^2}$$

where $\overline{\Delta A}_I$ and $\overline{\Delta A}_J$ are the area vectors of nodes I and J, respectively, and $\bar{R}_{IJ}$ is the directed distance vector from node I to node J. The resulting view factors are combined with their respective emissivities, and a radiosity network formed to account for surface reflections. The final output of the program gives the radiation resistors which are the product of area and the complex view factor.

The radiant interchange between exterior surface nodes and the space environment at a synchronous altitude was computed using a method similar to that described above. Using this method, absorbed orbital energies (solar, albedo, and planet-shine) are calculated for each surface node, with surface reflections being taken into account. The computation assumed a solar constant of approximately 1400 W/m^2 incident upon a plane normal to the solar vector. Radiated earth-shine was assumed to be from a sphere of radius 6.41×10^3 km at a temperature of 248°K. The albedo energy was calculated by assuming a grey earth albedo of 0.38. The results of these computations show that earth albedo and emission contribute a very minor fraction to the total energy absorbed by the telescope exterior at the orbit altitude of 3.52×10^4 km. The fraction involved is illustrated by comparing absorbed energies for an external node at a point perpendicular to the solar vector. At such a point, an external node on the side facing the sun absorbed 80.70 W of solar energy, 0.011 W of albedo, and 0.130 W of earth emission. The fractions involved vary throughout the orbit; however, the total contribution of earth emission and albedo remains small.

Heat capacity was calculated for each node using the relationship

$$C = C_p \rho V$$

where

C_p = specific heat capacity, W-sec/°K
ρ = density, kg/m^3
V = volume, m^3

For nodes which had extremely small capacities the value was set to zero, thus making them "dummy" nodes and saving computation time. Compute intervals were determined from the minimum system time constant, which was directly proportional to capacity. A dummy node's transient temperature was determined by setting it equal to the average of the temperatures of all nodes connected to it by radiation and/or conduction.

For nodes of constant temperature, such as outer space (0°K) and the manned experiment section (298°K), the capacity was set equal to -1.0, thereby creating "sink" nodes which furnished constant temperature boundary conditions.

Conductive resistances between nodes were calculated using the equation

$$R_{I-J} = \frac{1}{K_{IJ}} \int dX/A$$

where

K_{IJ} = thermal conductivity, W/m °K
A = cross sectional area, m^2
X = distance between nodes I and J, meters

and where, in general, for uniform areas, it can be assumed that

$$R_{I-J} = X/K_{IJ}A$$

A complete listing of the resistances between nodes, computed for use in the analyses, has been furnished to the MSFC Space Sciences Laboratory under separate cover to this report due to the considerable volume required for inclusion herein.

Two orbital conditions were selected for study on the basis that they represented extreme conditions. Both cases assumed a zero β angle, where β is the angle between the orbit plane and the solar vector. Earth-oriented and space-oriented telescope optical axis directions were studied for this orbit inclination. Figure 15 further clarifies the conditions of interest.

Analyses to obtain temperature predictions were performed by using an existing thermal analyzer computer program. Initially, the steady-state temperature levels were found for each node using average orbital energy absorption. In this process the capacity of the nodes is neglected – except to discern between real, dummy, and sink nodes – and a net heat balance is performed for the nodal system. The results obtained for orbit average energy absorption for the space-oriented and earth-oriented conditions are presented in Table 2.

The transient analysis was then accomplished by inputting the orbit average steady-state temperatures as start temperatures and beginning the computation at an orbit point which best approximates the average orbital environment. For this case, the calculations were started past the subsolar point at intervals of 100 sec to obtain accurate representation of the changing environment.

The transient computation was performed only for the earth-oriented case in view of its considerably more interesting flight conditions. For this case, it is necessary to actuate the sun shutter prior to and after leaving the Earth's shadow which imposes highly variant heat inputs to the tube interior. For the space-oriented flight, these transients are absent. For purposes of this initial study, it was assumed that the sun shutter would close at a point where the gamma angle permitted direct solar energy to strike the interior surfaces of Section B. Likewise, it would open after this situation was passed after leaving the earth's shadow. Representative results of the transient computation are shown in Figs. 16 through 19. Since the transient behavior of all external sections was similar, only the results for Section B are presented. All nodes represented by Figs. 16 through 19 are located near to a plane passing through the X axis.

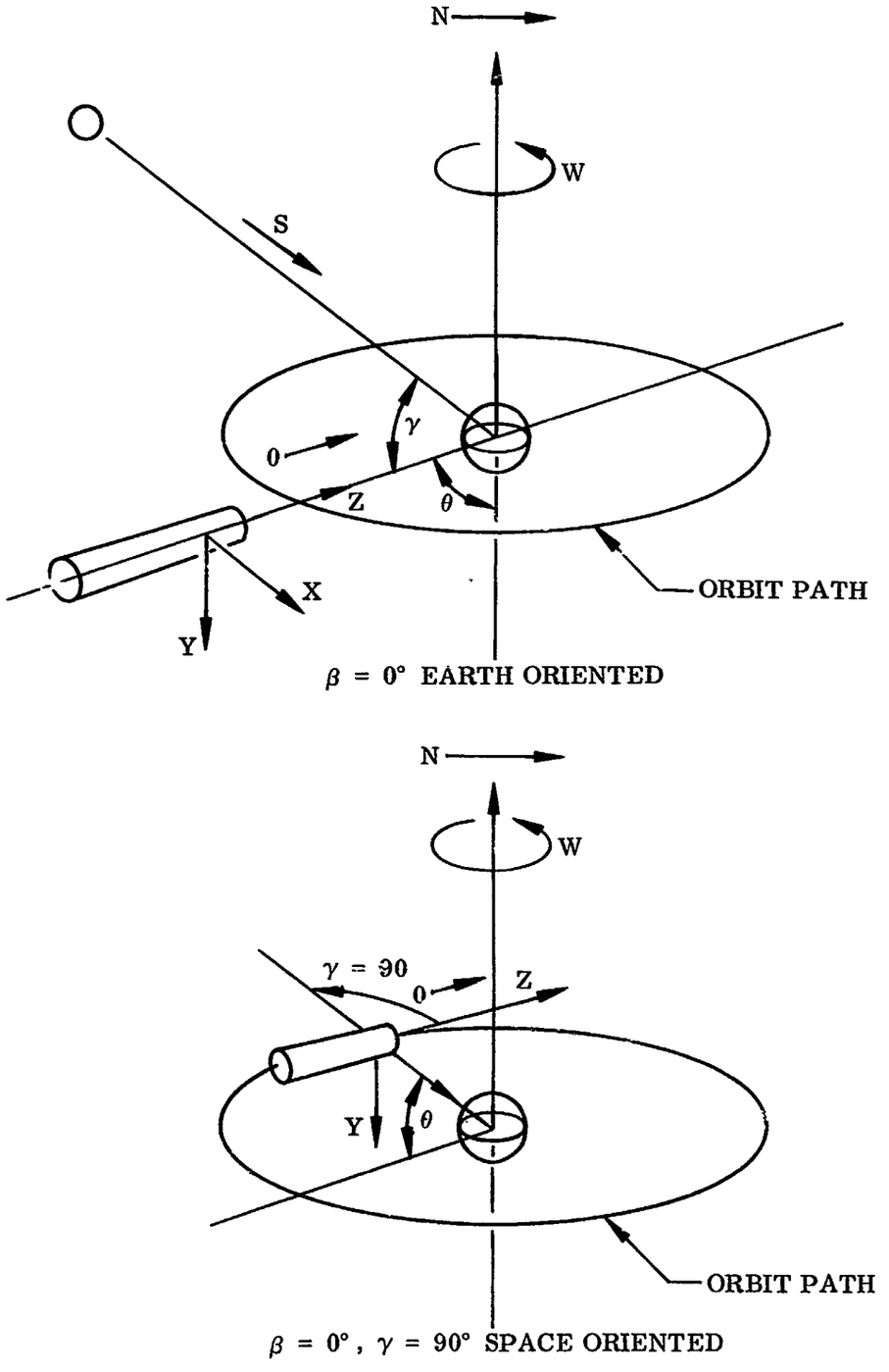


Fig. 15 Selected Orbital Configurations

Table 2

ORBIT AVERAGE TEMPERATURE PREDICTIONS TEMPERATURE, °K

Section	Node Number	Space Oriented	Earth Oriented
A Internal	1	87	137
A Internal	7	93	172
A External	301	76	133
A External	309	192	164
B Internal	13	99	153
B Internal	21	103	153
B External	313	74	109
B External	321	192	146
E Internal	49	116	165
E Internal	57	118	165
E External	349	75	110
E External	357	192	146
Mirror Top	73	138	176
Mirror Top	77	136	176
Mirror Bottom	133	138	176
Mirror Bottom	137	136	176
Manned Experiment External	385	104	158
Manned Experiment External	393	171	153
Barrel Support	442	99	150
Barrel Support	450	99	154
Manned Experiment Section	171	153	192

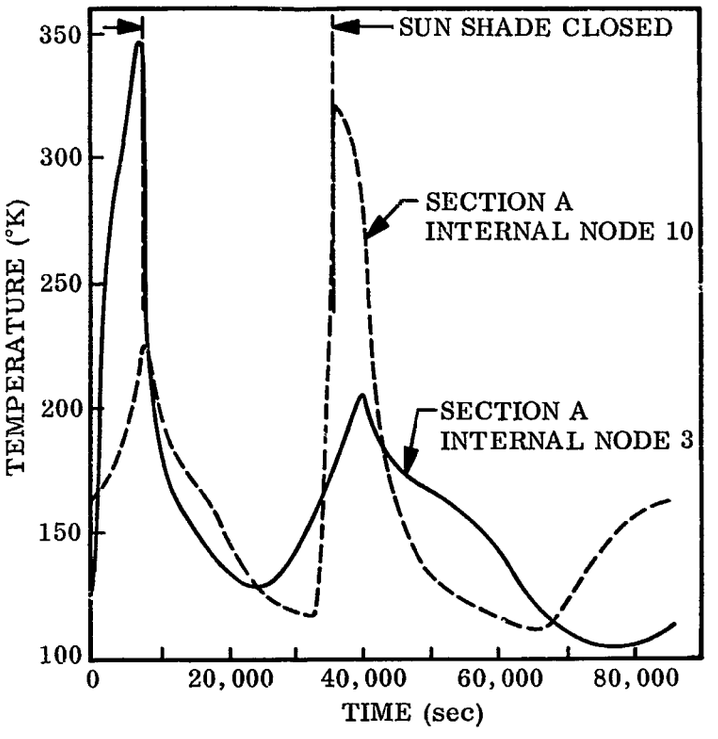


Fig. 16 Analytically Predicted Transient Thermal Behavior Section A

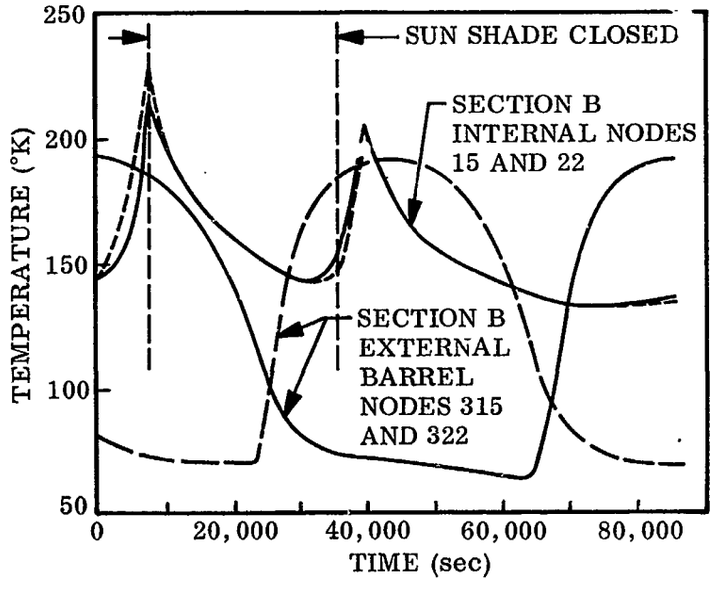


Fig. 17 Analytically Predicted Transient Thermal Behavior Section B

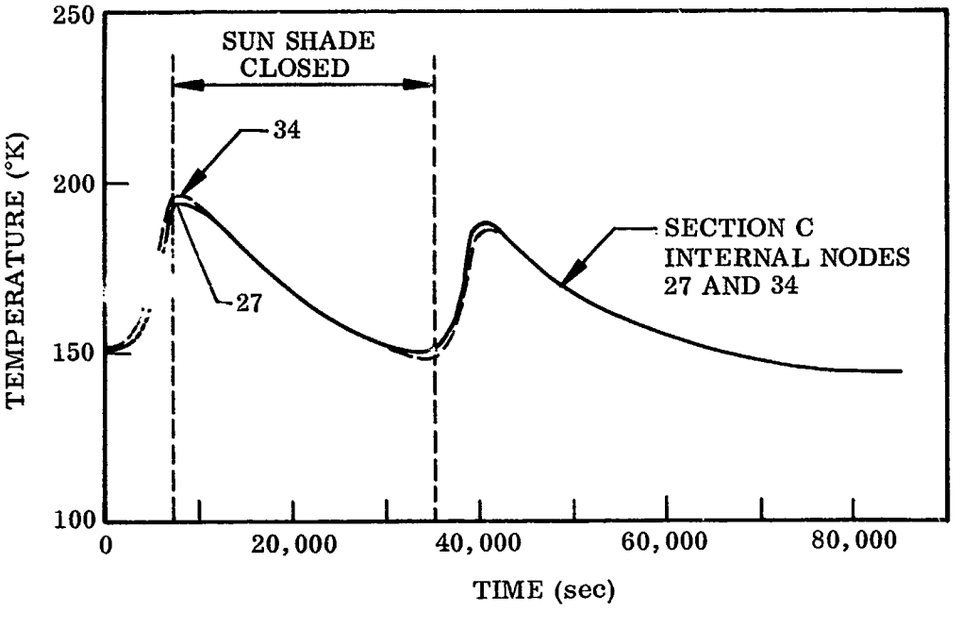


Fig. 18 Analytically Predicted Transient Thermal Behavior Section C

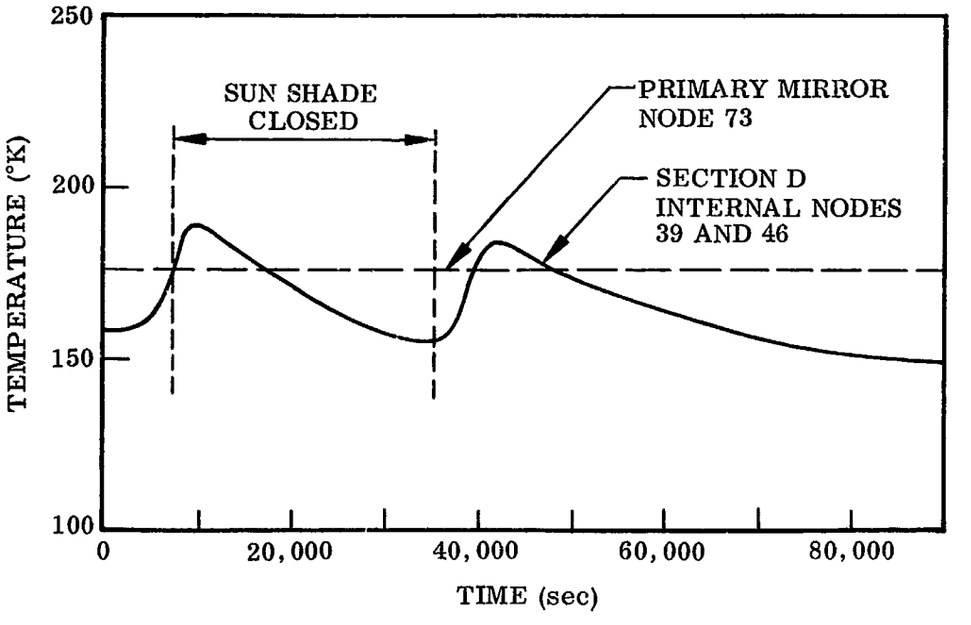


Fig. 19 Analytically Predicted Transient Thermal Behavior Section D and Primary Mirror

The orbit average predictions were useful primarily for purposes of starting the transient computation at some logical point. For this reason, their utility for comparisons to model results is limited. However, because of the long time constant of the primary mirror and the considerable damping of transients down the telescope tube, it is apparent that orbit average results are a reasonable indicator of primary mirror equilibrium temperatures.

The transient computation very clearly shows that solar energy entering the telescope front section is the primary contributor to temperature variations in the tube and also has a strong influence on the mean temperature assumed by the primary mirror. This is made clear by comparison of the temperatures presented in Table 2 for the space- and earth-oriented cases. The primary mirror orbit average temperature for earth orientation, where considerable solar energy enters the interior of Section A, is 40°K higher than for space orientation where only a very small amount of solar energy enters Section A directly. Therefore, it is obvious that selecting a different time for opening and closing of the sun shutter will result in a lower or higher primary mirror equilibrium temperature. Since the sun shutter has the dual role of keeping direct solar energy out of the optical path and of providing active thermal control, it is obvious that a more comprehensive study should be performed to establish optimal times for shutter activation under a variety of orbital conditions. The opening and closing times selected for this preliminary study were in a sense arbitrary and are not suggested as being the most appropriate. The purpose here was to establish temperature histories, based on prescribed operating conditions, that could be used to set the boundary conditions needed for completion of the model studies.

The maximum front-to-back and edge-to-edge temperature differences predicted for the primary mirror were on the order of 1°K. This prediction is basically due to the assumption that the three mirror segments were isolated from each other and had weak conductive coupling to the manned section interface. The validity of these assumptions will depend upon the final flight hardware mirror mount design. It is reasonable to assume that conduction isolation between mirror segments will be possible; however, zero conductance to the manned section is unlikely. Further analytical

work will be necessary, following final hardware design, to clarify the primary mirror thermal behavior.

The transient results presented in Fig. 17 show the effectiveness of the multilayer insulation in damping out the influence of external transients. The internal nodes, 15 and 22, closely follow the thermal input from Section A and show no response to the transients of nodes 303 and 310. This result was most important in setting the criteria for design of the thermal model since it permitted the use of steady state properties in selection of the model's multilayer insulation. A limited study was also made to determine the influence of the multilayer insulation thermal conductivity on overall thermal performance. Orbit average computations were completed using perpendicular conductivity values of 1×10^{-3}, 1×10^{-4}, 1×10^{-5}, and 1×10^{-6} W/°K-m with findings that no significant change in internal temperatures occurred except for the lowest value. This result verified that the telescope wall was essentially adiabatic and that transient energy transfer through the wall was of less importance than energy transferred from the aperture or manned support section. The subject of modeling the insulation is treated in considerably more detail in Section 4.

The analytical studies of the 2-meter telescope carried out in support of this program did not encompass all of the details that would necessarily be considered for hardware design. However, sufficient detail was included to permit meaningful comparisons between the analyses and model test results. In the event of better definition of the telescope hardware, it would be possible to extend the analytical work to include areas of particular interest such as the servo-drive mechanism for the primary mirror, the manned experiment section and its influence on the optical system, other beta and gamma attitudes, optimum shutter operating cycles, and the influence of the temperature dependence of thermal and optical properties. A study of these details was not necessary for the completion of this program.

Section 4

THERMAL MODELING OF THE OTES MULTILAYER INSULATION SYSTEM

4.1 INTRODUCTION

An experimental program was undertaken to develop criteria for thermal modeling of the multilayer insulation system for the 2-meter OTES telescope. This activity was required in order to design and construct a properly scaled insulation wrap for use on the 1/6.43 scale model described in Section 5. Prior to this effort, very little work had been done in the area of thermal modeling to establish techniques required for thermal scaling of multilayer insulation, and consequently, modeling criteria for such systems were virtually nonexistent. A great deal of work had been accomplished to define thermal characteristics of multilayer insulation systems for both high and low temperature applications; however, this work did not consider thermal modeling aspects of such systems.

Since the primary objective of the overall program, reported herein, was to design, fabricate, and test a small-scale thermal model of the 2-meter OTES space telescope, the insulation experiments were designed to coincide with performance characteristics of the prototype system. For the telescope thermal model, a thermophysical properties preservation approach to modeling was selected. With this technique, either identical materials or substitute materials, which have thermal properties similar to those of the prototype's for scaled temperature conditions, are used in designing the model. For most solid materials, thermal conductivity does not vary with changes in the length of the heat flow path. This is not the case for multilayer insulation where, in addition to being temperature dependent, thermal conductivity is also dependent upon the number of layers in the wrap and upon the wrap density. Consequently, reducing insulation thickness according to the specified length scale-ratio can cause sizable changes in thermal conductivity.

Previous work (Ref. 13) has shown the variations in thermal conductivity which occur as a result of changes in boundary temperatures, layer density, and the number of insulation layers. However, the data reported were not sufficient to meet the requirements for modeling the OTES insulation system. This ruled out the possibility of a purely analytical study and established the need for a combined experimental and analytical program to determine the modeling criteria. This approach was successful, with the results demonstrating that steady state thermal conductivity perpendicular to the insulation layers can be modeled effectively at elevated temperatures utilizing identical materials.

The multilayer insulation experiments were designed to meet objectives of modeling the OTES system and were not intended to be a general study of modeling multilayer insulation systems. However, the experimental and analytical techniques developed here should provide a useful basis for further study in this area.

4.2 APPROACH

The multilayer insulation thermal modeling studies involved the design, construction, and testing of two models having similar thermal behavior. The larger of the two models, referred to in these studies as the full-scale insulation model, consisted of four open-end cylindrical sections scaled in overall size to be one-third that of four similar sections on the 2-meter OTES telescope. The smaller model was geometrically identical to the larger and was designed to be a half-scale thermal model of the larger system. Its diameter was similar in size to that planned for the complete OTES thermal model described in Section 5. The size and configuration of the insulation models were chosen on the basis of test chamber size and a desire to duplicate the difficulties associated with fabrication of the insulation required for the prototype telescope and the telescope thermal model. Temperature conditions for the insulation models were also scaled relative to the prototype, with the temperature ratios (T*) for the full- and half-scale models being 1.44 and 1.82, respectively.

Although sizes and operating temperature levels were scaled relative to the prototype telescope, neither of the insulation test objects was designed to be a thermal model

of the OTES system. Such a condition was not required to meet the objectives of the study. Thus, for purposes of the insulation experiment, the full-scale insulation model was, in effect, a prototype with the half-scale system being the scaled thermal model.

Characteristics of the multilayer insulation for the full-scale insulation model were identical to those planned for the prototype telescope. The insulation consisted of a 1.27-cm thick wrap of alternate layers of double aluminized mylar and glass-fiber paper with a layer density of 28.3 layers/cm. An insulation wrap identical to that planned for the prototype telescope was used on the full-scale insulation model in order to obtain initial experimental data that could be used as a basis for modeling the insulation on smaller systems. Having defined the thermal properties of the full-scale wrap, modeling to a half-scale system was done analytically followed by tests on the model to verify the analytical predictions. The results were then extrapolated for application to smaller models, and a suitable insulation wrap for the complete telescope model, with a scale ratio of 1/6.43, was designed.

In addition to its function as the insulation prototype as described, the full-scale insulation model was used as the primary indicator of changes in thermal performance caused by varying the insulation wrap configuration. This study was included to determine the effects of an exterior versus an interior insulation wrap and to investigate the possibilities of using a wrap which extended continuously the entire length of the thermal model. During the early stages of the program, a continuous wrap was thought to be desirable from the standpoint of facilitating assembly of the complete OTES thermal model. The configurations studied were as follows:

(1) A continuous exterior wrap with no separation of the insulation at the edges of each cylindrical section
(2) An exterior wrap with separation of the insulation at each edge of the separate cylindrical sections
(3) An interior wrap with separation of the insulation at each edge of the separate cylindrical sections

These configurations are referred to as test configurations 1, 2, and 3 throughout those portions of the report dealing with the multilayer insulation studies. Details of each are described in subsection 4.3.

To determine the thermal insulating characteristics of the wrap and to establish a basis for comparison between internal and external systems, the one-dimensional thermal conductivity (K) was determined for test configurations 1 and 3. This was done for various temperature levels in order to establish the temperature dependence of K over the operating temperature range of the full- and half-scale insulation models. Such a determination of K as a function of temperature was required in order to judge whether or not the insulation blanket for the half-scale model had been scaled properly. The tests to determine K were accomplished using only three sections of the four-section model. Both ends of the system were closed with insulated flat disks, heat sources were installed within the model's interior, and both internal and external surface temperatures were monitored using appropriate thermometry. From thermal conductivity measurements on the larger model and the analysis which followed, the layer density and insulation blanket thickness were selected for the half-scale model.

To evaluate the performance of the multilayer insulation in terms of OTES system performance, a series of tests involving transient heating and cooling was run on each test configuration. For these tests, an insulated disk was removed from one end of the three-section unit and the fourth cylindrical section, designed to represent the front section (Section A) of the prototype telescope, was attached. Heaters in the form of high intensity tungsten-filament lamps were installed circumferentially around the exterior of Section A. In addition, a line of lamps was installed longitudinally along the top exterior surface of the three-section insulated tube. Two distinctly different external energy rates were used in the system performance tests. Both relied upon the analytical study of the prototype as a means of establishing the desired skin temperatures. In the first case, Section A was thermally cycled from maximum to minimum temperature while the top exterior of the model was subjected to a constant radiant flux.

For the second case, the top exterior of the model was cycled between maximum and minimum temperatures while Section A was held at an average temperature. The heating and cooling cycles were accomplished by a programmed square-wave heat pulse from the two separate lamp bank systems. For the full-scale model, the period of each cycle was based on an orbital period of 24 hr. The period for the half-scale model during a similar series of tests was scaled to be 1/4 that of the larger system.

The results obtained from the full-scale model tests were used to establish design criteria for modeling the insulation for the half-scale model. For the latter system, an internal wrap with separation of the insulation at the edges of each section was selected. While an internal wrap was required as indicated by the full-scale tests, separation at the edges was not found to be a requirement. Separation of the insulation between sections was chosen for the half-scale model primarily for convenience of assembly. The test configuration selected for the half-scale model will be referred to as test configuration 4.

In designing the half-scale system, the thermal modeling approach of materials preservation was employed. This method was used for the insulation studies since a similar approach was required for modeling the prototype OTES telescope. As discussed in subsection 4.3.4, the modeling criteria for materials preservation are that ρ^*, C_p^*, and K^* be equal to unity which gives $T^* = (1/t^*)^{1/3}$, where t^* is the insulation thickness ratio. However, when multilayer insulation is involved, it is almost certain that some distortion of one or more of the material property ratios as well as the insulation's thickness ratio (t^*) will be required to model important temperatures and heat fluxes. The principal reason for this is that thermal conductivity changes with temperature and with variations in blanket thickness and insulation layers. For this program, both K^* and t^* for the multilayer insulation were distorted. Since the smaller insulation model was designed to be a half-scale thermal model of the larger, the criteria employed in design of its insulation were to maintain $K^*/t^* = 2$, thereby preserving a temperature ratio (T^*) between model and full-scale system equal to 1.25.

To determine the degree of success achieved in modeling the half-scale system, tests were run to establish the one-dimensional K (perpendicular to the insulation layers) for various temperature levels. While the thermal conductivity of the wrap was of importance to this investigation, and for this reason received considerable attention, it was also desired that a comparison of the transient perfor ance characteristics of the full- and half-scale models be obtained. Both transient performance testing and determination of one-dimensional conductivity were accomplished for the half-scale model following the same procedures as used for the full-scale insulation test object.

4.3 DESCRIPTION OF INSULATION TEST MODELS

The model geometries discussed in this section and the test procedures presented in subsection 4.4.4 were used to accomplish two separate goals. The first was to obtain tests results on the success achieved in modeling the one-dimensional thermal conductivity of the multilayer insulation. Totally enclosed test objects were used for this purpose. The second was to observe the effects of different insulation wrap configurations and the influence of gaps and exposed edges in the insulation on the overall system performance under transient conditions similar to those predicted for the OTES telescope system. An open-ended test configuration and external lamp bank system were used for this purpose.

The two models constructed for experimental evaluation during the multilayer insulation investigation were geometrically identical, with one system representing a half-scale thermal model of the other. The full-scale insulation model was approximately 76.2 cm in diameter and had a maximum length of 236.2 cm. It consisted of four cylindrical sections, three of which were insulated similar to the prototype OTES telescope and one which was not insulated. The geometry and size of this model was scaled to be approximately one-third that of a similar four sections on the prototype (i.e., Sections A, B, C, and D). The model was limited to four sections because of test chamber size; however, the use of only four sections was adequate for achieving the objectives of this investigation. Three different insulation wrap configurations were evaluated and compared during testing of the full-scale mode. From these evaluations of the full-scale model, the type of wrap to be used on the half-scale test object was selected

and modeled accordingly to provide the required heat flow perpendicular to the insulation layers. The various insulation wrap configurations will be referred to as configurations 1, 2, and 3 for the full-scale system, and configuration 4 for the half-scale model.

In addition to the three insulation wrap configurations, two different test arrangements were required for each model. They consisted of a three-section cylindrical tube for one-dimensional thermal conductivity determinations and a four-section cylindrical tube for transient performance evaluations. Details of the various insulation configurations and the different test arrangements employed to study and model the thermal characteristics of the multilayer insulation system are described in this section of the report.

4.3.1 Test Configuration 1

The one-dimensional and transient test arrangements for this configuration are illustrated in Figs. 20 and 21. The individual cylindrical sections are identified A, B, C, and D corresponding to the nomenclature used in describing the prototype telescope in Section 2. Basically, this configuration consisted of an exterior multilayer insulation wrap with no separation of the insulation between Sections B, C, and D.

For determination of thermal conductivity perpendicular to the insulation layers, the one-dimensional test arrangement was employed. This unit consisted of three stainless steel cylinders connected together and insulated on the exterior with a continuous insulation wrap extending the full length of the model. Both ends were closed off with multilayer insulated flat disks, thus providing an enclosure completely surrounded by the insulation system being evaluated.

The internal cylindrical skin was constructed from 0.064-cm thick, Type 301 stainless steel sheet, tempered to 1/2-hard. The cylindrical sections were spaced 0.64 cm apart by means of three 0.95-cm-wide and 0.031-cm-thick stainless steel tabs at each joint. These connectors provided the required structural rigidity while also effectively

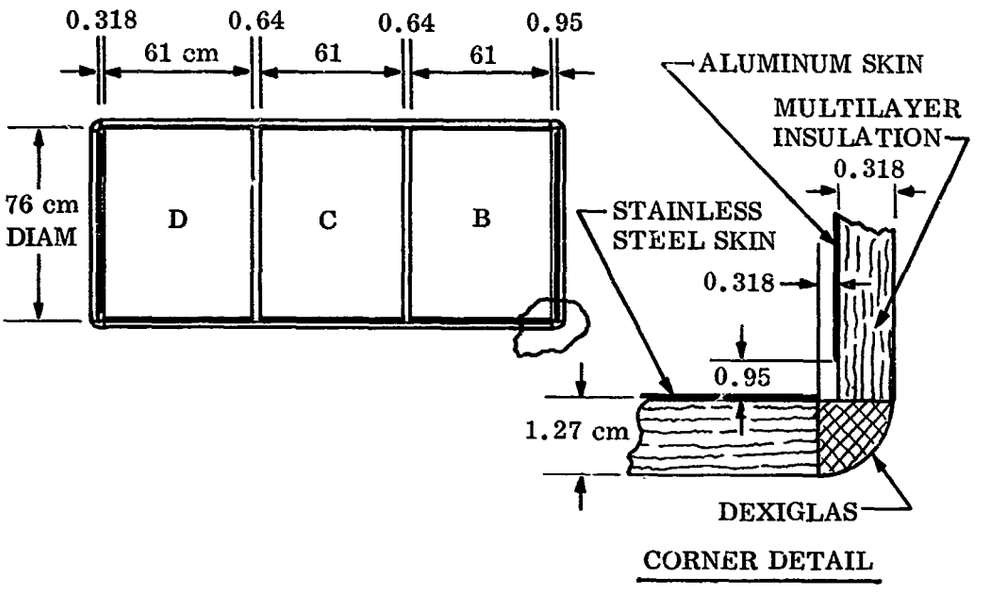


Fig. 20 Configuration 1: One-Dimensional Test Arrangement

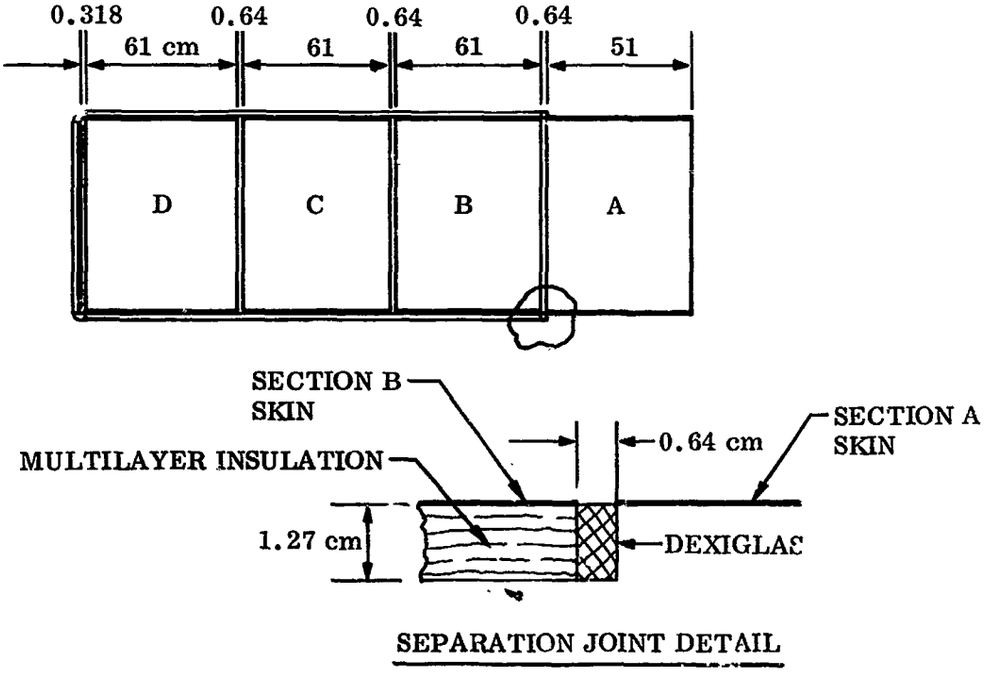


Fig. 21 Configuration 1: Transient Test Arrangement

disconnecting the cylinders from axial solid conduction. During initial design of this model, consideration was given to modeling the honeycomb skin of the prototype telescope using the materials preservation approach being employed for modeling the insulation system. However, to properly model the low thermal conductivity of the 1.27-cm-thick honeycomb skin using readily available materials (e.g., stainless steel sheet) would have required thicknesses on the order of 0.0089 cm for the full-scale system and 0.0043 cm for the half-scale model. The required structural rigidity of the models ruled out the use of such thin materials. The sizes finally selected, of course, did not provide the circumferential temperature gradient predicted for the prototype. However, preservation of this gradient was not necessary for the intended purpose of the experiment.

The insulated end disks were 74.5 cm in diameter and were constructed from 0.081-cm-thick 6061-T6 aluminum sheet. They were attached to the cylinders by four small teflon angle brackets which also provided a low thermal conduction link between the ends and cylindrical sections. The multilayer insulation used for the end disks was an exterior wrap and was similar in structure to that used on the cylinders except for a slight difference in layer density. Although the same number of layers was used, the insulation on the ends tended to compress more than on the cylindrical sections causing the wrap to be approximately 0.95-cm thick rather than the 1.27-cm thickness obtained on the cylinders. The diameter of the insulation blanket was made larger than the aluminum disk by 1.9 cm, as shown in Fig. 20, in order to fill the space around the edges not covered by the aluminum plate.

Modification of the one-dimensional steady state configuration for the transient system performance tests consisted of removing the insulated end plate adjacent to Section B and installing the noninsulated Section A as illustrated in Fig. 21. Section A was designed to simulate the sun-shade section of the prototype telescope, although, as was the case with the other sections, exact scaling of the honeycomb skin was not done. This section was constructed of 0.127-cm-thick 6061-T6 aluminum and had the same internal diameter as the insulated sections. Aluminum was used for this section to facilitate its fabrication and assembly and to provide better control of the circumferential temperature profile required during its operation as a simulated sun-shade

section. It should be noted here that the objective of the insulation experiment did not require that the diameters of the cylindrical sections be different as is required for the telescope tube of the prototype. In fact, the use of variable diameters for these models would have unnecessarily complicated the experiments and caused correlation of results between configurations to be more difficult. To provide a low thermal conduction link between Section A and the other sections, the cylinder was attached using four small Teflon connectors which also served to maintain the desired spacing between Section A and Section B.

Figure 22 shows the assembled test object installed on the movable test chamber door just prior to a transient performance test run. The photograph is actually of test configuration 2, but is also representative of the other configurations tested. To minimize the conduction heat exchange between the test object and the surrounding environment, the object was suspended from an overhead beam by six 0.051-cm-diameter stainless steel wires. For Section A, the wires were attached at the top directly to the aluminum skin. In the three insulated sections, the wires penetrated through the insulation blanket between sections and at the ends and were attached to a center shaft extending longitudinally along the axis of the three sections.

The center shaft with a wire spoke arrangement supported the three insulated sections and maintained their cylindrical shapes. The spokes, consisting of 0.051-cm-diameter stainless steel wire, extended between the center shaft hub assembly and the stainless steel skin. The center shaft consisted of a 1.27-cm-diameter stainless steel tube with a wall thickness of 0.071 cm. Figure 23 is a photograph of the interior of the test object showing the center shaft and spoke arrangement. For each section, two brass hubs with seven spokes in each hub were used. Conduction heat flow from one side of the model to the other through the wire spokes was calculated and found to be negligible in comparison to the energy transferred by radiation.

The center shaft and spoke arrangement also facilitated handling of the assembly both during and after installation of the insulation blankets. Care during application of the multilayer insulation and careful handling of the assembled test object was an important

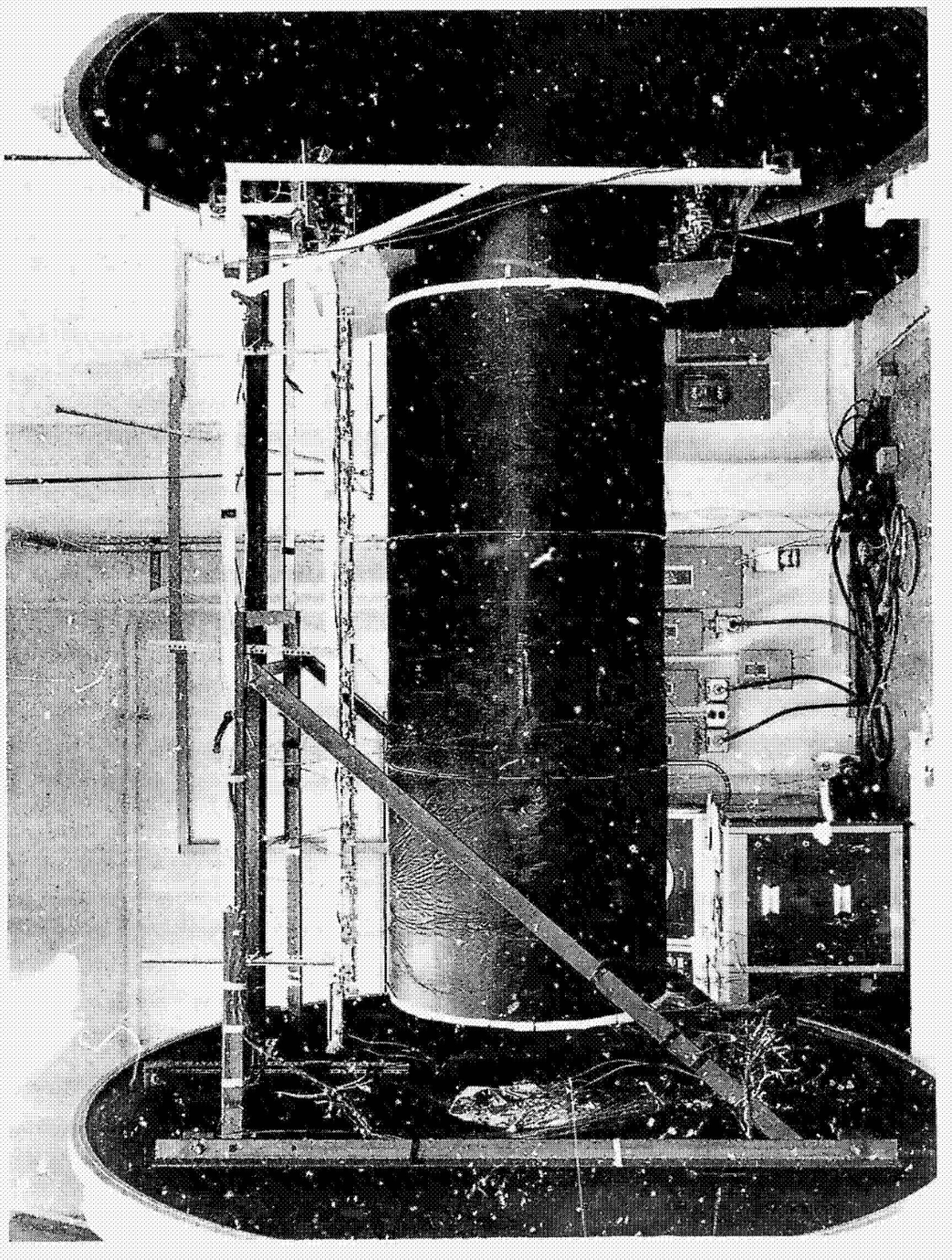
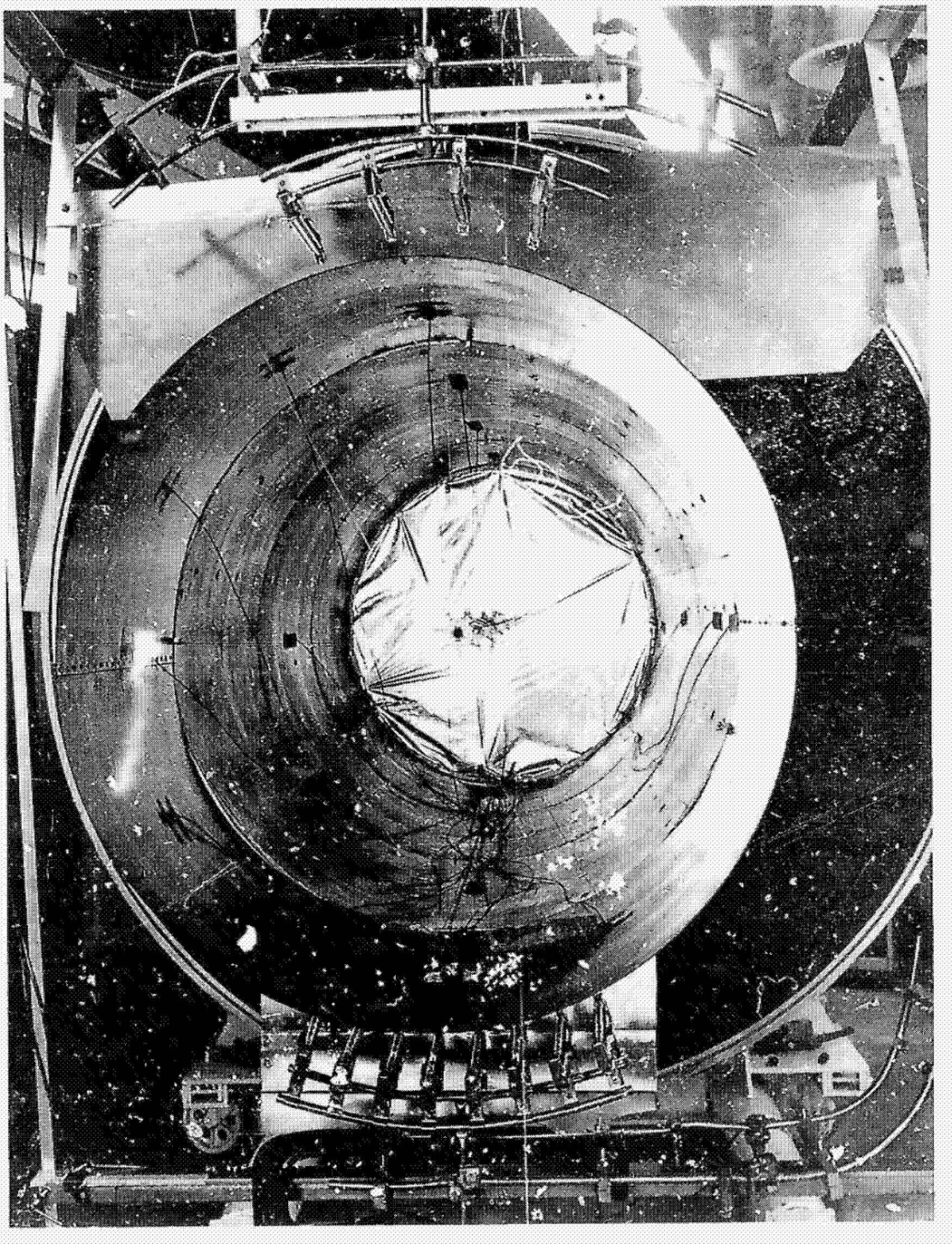


Fig. 22 Chamber Installation of Full-Scale Insulation Test Object



, Interior of Full-Scale Insulation Test Ooject

consideration since large flexures of the stainless steel cylinders could have caused distortion and possible damage to the insulation blanket.

Insulation Details

The multilayer insulation wrap consisted of 36 alternate layers of 0.0064-mm-thick double aluminized mylar and glass-fiber paper (Dexiglas*). This gave a blanket thickness of approximately 1.27 cm with a layer density of 28.3 layers/cm, which in terms of insulation performance gives a minimum effective thermal conductivity (Ref. 13) (or optimum heat flux per unit thickness) for the boundary temperatures of interest to the OTES telescope system. The insulation was attached to the stainless steel skin using a button attachment method as illustrated in Fig. 24. The buttons were located in a square pattern, spaced on 15.2-cm centers, and consisted of 0.081-cm-diameter Teflon monofilament thread and 1.27-cm-diameter, 0.025-cm-thick Teflon disks. The length of the Teflon thread, which determined the maximum density of the insulation blanket (the density between buttons was usually slightly lower), was carefully controlled at 1.27 cm.

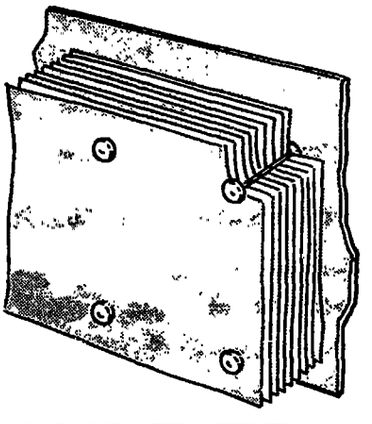


Fig. 24 Detail of Insulation Button Attachment Method

*C. H. Dexter & Sons Paper Co.

In the construction of configuration 1, an important objective was to equip the model with the highest performance insulation wrap practical. To accomplish this, the number of discontinuities in the insulation layers was minimized, and those found to be necessary were designed to produce small perturbations in the insulation performance. All insulation wraps for the test configurations in this program were constructed with a joint (or seam) running longitudinally the length of the test object. For the full-scale insulation model, this joint consisted of four precut nine-layer blankets joined together as shown in Fig. 25. The butt-joint of each blanket was offset with respect to the joints of the other blankets. This produced a discontinuous heat flow path from one side of the wrap to the other and thereby minimized "heat leaks" through the insulation. This type of insulation joint had been evolved in previous programs at LMSC and was found to be less deleterious to insulation performance than the more easily constructed single-blanket butt joint.

An additional overlap butt joint was required for configuration 1 (also used in configuration 2) because the widths of available multilayer insulation materials were smaller than the total length of Sections B, C, and D on the full-scale model. This joint was located at the center of Section C and extended around the model's circumference. Similar to the previous joint, four precut nine-layer blankets were used; however, the method of offsetting the individual butt joints was different than for the previous case. The difference may be seen by comparing Fig. 25 with Fig. 26.

A problem area in multilayer insulated systems such as this is that of reduced performance due to exposed edges and parallel heat flow which occurs in the blanket near these edges. Figure 20 shows the detail of the junction between the end plate and cylinder insulation blankets. To isolate the ends of the multilayer insulation from the surrounding environment and thereby reduce parallel heat conduction near the ends, an intermediary of Dexiglas was used as shown in Fig. 20. This same technique was used to cover the exposed insulation edges of Section B (Fig. 21) during the transient system performance testing.

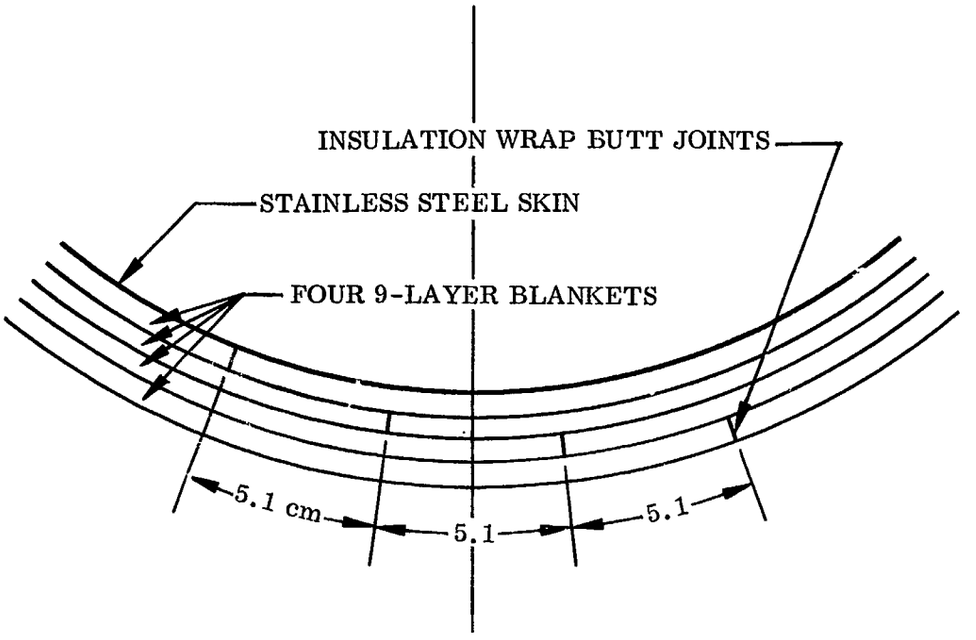


Fig. 25 Detail of Multilayer Insulation Axial Overlap Joint

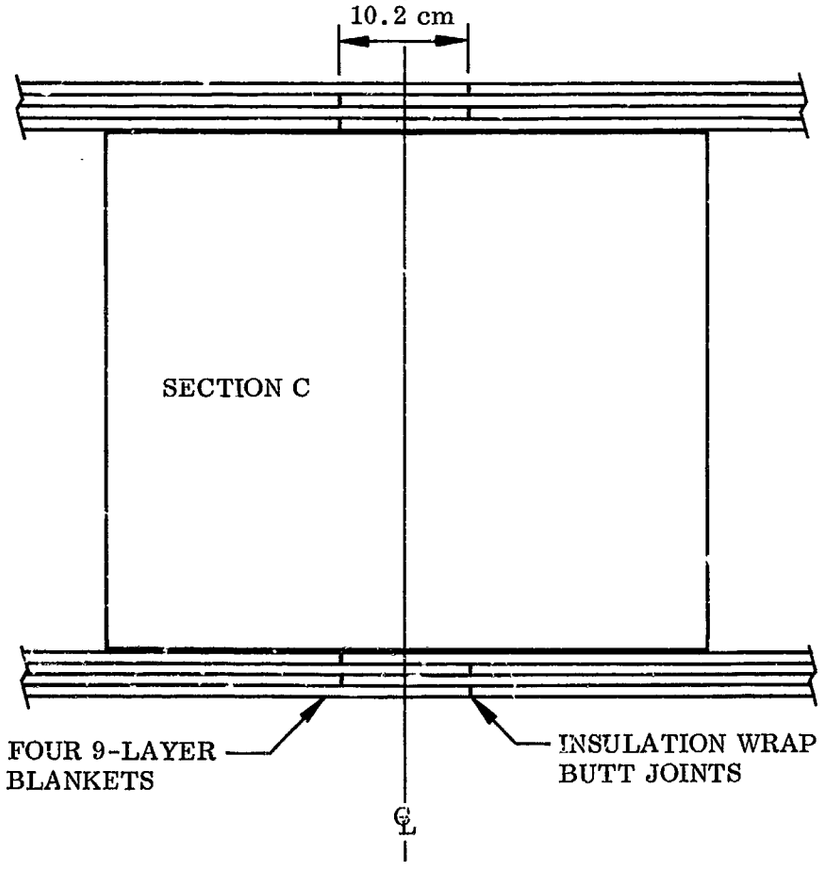


Fig. 26 Detail of Multilayer Insulation Circumferential Overlap Joint

Thermal Control Surfaces

The internal and external surfaces of the four cylindrical sections were painted black to provide the desired surface emittance. Black paint on the internal surfaces of these sections duplicated that which is planned for the prototype OTES telescope. The use of black paint on the exterior surfaces approximated the emittance of the Optical Solar Reflector (OSR) thermal control surface (Ref. 14) that is planned for use on the prototype. The OSR has a high emittance (ϵ) and a low solar absorptance (α_s); however, since solar simulation was not used for these tests, duplication of α_s was not required. For purposes of this experiment, modeling of absorbed heat flux was not a requirement. Instead, various surfaces normally exposed to direct solar heating were temperature controlled. Use of black paint provided the thermal radiation properties required for optimum absorptance of the tungsten lamp energy and for producing the range of boundary temperatures desired for the insulation.

Two different black paint coatings were used. The aluminized mylar surfaces were coated with a silicone paint which produced an ϵ of approximately 0.95. This coating remained flexible after curing and therefore did not crack or chip with flexure of the 0.0064-mm aluminized mylar substrate. The stainless steel cylinders of Sections B, C, and D and the aluminum cylinder of Section A were coated with a black epoxy paint which produced an ϵ of approximately 0.90. This paint was used for the more rigid substrates primarily for convenience in application.

The paint pattern for the internal and external surfaces of the end plates was varied between the one-dimensional and transient test arrangements. For test configuration 1 and the one-dimensional arrangement, the inside surface was painted black and the outside was aluminized mylar. On later configurations (i.e., 3 and 4) this pattern was changed and black was applied to both the internal and external surfaces during the one-dimensional tests in order to simplify the calculation of thermal conductivity. During transient testing of all configurations, the end plate was covered with aluminized mylar on the interior and painted black on the exterior. The highly specular and low emittance aluminized mylar used on the inside of the end plate during transient

testing simulated a similar low emittance surface condition specified for this area of the prototype telescope.

4.3.2 Test Configuration 2

This configuration was tested only for transient performance evaluation. It was identical to the transient test arrangement of configuration 1 except for separation of the insulation between Sections B, C, and D. The same insulation blanket was used for both configurations 1 and 2, with the separations between Sections B, C, and D provided in the latter system by cutting a 0.64-cm-wide gap in two places around the circumference of the model. The gaps (or separations) in the insulation blanket between cylindrical sections were provided in this and the following configurations to simulate a similar condition existing on the OTES telescope. No gaps were provided in test configuration 1 in order that a comparison could be made between systems with separations and systems without separations. Small differences in performance would allow more latitude in construction of the insulation for the complete OTES telescope model. It was postulated that the presence of gaps would have little effect on the model's thermal behavior; however, testing was necessary to verify the assumption. The gaps in the insulation were the same size as the spacing maintained between the stainless steel cylinders. The photograph presented in Fig. 22 shows the circumferential separation gaps in the insulation blanket of this test configuration.

4.3.3 Test Configuration 3

This configuration consisted of an internal multilayer insulation wrap with separation of the insulation between Sections B, C, and D. The one-dimensional and transient test arrangements are shown in Figs. 27 and 28. Except for the insulation being attached to the interior surface of the stainless steel cylinders, this configuration is very similar to test configuration 2. For the one-dimensional arrangement in which thermal conductivity of the wrap was determined, the three sections were butted closely together, thereby slightly reducing the overall length from that of test configuration 1. For transient testing, the cylinders were repositioned with a 0.64-cm-gap

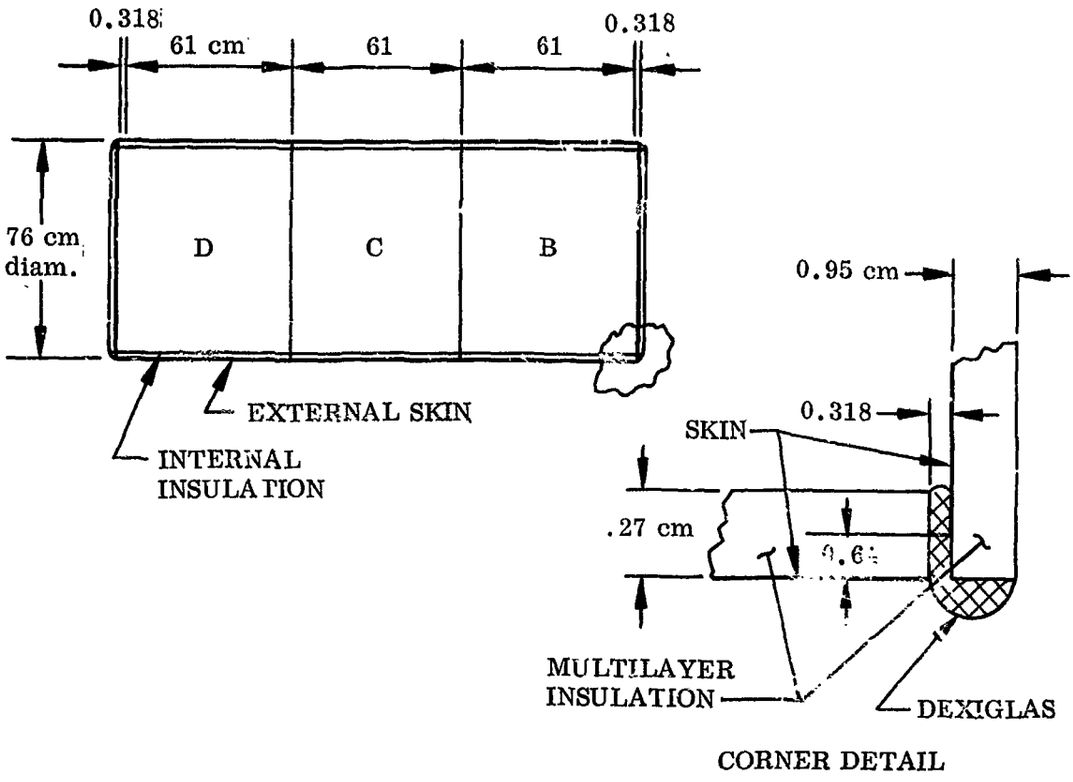


Fig. 27 Configuration 3: One-Dimensional Test Arrangement

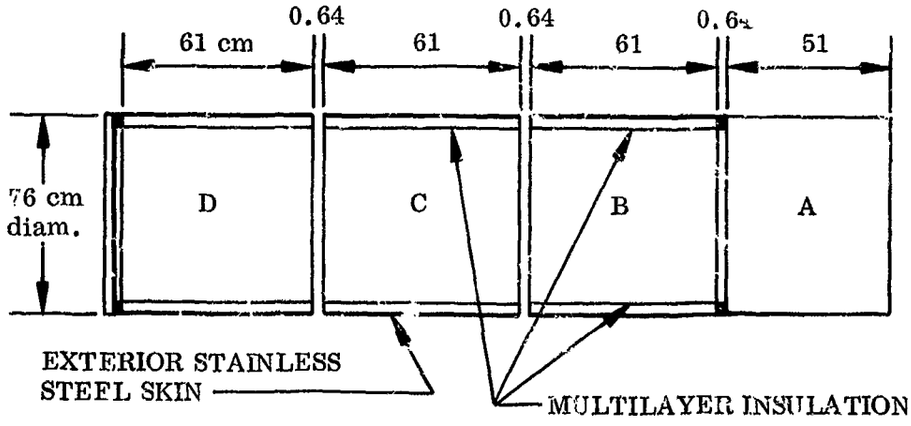


Fig. 28 Configuration 3: Transient Test Arrangement

between sections, the end plate adjacent to Section B was removed, and Section A was attached. Thus, the geometry for the transient test arrangement of both configurations 1 and 2 was reproduced except for the change from an external to an internal insulation wrap. The insulation on the end disks was unchanged from the previous configurations and remained as an external wrap. This was done for convenience of assembly for the one-dimensional arrangement since it had no effect on the thermal conductivity determinations of the cylindrical wrap. During transient testing, the primary purpose of the end plate was to provide an adiabatic wall with a high infrared reflectance (or low ϵ) on the internal surface. An external wrap on the end plate was maintained for all test configurations so that any changes in the transient performance could be related solely to variations in the cylindrical portion of the system.

For the one-dimensional arrangement, all interior and exterior surfaces were painted black including the exterior aluminized mylar surface of the two end sections. Since the interior surface of the stainless steel cylinders had been blackened for the preceding tests, the multilayer insulation now facing the blackened surface was subject to different boundary conditions. In test configuration 1, the inner layer of the externally applied insulation was viewing the relatively low emissivity stainless steel surface. For the internal wrap, the insulation layer next to the cylinder was viewing a high emissivity painted surface. To compensate for this discrepancy, an additional layer of aluminized mylar was interposed between the 36 layers of insulation and the interior surface of the cylinders. This layer of aluminized mylar presented a low emissivity surface to the first layer of the insulation blanket, and since its temperature was close to that of the stainless steel, it reproduced the experimental situation of the external wrap. The paint pattern for the system performance tests was the same as for the previous configurations.

4.3.4 Test Configuration 4

This configuration consisted of a half-scale thermal model of test configuration 3. In designing the model, a "materials preservation" technique was employed. With this technique the model is constructed using the same materials as the prototype. Subsection 5.1 presents the basic thermal modeling laws (Eq. 5.1) and defines the

terminology and the various modeling parameters involved. For the "materials preservation" technique, $K^* = C_p^* = \rho^* = 1$ and the model ratios from Eq. (5.1) become:

$$\frac{V^*T^*}{\theta^*} = I^*A_I^* = Q^* = \frac{A_n^*T^*}{t^*} = A_i^*T^{*4} \qquad (4.1)$$

Then for a geometrically similar half-scale model, $T^* = 1.26$, $\theta^* = 0.25$, and $Q^* = 0.63$.

For the half-scale model constructed during this program, geometric similarity was maintained between the model and the prototype for all components with the exception of the multilayer insulation thickness and a minor distortion in the internal surface area ratios. Geometric similarity of the multilayer insulation blanket could not be maintained due to the dependence of thermal conductivity (K) on the blanket thickness, number of layers, and insulation temperature. Therefore, in order to obtain the desired T^* and Q^* through the wrap, distortion of both the thickness ratio (t^*) and thermal conductivity ratio (K^*) of the insulation blanket was necessary. The criterion employed in design of the model was to maintain $K^*/t^* = 2$. The distortion in t^* for the insulation caused a slight distortion to occur in the area ratio for the internal surfaces; however, in comparison to the overall size of the internal surface area, the effect of the distortion was negligible.

Based on the thermal conductivity results obtained in the one-dimensional steady state testing of configurations 1 and 3, an insulation wrap was selected for the half-scale model consisting of 27 alternate layers of 0.0064-mm double aluminized mylar and Dexiglas spacer material. This resulted in a blanket thickness of 0.95 cm which corresponded to a $t^* = 0.75$ rather than $t^* = 0.50$ as required for geometric similarity. This, obviously, did not provide proper scaling of the heat flow in the wrap parallel to the insulation layers; however, for the telescope system, modeling of K perpendicular to the layers was a more important consideration than modeling of K parallel to the layers.

The insulation blanket was attached to the stainless steel cylindrical skin using the button attachment method described in subsection 4.3.1. Except for length, the button materials and sizes were the same as used for the full-scale system. Use of the 0.081-cm-diameter Teflon thread spaced on 15.2-cm centers modeled the solid conduction heat-flow path. Another approach to modeling the half-scale system would have been to use 0.0405-cm-diameter Teflon thread spaced on 7.6-cm centers. This approach was rejected because of possible performance deterioration of the insulation due to overlapping of the penetration effects. The offset butt joints used for connecting the blanket ends were the same as those used for the larger system, except that only three instead of four precut nine-layer wraps were used for each cylinder.

The transient test arrangement of the half-scale model is illustrated in Fig. 29, which also gives details of the insulation configuration. For the transient arrangement, the end disks were insulated on the exterior as was the case for the previous configuration. In the one-dimensional arrangement, the end disks were insulated on the interior. The photograph in Fig. 30 shows the model's one-dimensional test configuration with end disks in place. The figure also shows the Dexiglas intermediary around the periphery of the ends, which serves to isolate the insulation edges from the external environment. Figure 31 shows a side view of the half-scale model for the one-dimensional test. A comparison of Figs. 22 and 31 gives a good indication of the size differential between the full- and half-scale test objects, even though the test arrangements shown are different.

All thermal control surface characteristics of configuration 3 were preserved in construction of the half-scale model. For Section A, however, an inorganic silicate was used instead of the black epoxy paint because of high temperature requirements for the model. Since both these coatings have similar emittances, the surface properties were unchanged.

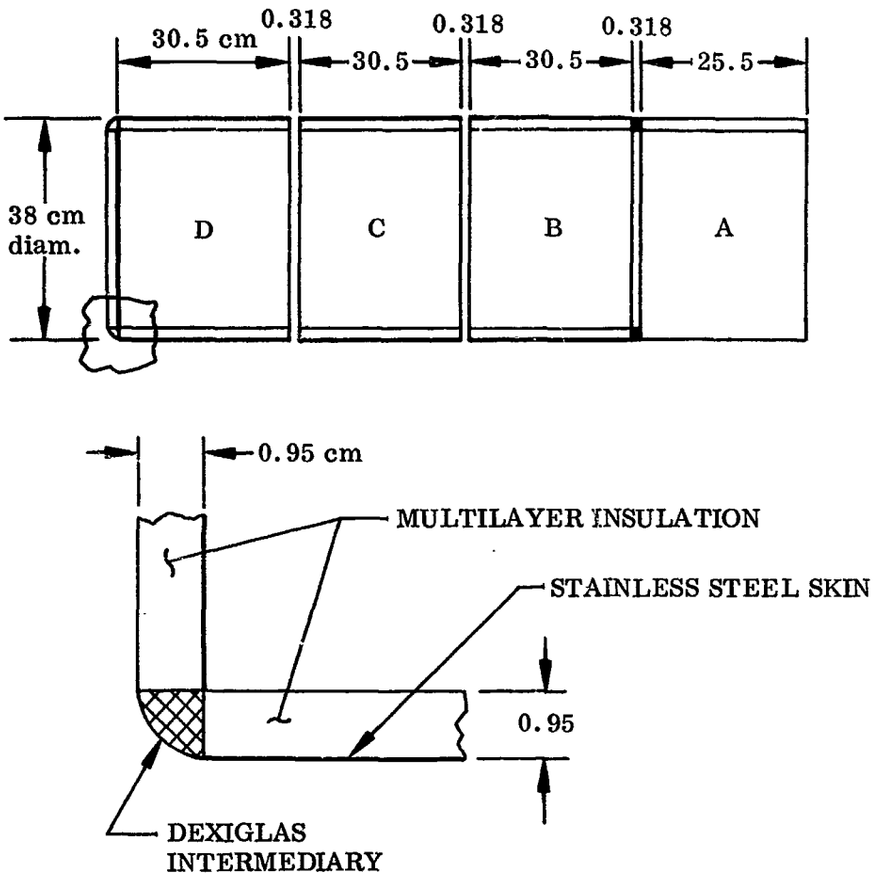


Fig. 29 One-Half Scale Model – Transient Test Arrangement

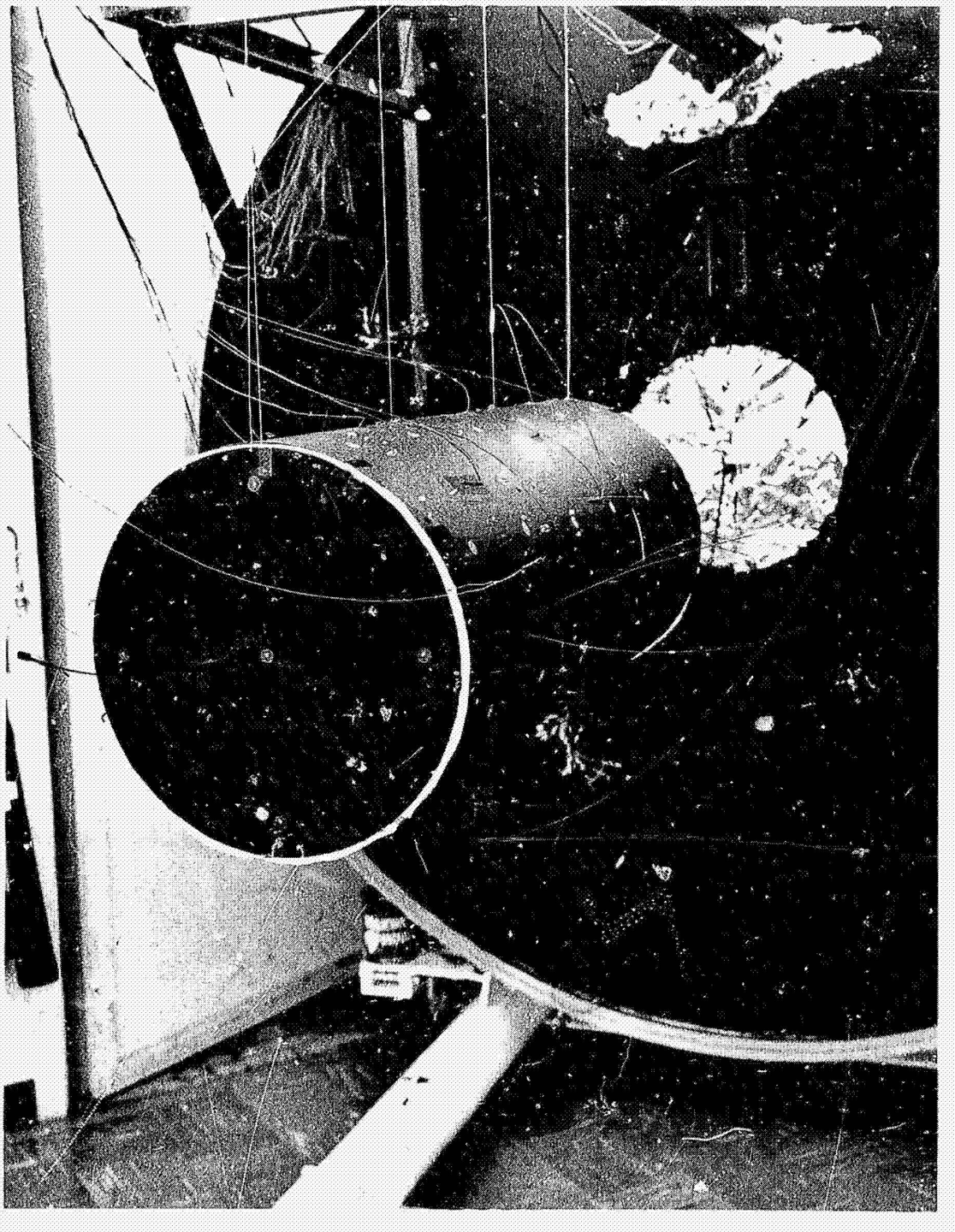


Fig. 30 End View of Half-Scale Model's One-Dimensional Test Arrangement

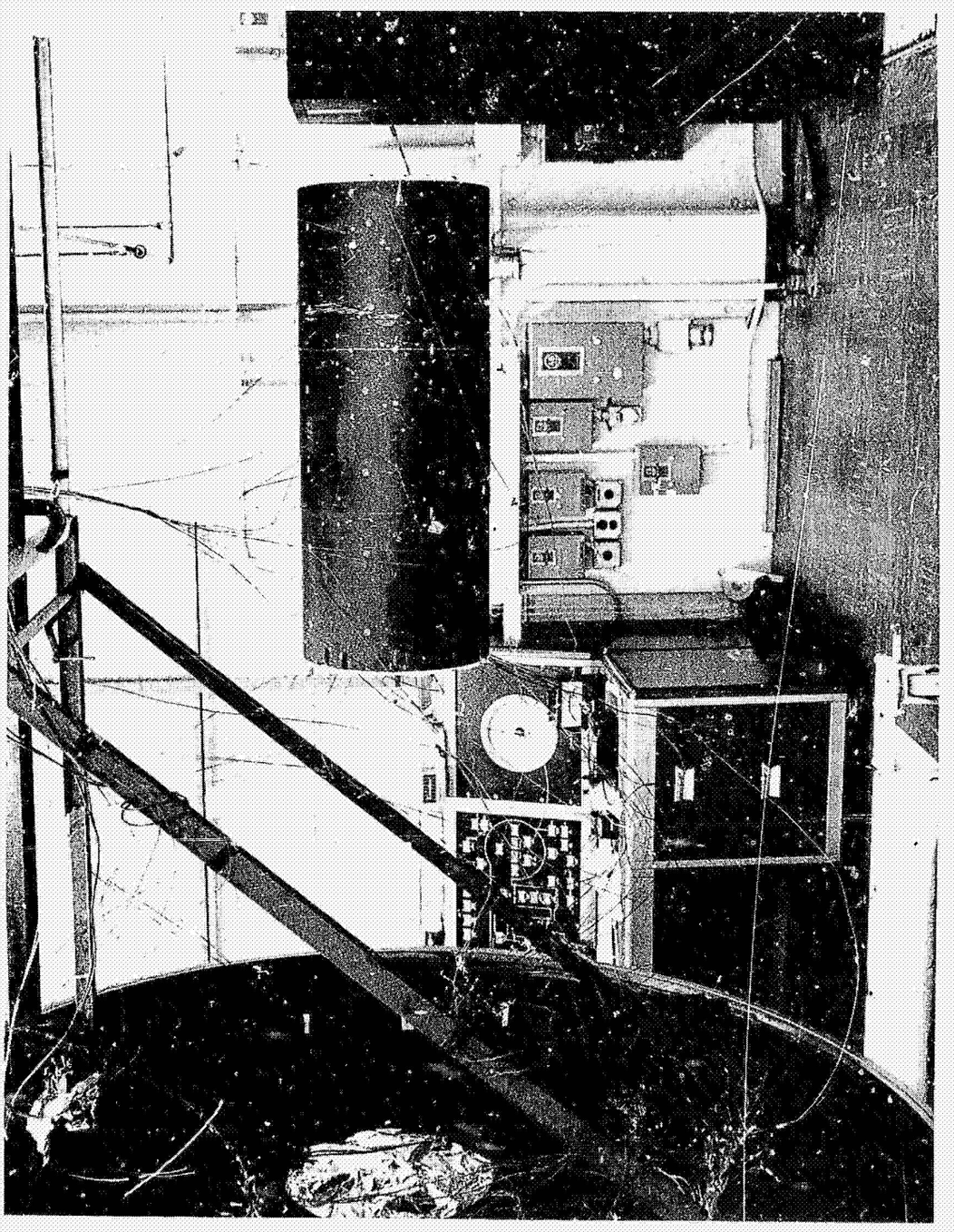


Fig. 31 Chamber Installation of the Half-Scale Model's One-Dimensional Test Arrangement

4.4 TEST PROGRAM

4.4.1 Chamber Installation

The insulation models were tested in a 2.5-meter diameter by 3.1-meter-long vacuum chamber which is equipped with a blackened, liquid nitrogen cold wall. The assembled test models were suspended from an overhead beam attached to the chamber door using stainless steel wire. The models were positioned within the test chamber in a horizontal position as shown in Fig. 22. Testing was done under vacuum conditions of 6×10^{-6} Torr.

4.4.2 Energy Sources

For the one-dimensional test arrangement, energy sources located inside the test objects were used to establish the desired temperature levels. These sources consisted of nine 6-W 115 V tungsten filament lamps for the full-scale system and six 6-W lamps for the half-scale model. The lamps were connected in a parallel circuit and were powered by an ac voltage. For the full-scale system, three lamps were located near the center of each section; for the half-scale model, two lamps were placed at approximately these same relative locations. Positioning the lamps in this manner was found to be adequate for providing the isothermal condition desired for the interior surfaces.

Two separately controlled lamp bank systems were employed during the system performance tests. They consisted of the lamp bank system shown in Fig. 32 for heating the top and bottom areas of Section A and the top lamp bank system shown in Fig. 22 for heating the top exterior surfaces of Sections B, C, and D. The lamps used were G.E. 500 T-3 units having a nominal rating of 500 W at 120 V. These are wound tungsten filament lamps and dissipate on the order of 100 W per linear inch of filament at maximum voltage.

The system used for controlling temperatures of Section A consisted of a top bank with four lamps in parallel and a bottom bank with eight lamps in parallel. Both

Fig. 32 Section A Lamp Bank Location

systems were energized from the same power supply; however, a variac in the circuit between the banks allowed the top bank output to be varied relative to that of the lower bank. The lamps were positioned to give a circumferential temperature profile around Section A based on that predicted for the sun shade section of the OTES telescope just prior to closure of the shutter system described in Section 2. Proper positioning of the lamps around Section A was accomplished by initially setting up the system in air and monitoring surface temperatures. The procedure was repeated under vacuum conditions, both with and without the LN_2 cold wall, until the lamps were positioned to give the desired affect. Although the desired temperature profile was not duplicated exactly, an equivalent emissive power for the interior area of Section A was achieved.

The lamp bank system used to control external surface temperatures for the top region of Sections B, C, and D (Fig. 22) consisted of a row of thirteen lamps extending longitudinally the length of the three insulated sections. This bank was used to provide a temperature condition on the top surface of the model simulating the effect of solar heating with the longitudinal axis perpendicular to the solar vector. Distances from the test object to the lamps were properly scaled in going from the full- to half-scale model. Both the longitudinal lamp bank system and the system heating Section A were shielded such that one bank would not influence the area heated by the other.

Depending on the particular test being run, the lamp banks were either maintained at constant output for average surface temperature control or cycled on and off to provide a square-wave heat input. A Data-Track Model 5300 Programmer* was used to provide the required on-off sequencing of the lamp banks, and a Thermac Controller* was used to maintain the required surface temperature levels.

4.4.3 Instrumentation

Copper-constantan thermocouples were used to monitor temperature behavior of the test objects. Thermocouple locations are shown in Fig. 33 for the transient test

*Research, Inc., Minneapolis, Minn.

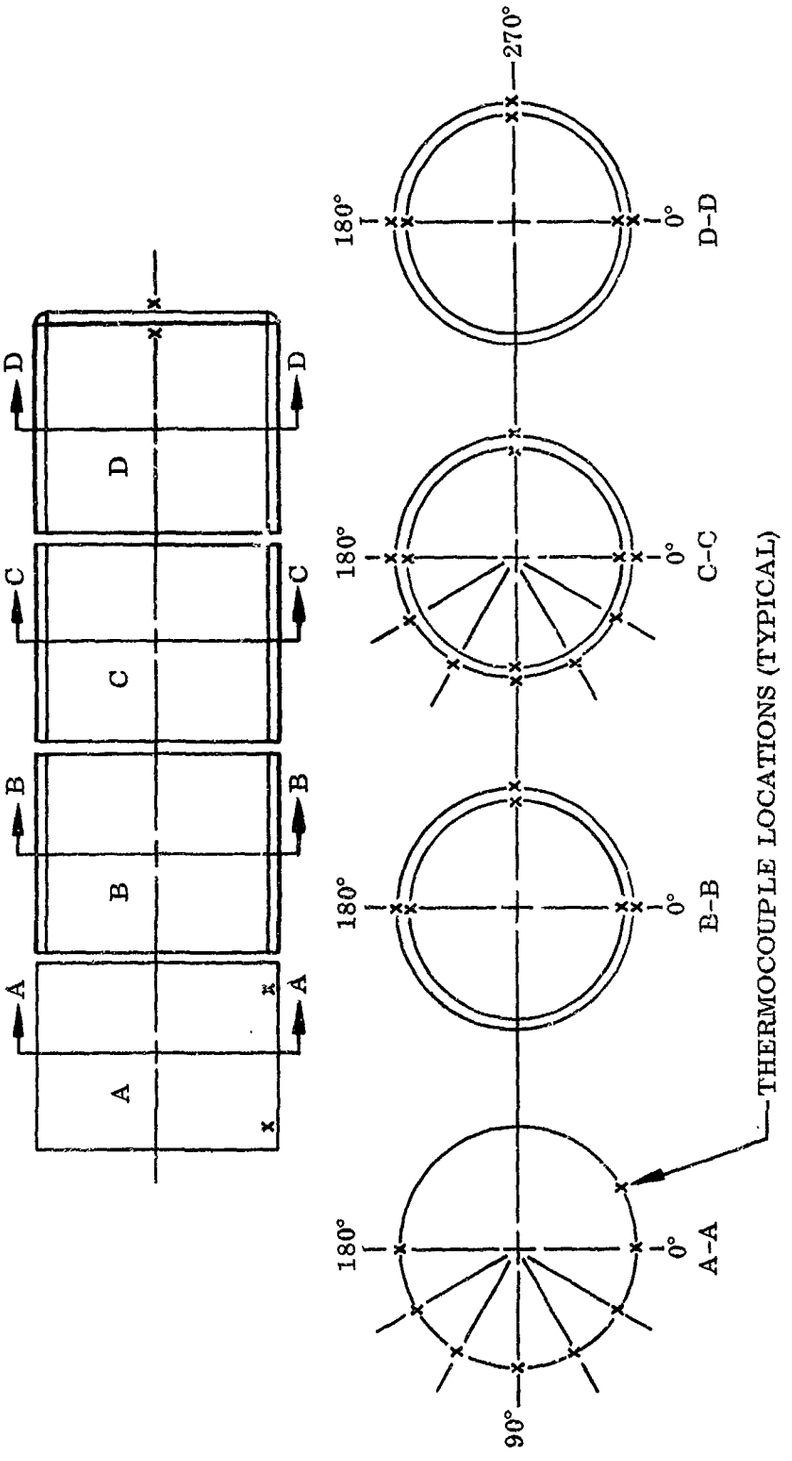


Fig. 33 Thermocouple Locations for System Performance Tests

arrangement. In addition to those shown, thermocouples were also located at the 270-deg position near the ends of Sections B and D, and two were attached to the center shaft. The thermocouples near the ends of Sections B and D were positioned to obtain a qualitative estimate of the parallel heat flow in the insulation near the edges of the blanket. This assessment of parallel heat flow was primarily of interest during the one-dimensional determinations of thermal conductivity.

A total of 42 thermocouples were used for the transient test configuration. For the one-dimensional arrangement, thermocouple locations for Sections B, C, and D were the same as shown in Fig. 33 with additional thermocouples being attached both internally and externally to the end disks near their edges, making a total of 38 for this configuration. The reference junctions of all thermocouples were maintained at 273°K with the use of an ice bath.

Instrumentation used to measure temperature , voltages, current, and power was obtained from the LMSC Research Laboratory Loan Pool and was all of standard design. The performance characteristics of the instrumentation are given in Table 3. Each unit had an up-to-date calibration certification from the LMSC calibration laboratory and was within manufacturing specifications at the time of use.

4.4.4 Test Procedures

Upon installation of a test configuration in the environmental chamber and prior to starting a test series, the system was allowed to degas for at least 24 hr with the chamber at a pressure of $\sim 10^{-6}$ Torr. This procedure was followed to assure that the insulation blanket was thoroughly degassed prior to chilling of the chamber's liquid nitrogen cold wall. Degassing was important since trapped air and moisture between the layers could have degraded the performance of the multilayer insulation.

The tests to determine one-dimensional thermal conductivity were run on configurations 1, 3, and 4. These tests were performed using the internally located lamps to

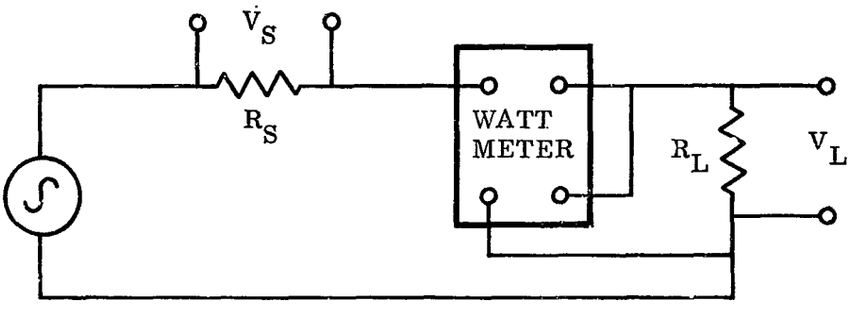
Table 3

INSTRUMENTATION FOR INSULATION EXPERIMENTS

Type	Serial No.	Range	Precision or Accuracy	Use
Wattmeter	MSL 65414	0–12 0–24 0–48	0.1 0.2 0.4	Internal power dissipation
AC Null Voltmeter	LMSC 77629	0–0.5 0–5 0–50 0–500	0.2% 0.2% 0.2% 0.2%	Voltage across internal lamps
Standard Resistor	MSL 15815	1 Ω	0.15%	Current of internal lamp circuit
24 pt. mV Recorder	LMSC 78353	0–10	0.5	Monitor model performance
Digital Voltmeter	LMSC 84069	0–10 mV 0–100 mV	0.03% 0.03%	Model thermocouple response
Portable mV Potentiometer	MSL 54893	0–1020	0.05	Model thermocouple response

establish the desired temperature condition on the interior surfaces of the test objects. Upon achieving steady-state conditions, where the internal and external surface temperatures were constant with time for a given lamp power-setting, thermocouple data were recorded. For each power setting, the time required to achieve steady state conditions was approximately 80 to 100 hr for the full-scale system and 24 to 40 hr for the half-scale model.

Measurement of internal lamp power dissipation was accomplished as illustrated in the following circuit diagram:



where R_L is the resistance of the lamps and R_S is the resistance of a standard resistor. The voltage drops across the standard resistor and lamp assembly were measured with a null balance ac voltmeter with ± 0.2% accuracy. In addition, a wattmeter was used to give a direct indication of the power dissipation by the lamps. The power in the lamps was obtained from the equation

$$P = P_W \left(1 - \frac{V_L}{R_W} \frac{R_S}{V_S}\right)$$

where P_W is the wattmeter indicated power and R_W is the resistance of the wattmeter voltage measuring winding. The term in the parenthesis represents a correction of the indicated power which takes into account the current shunted through the voltage coil of the wattmeter.

The internal power dissipations for the various one-dimensional tests are given in Table 4. For test configurations 1 and 3, steady state temperature data were obtained for three different power settings. For configuration 4, initial testing was also done for three power settings; however, this was followed by an additional series of tests

Table 4

INTERNAL POWER DISSIPATION FOR ONE-DIMENSIONAL TESTS

Q (Watts)		
Configuration 1	Configuration 2	Configuration 4
4.28	4.26	2.04
7.27	7.34	2.32
29.9	30.2	2.74
		3.31
		4.84
		6.87
		8.59
		9.69

in which data were acquired for several more internal power conditions. The additional tests were run to verify previously obtained results and to provide temperature dependence data for thermal conductivity over a wider range of temperatures.

During one-dimensional testing of the internal insulation wrap configurations (i.e., 3 and 4), the spaces between sections were eliminated by butting the cylindrical sections tightly together. This procedure was followed to minimize direct losses of energy through the gaps and to minimize insulation edge effects.

Transient tests were run on all four test configurations. Except for configuration 2 on which no one-dimensional testing was done, transient testing was done immediately following the one-dimensional test series for each particular insulation wrap configuration. Transient performance testing consisted of observing the behavior of the test objects when subjected to controlled cyclic heating and cooling conditions. Two distinctly different external energy rates were employed. In the first, Section A was cycled between maximum and minimum temperatures while the top exterior of Sections B, C, and D were subjected to a constant incident heat flux which was set to provide a given average temperature level.

For the second case, Section A was held at an average temperature while the top exterior of the other three sections was cycled between maximum and minimum temperatures. In both cases, thermal cycling of the model was accomplished by a square-wave heat flux input from the lamp bank systems. Test conditions for the system performance tests are given in Table 5. Figure 34 presents the temperature distribution on Section A for the full- and half-scale test objects. For the half-scale model, both the actual test profile and the profile required from scaling the prototype's distribution are shown.

Table 5

TEST CONDITIONS FOR TRANSIENT PERFORMANCE TESTS

Test Run		Full-Scale (test)	Half-Scale (required)	Half-Scale (test)
Section A cycled and top exterior of Sections B, C, D constant heat flux	Equivalent emissive power (W/cm^2) of Section A during lamps on cycle	0.911	2.296	2.267
	Average temperature (°K) of top exterior of Sections B, C, D	212	267	270
Section A constant heat flux and top exterior of Sections B, C, D cycled	Equivalent emissive power (W/cm^2) of Section A	0.274	0.69	0.708
	Temperature (°K) of Sections B, C, D during lamps on cycle	285	359	363

The total transient period for the full-scale system was 24 hr which consisted of the lamps on for 12 hr and off for 12 hr. For the half-scale model, the transient period was one-quarter that of the larger system or 3 hr of heating and 3 hr of cooling. Temperatures at selected points on the models were monitored just prior to the lamps turning off at the end of the heating cycle and again just prior to the lamps turning on at the end of the cooling cycle. Cycling of the system was continued until the model's temperatures became repeatable from cycle to cycle. When this occurred, the system

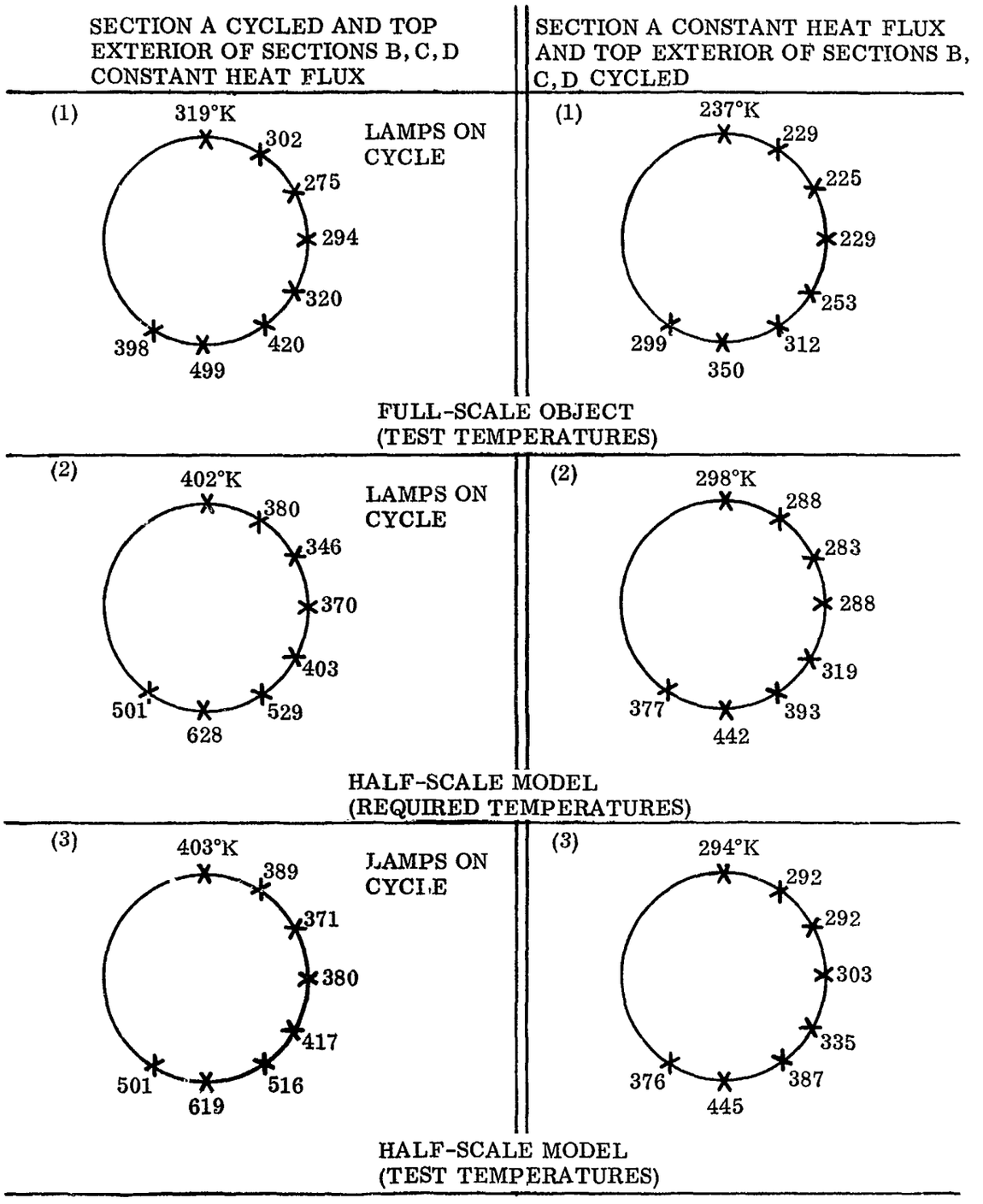


Fig. 34 Section A Temperature Distributions, °K

was considered to be in equilibrium, and data for all thermocouples were recorded. In addition, at this time, selected thermocouple data were recorded continuously throughout the next complete transient cycle.

4.5 ONE-DIMENSIONAL HEAT FLOW TEST RESULTS

In this section results are presented for the one-dimensional, steady state heat flow tests which were obtained for configurations 1, 3, and 4. The primary objective of the tests was to determine a functional relationship between the length scale ratio and the multilayer insulation thickness (t*) for one-dimensional heat flow. Although the thickness parameter was used in the study, it would have been just as appropriate to use the number of layers since the layer density of the insulation wrap was assumed constant. To accomplish this objective it was necessary to determine the effective thermal conductivity of the full-scale insulation as a function of hot and cold boundary temperatures. During the tests, the hot boundary temperature was set at various levels to encompass the temperature ranges predicted for the prototype telescope and the complete thermal model of the prototype telescope. The information obtained from testing the full-scale model was then used to predict an insulation thickness for a half-scale insulation model which was fabricated and tested to verify the analytical predictions. The results obtained from testing the two insulation models were extrapolated to a 1/6.43-scale insulation system and applied to the design and construction of the OTES model described in Section 5.

The test results are presented in chronological order with a detailed exposition of results from test configuration 1 given first. Following the presentation of test results, the correlation for modeling the insulation is derived from a comparison of results obtained for configurations 3 and 4.

4.5.1 Configuration 1 Test Results

Three internal power settings were used to obtain three sets of steady state equilibrium boundary temperatures. The power levels were chosen to give an inner (hot) boundary

temperature, T_H, of 220, 275, and 405°K. During these tests the 16 thermocouples, which monitored the interior temperatures, indicated a maximum diferenct of 0.6°K from the average temperature, with a maximum temperature spread of 0.8°K.

Temperatures measured on the outside of cylinders C and D are plotted in Fig. 35 for the high and low power inputs. The large circumferential gradients shown arise primarily from the presence of local hot regions in the liquid nitrogen cooled chamber walls. During succeeding runs, the chamber was instrumented and the principal hot area was identified as the diffusion pump inlet to the chamber. The influence of the inlet was essentially centered on Section C and was positioned at the 225-deg position corresponding to the peak in the temperature profile as shown in the figure.

The outer boundary temperature of the insulation, when completely surrounded by a cold wall ($T_{wall} \sim 85°K$), was calculated from an energy balance relationship to be 105°K which is close to the temperature measured at the 30 deg position or coldest part of Section C. The circumferential gradient of Section D was less than that of Section C because the view factor from this section to the pump inlet was smaller. The low temperature point of Section D was warmer than that of the other sections because of its location near the chamber door and also due to the presence of nearby uncooled support structure as shown in Fig. 22. The average temperature of Section D, however, was close to that of Section C. Section B ran somewhat cooler than D, but with about the same temperature profile. This occurred because Section B had a negligible view of the support structure as well as a small view of the pump inlet.

The external temperatures of the insulated end disks were also higher than expected and exceeded the cylinder temperature by as much as 26°K. The cause of this was traced to a relatively hot area in the center of each chamber door.

To analyze the perform nce of the multilayer insulation, it was necessary to specify the outer boundary temperature by some average value. An exact analysis would have required an extensive thermal network calculation in order to account for the presence of two-dimensional heat flow. This was impractical both from the standpoint of the

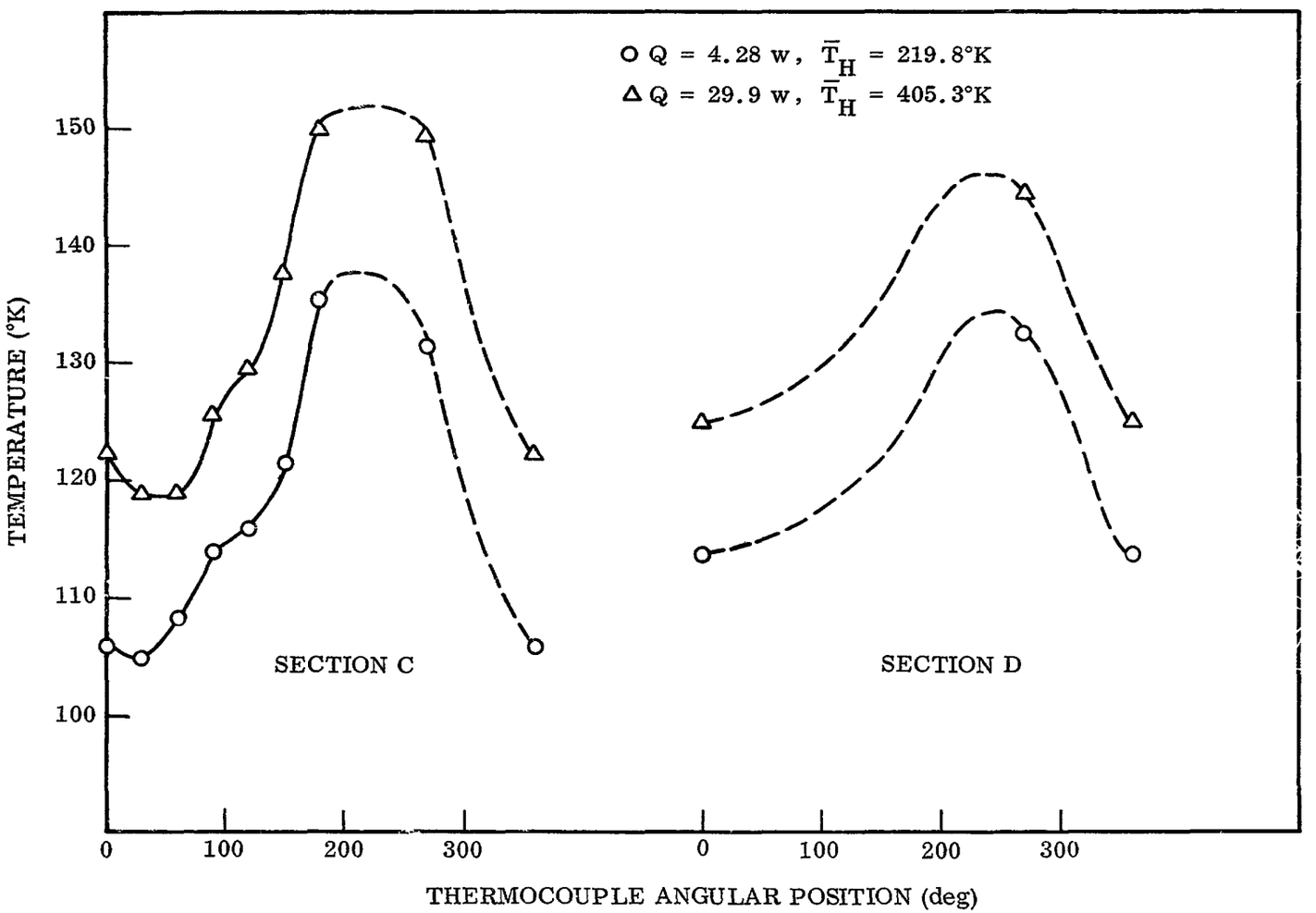


Fig. 35 Test Configuration 1; Exterior Temperatures for One-Dimensional Heat Flow Test

effort involved and the uncertainty of arriving at any better results with the available input information. The average exterior temperature of Section C was taken from the data plot of Fig. 35. Since only three temperatures were measured for Section B and D, their average temperatures were estimated by scaling the average of Section C in proportion to the temperature differences between the three temperatures of Section B (or D) and the three corresponding temperatures of Section C.

Analysis of the data to obtain thermal conductivity was accomplished by dividing the heat flow through the insulation into two parallel flows given by the equation:

$$Q = \frac{A_e K_e}{t_e} \overline{\Delta T}_e + \frac{A_c K_c}{t_c} \overline{\Delta T}_c \qquad (4.2)$$

where the subscripts e and c refer respectively to the ends and cylinders. The value of K_e was taken as

$$K_e = HK_c$$

where the proportionality constant H is a function of the relative layer densities and boundary temperatures. From previous work on multilayer insulation (Ref. 13), H was taken as 1.25 due to the higher layer density of the ends (36.6 layers/cm as compared to 28.3 layers/cm for the cylinders).

The effective thermal conductivity of the cylindrical portion of the wrap was calculated from

$$K_c = Q\left[\frac{A_e H\overline{\Delta T}_e}{t_e} + \frac{A_c \overline{\Delta T}_c}{t_c}\right]^{-1} \qquad (4.3)$$

The temperature dependence of K_e/K_c was taken into account by first neglecting this influence to establish approximate values of K_c as a function of temperature and then

iterating the calculation using the approximate temperature dependence established from the first calculation. The largest change in H due to the temperature effect was 8% as a result of a 30°K higher outer boundary temperature. Due to the smaller area of the end sections, this lowers the K_c value by only 1%. The resultant effective conductivity values are summarized in Table 6 along with the average hot and cold boundary temperatures ($\bar{T}_H$ and $\bar{T}_c$) of the cylindrical sections.

Table 6

SUMMARY OF ONE-DIMENSIONAL TEST RESULTS FOR CONFIGURATION 1

Q (Watt)	$\bar{T}_H$ (°K)	$\bar{T}_c$ (°K)	$\bar{T}_e$ (°K)	K_c (W/cm-°K $\times 10^{-6}$)
4.28	219.8	121.2	147.0	1.01
7.27	274.4	122.9	149.7	1.10
29.9	405.3	133.4	160.3	2.47

4.5.2 Configuration 3 Test Results

The insulation for this test configuration was wrapped internally using the same stainless steel cylindrical skin as used for configuration 1. It therefore had a slightly smaller effective area than that of previous configurations. In addition, this configuration had two circumferential butt joints at the interfaces between Sections B and C and between Sections C and D.

The outer boundary temperature profiles were similar to those of the external wrap configuration with the exception that the circumferential gradients were reduced by as much as a factor of 2 as shown in Fig. 36. The suppression of the gradients resulted from the relatively high thermal conductivity of the skin which was located on the cold boundary side of the insulation for this configuration. The interior temperatures were again uniformly isothermal.

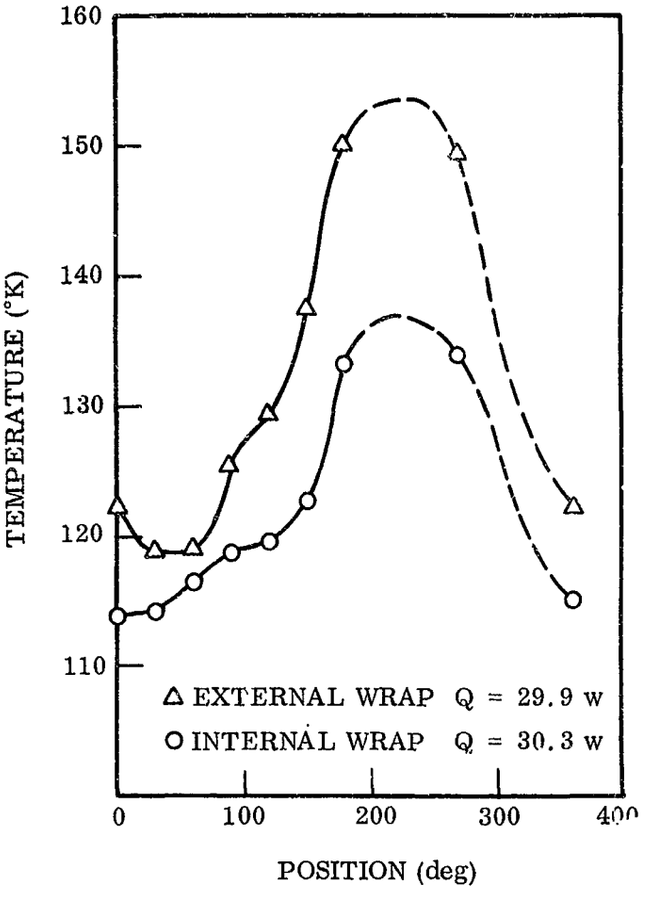


Fig. 36 Comparison of Exterior Temperatures for One-Dimensional Heat Flow – Test Configurations 1 and 3

For this configuration, the end sections were blackened on the exterior. This resulted in the end temperatures running closer to the average cylinder temperature and showing less variation with input power.

Again, three data points were obtained, and the effective conductivities calculated following the same procedures as used for test configuration 1. The average temperatures and conductivities are presented in Table 7.

Table 7

SUMMARY OF ONE-DIMENSIONAL TEST RESULTS
FOR CONFIGURATION 3

Q (W)	$\bar{T}_H$ (°K)	$\bar{T}_c$ (°K)	$\bar{T}_e$ (°K)	K_c (W/cm-°K $\times 10^{-6}$)
4.26	219.8	120.5	140.1	1.06
7.34	267.8	120.6	140.0	1.21
30.2	410.1	128.4	143.1	2.60

Previous investigations of multilayer insulation systems (Ref. 15) have shown that the effective thermal conductivity, as measured in the present experiments, can be related to the boundary temperatures by

$$K_e = An^2(T_H + T_C) + B \frac{\sigma}{n(N - 1)/N} \left(T_H^2 + T_C^2\right)(T_H + T_C) \qquad (4.4)$$

in which the solid conduction and radiative heat transfer are treated as parallel heat flows. In this equation, n is the layer density (layers/cm), N is the total number of layers, and σ is the Stefan-Boltzman constant. The coefficients A and B are functions of the properties of the specific multilayer components and were treated as constants. In the work of Ref. 15, the coefficients have been experimentally evaluated, allowing Eq. (4.4) to be written as

$$K_e = 0.370 \times 10^{-9} (T_H + T_C) + 1.75 \times 10^{-3} \sigma \left(T_h^2 + T_C^2\right)(T_H + T_C) \qquad (4.5)$$

in which $n = 28.3$ layers/cm and $N = 36$ have been used. The type of insulation for which the above equation was derived was an aluminized mylar/Dexiglas insulation system with no button attachments or insulation joints. From practical experience, this insulation would be expected to have a lower conductivity than the insulation tested for the present program.

The test results obtained for configurations 1 and 3 are compared in Fig. 37 to thermal conductivity values calculated using Eq. (4.5). In Fig. 37, thermal conductivities have been plotted against the radiative potential $\sigma\left(T_H^2 + T_C^2\right)(T_H + T_C)$. The values from Eq. (4.5) follow essentially a linear behavior, especially at higher temperatures.

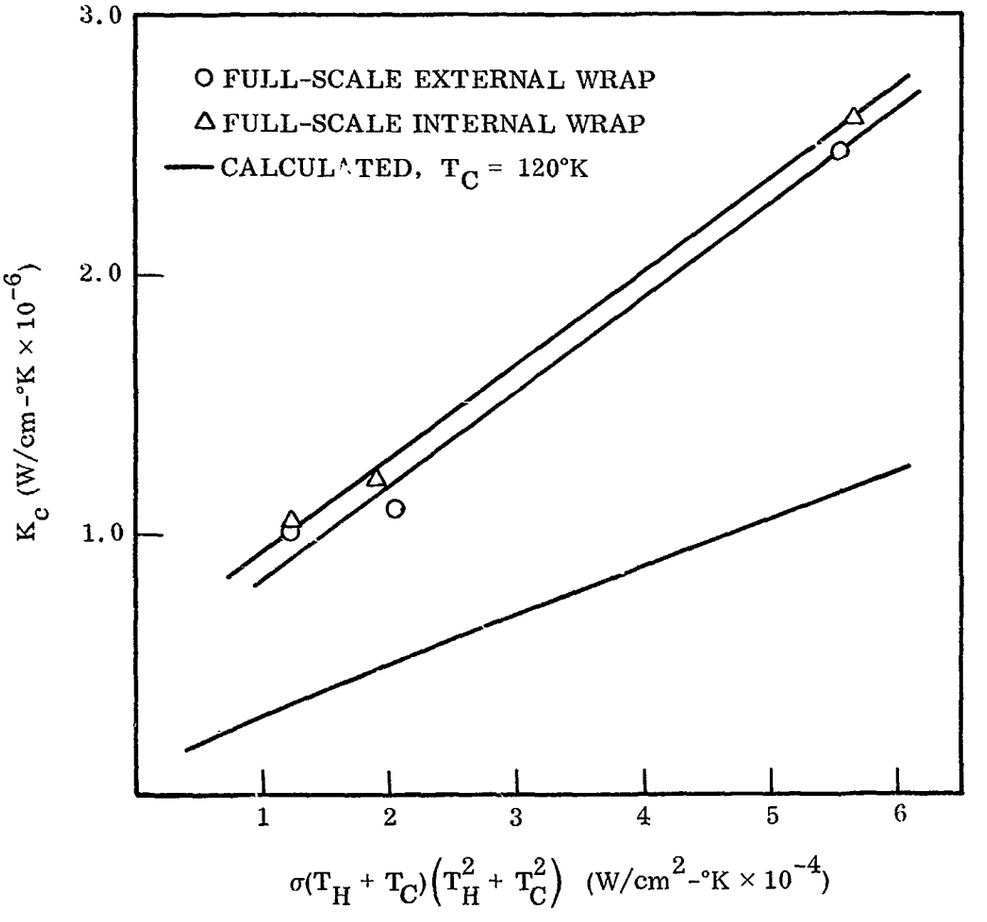


Fig. 37 Insulation Thermal Conductivities for the Full-Scale Interior and Exterior Wraps

The straight line representations of the experimental data show that the external wrap was slightly better in insulative performance. This would be expected for several reasons which include the presence of two butt joints in the internal wrap and the difficulty in constructing the internal wrap with the quality of the external wrap. Errors associated with the experimental determination of the parameters involved in calculating any one point of Fig. 37 are small enough so that the true value lies within the circle inscribing the plotted point. However, the largest uncertainty in an experiment of this type is that of determining when steady state conditions have been reached. In the course of an experiment involving multilayer insulation, the temperatures may appear to have stabilized when in fact a sizable transient is propagating through the insulation. An inspection of the data indicates that this was the case for the mid-temperature point of the external wrap.

4.5.3 Configuration 4 Test Results

For materials preservation modeling the scaling criterion for the insulation may be stated as

$$\frac{K^* A_n^*}{t^*} = L^* \tag{4.6}$$

or since the distortion of the insulation area is small, $A_n^* = L^{*2}$ and Eq. (4.6) becomes

$$\frac{K^*}{t^*} = \frac{1}{L^*} \tag{4.7}$$

Since it is impossible to maintain $K^* = 1$ and have strict geometrical identity with $t^* = L^*$, it is necessary to distort t^* in accordance with Eq. (4.7) once the value of K^* has been determined.

Values for K^* were generated from the data of Fig. 37 as a function of the full-scale insulation temperatures. The hot boundary temperature of the full-scale model was assumed to scale upwards by $(1/\pi^*)^{1/3} = 1.26$ in designing the half-scale model. The cold boundary temperatures were assumed unaffected by the scaling since the half-scale model was closely coupled to the unscaled liquid-nitrogen cold wall. Also, any small changes in T_C will not affect the value of K^* since K is a weak function of T_C for the present case.

Results of the calculation for three temperatures modeled to $T'_H = 1.26\ T_H$ are given in Table 8 as K^*_{meas}. In this table $P = \sigma(T_C + T_H)\left(T_C^2 + T_H^2\right)$, and the primed quantities refer to the half-scale model. For comparison, K^*_{calc} values are included which were derived from the calculated conductivity curve of Fig. 37. The agreement between K^*_{meas} and K^*_{calc} is apparently fortuitous. In the range of 220 to 335°K, the variation of K^* is 20%. For the design of the half-scale model, a mean T_H of 270°K was taken as the model point with the resultant $K^* = 1.42$.

From Eq. (4.7), the t^* value can be defined as $t^* = 0.71$, and since the total number of layers, N, is proportional to t

$$\begin{aligned} N' &= Nt^* \\ &= (36)(0.71) \\ &= 25.6 \end{aligned}$$

Table 8

COMPARISON OF MEASURED AND CALCULATED THERMAL CONDUCTIVITY MODEL RATIOS (K^*)

T_C (°K)	T_H (°K)	T'_H (°K)	P (W/cm^2-°K $\times 10^{-4}$)	P' (W/cm^2-°K $\times 10^{-4}$)	K^*_{meas}	K^*_{calc}
120	220	277	1.21	2.05	1.30	1.46
121	270	340	1.94	3.41	1.42	1.57
125	335	422	3.34	6.01	1.54	1.68

The actual wrap used for the half-scale model consisted of 27 layers of insulation with $t^* = 0.75$. This was done so that any necessary adjustment in the insulation could be accomplished by removing layers rather than adding layers.

During the half-scale model testing, additional temperatures were measured on the external surfaces in order to obtain a better definition of the temperature profile. A typical profile for Section C is shown in Fig. 38 and compared to an equivalent power input of $Q_m = 0.64\, Q_p$ from the full-scale internal wrap. Although the Q/A for the half-scale system had increased by 2 :6, the external temperatures were relatively unaffected as the smaller model was less affected by the hot areas of the chamber. In fact, the increases in average temperature were less than 2%.

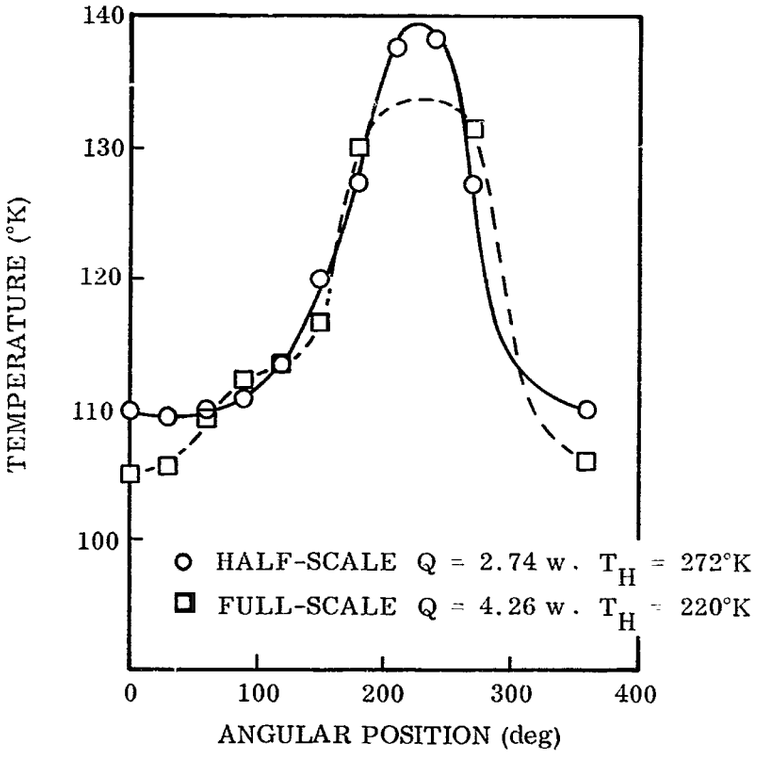


Fig. 38 Comparison of Exterior Temperatures for One-Dimensional Heat Flow – Test Configurations 3 and 4

The data for the half-scale tests are presented in Table 9. Eight data points were acquired in an attempt to determine the validity of using a linear relationship between the thermal conductivity and the radiation potential. The previous data for the full-scale models showed some indication of an increasing slope with increasing P (radiative potential). This would be an opposite behavior from the calculated curve of Fig. 37, and could only result from some experimental inconsistency in temperature or power measurement.

Table 9

SUMMARY OF ONE-DIMENSIONAL TEST RESULTS
HALF-SCALE INSULATION MODEL (CONFIGURATION 4)

Q (W)	$\bar{T}_H$ (°K)	$\bar{T}_{cyl}$ (°K)	$\bar{T}_e$ (°K)	K_c (W/cm-°K $\times 10^{-6}$)
2.04	243.7	120.4	130.7	1.24
2.32	254.4	121.1	129.8	1.31
2.74	271.6	122.0	132.5	1.37
3.31	291.5	123.0	133.6	1.47
4.84	336.6	125.1	135.1	1.71
6.87	382.0	126.3	136.1	2.01
8.59	406.3	128.7	136.3	2.16
9.69	428.5	130.1	139.7	2.42

The conductivities are plotted against the radiative potential in Fig. 39, showing that experimental data is self-consistent and closely fits a linear relationship. A comparison of these results with those obtained for the full-scale insulation tests shows that the slope of the conductivity curve has decreased by approximately 30%. This behavior is puzzling since the only mechanisms (i.e., heat leakage around joints and two-dimensional heat flows) to account for this behavior which are functions of scaling would be expected to produce an opposite trend. This being true, a probable explanation is that the half-scale insulation was physically different and in fact had a different temperature dependence, such as would arise from a lower layer density as indicated by Eq. (4.4). The difference cannot be attributed to the total number of layers used for the model since a change in N of a few layers would only represent a 1% change in K.

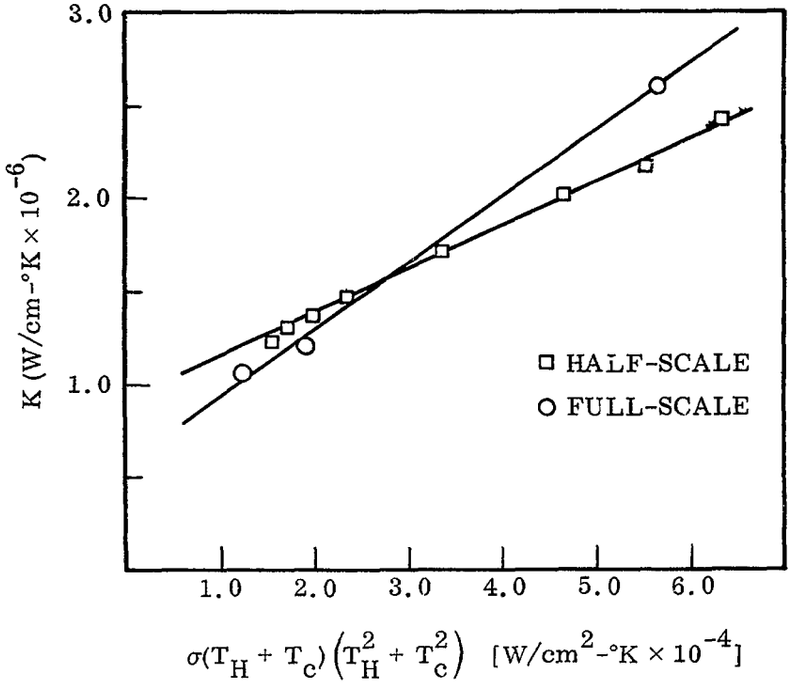


Fig. 39 Insulation Thermal Conductivities for the Full- and Half-Scale Interior Wraps

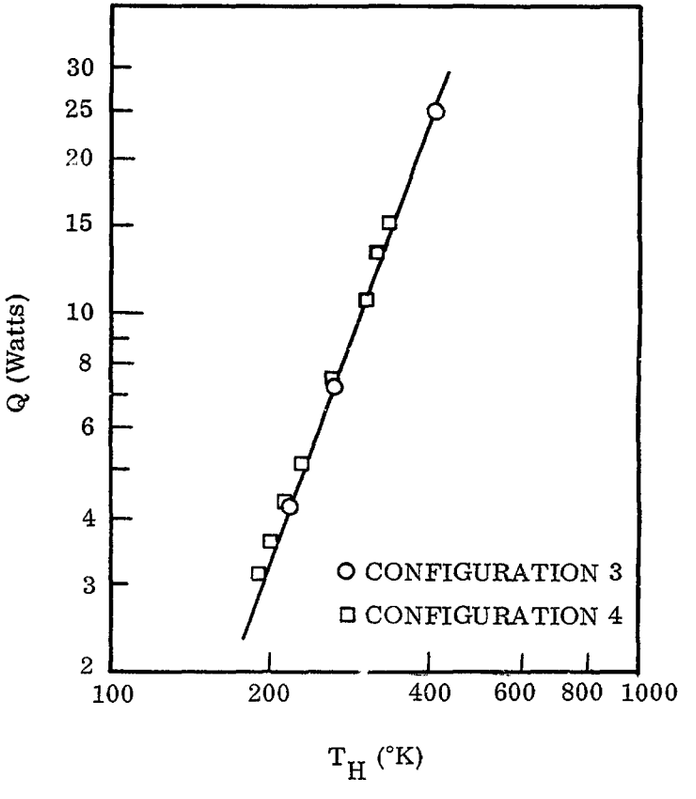


Fig. 40 Correlation of Internal Temperatures for One-Dimensional Heat Flow; Test Configurations 3 and 4

A comparison of the interior hot boundary temperatures for the half- and full-scale tests is made in Fig. 40. The total heat input and temperatures of the half-scale tests have been multiplied by 1/0.63 and 1/1.26, respectively, to produce a direct comparison to the full-scale results. A straight line has been drawn through the three points of the full-scale tests and can be used to estimate the deviation of the one-half scale model points. It is evident that good agreement is attained with the half-scale temperatures falling slightly below the full-scale temperatures.

4.5.4 Insulation Design for the 1/6.43-Scale Model

The OTES thermal model discussed in Section 5 was designed with an overall length ratio $L^* = 1/6.43$. To provide an insulation wrap which would nominally model the OTES prototype insulation system, the data from the multilayer experiments were utilized to provide scaling criteria for specifying the number of layers. The more precisely defined thermal conductivity versus radiative potential curve for the half-scale insulation model was used in characterizing the prototype insulation.

The boundary temperatures of the prototype insulation were in some cases much lower ($\sim 60°K$) than could be achieved in the test chamber with a liquid nitrogen cold wall. It was therefore necessary to extrapolate the data of Fig. 39 down to $P = 0.36 \times 10^{-4}$. This was done in two ways: (1) the extrapolated curve was allowed to fall to zero as P approached zero in the same manner as the calculated curve of Fig. 37 (this extrapolation was based on evidence that the knee of the thermal conductivity curve begins in the region of the lowest temperature data points); and (2) the extrapolated curve was continued in a linear fashion. With the first approach, K^* equals 2.36 for a radiative potential of $P = 0.56 \times 10^{-4}$ which corresponds to the prototype mean operating temperatures. For the boundary temperature extremes, K^* remains fairly constant, giving values of 2.35 and 2.56 for radiative potentials of 1.02×10^{-4} and 0.63×10^{-4}, respectively. This behavior is coincidental with the prototype temperatures being in the region of sharply decreasing K. The second approach of using a linear extrapolation yield a K^* of 1.67 for the mean temperature point and K^* values of 2.11 and 1.46 for the high and low temperature extremes.

To determine the configuration of insulation wrap for the model, $K^* = 2.36$ was used, giving

$$t^* = K^*L^* = 0.367$$

From Eq. (4.7), the number of layers was determined to be

$$\begin{aligned} N_m &= N_p t^* \\ &= (36)(0.367) \\ &= 13.2 \end{aligned}$$

N_m was further reduced because of the $N/(N-1)$ dependence of the radiative term in Eq. (4.5). This has the effect of reducing N_m by a maximum of 5% to 12.5 layers.

From the previous considerations, a 13-layer wrap for the model was decided upon. The distortion that this induces into the transient response of the insulation may be found from

$$\frac{\rho^*V^*C^*T^*}{\theta^*} = \frac{K^*A_n^*T^*}{t^*} \tag{4.8}$$

The volume ratio is $t^*A_n^*$ so that

$$\theta^* = \frac{t^{*2}}{K^*}\rho^*C^* \tag{4.9}$$

and since $t^* = K^*L^*$ and $\rho^* = 1$, this gives

$$\theta^* = K^*C^*L^{*2} \tag{4.10}$$

From Eq. (4.10) it can be seen that the transient response is distorted from exact materials preservation modeling by C^*K^*. For the present case in designing the insulation for the OTES thermal model, $L^* = 1/6.43$, $C^* = 1.88$ (Ref. 13), and $K^* = 2.36$. This results in an insulation time scale ratio of $\theta^* = 1/9.35$ as compared to a value of $\theta^* = 1/41.3$ which is obtained for the case of pure materials preservation and exact geometric similarity modeling.

4.6 TRANSIENT PERFORMANCE TEST RESULTS

Figures 41 through 44 present the transient thermal histories observed on the four configurations for the test condition consisting of temperature cycling of Section A while the top exterior surfaces of Sections B, C, and D are exposed to constant heat flux. The data represent the transient behavior after the system had reached a state where the temperature data were repetitious from cycle to cycle. It can be seen that emission of energy from Section A caused periodic heating of the interior of Sections B, C, and D. It is interesting to note that internal cycling of the three insulated sections had only a minor influence on external surface temperatures. The exterior top surfaces exhibited essentially no change in temperature while the bottom surfaces experienced fluctuations on the order of ± 7 to $\pm 10°K$, depending on the test configuration observed. At 115°K, the $\pm 10°K$ temperature change, for a surface emittance of 0.9, is directly related to a change in flux density of $\Delta Q = 3.34 \times 10^{-4}$ W/cm^2 (1.06 Btu/hr-ft^2). A similar change in flux density for the top surface ($\bar{T} = 214°K$) would cause a change in temperature $\Delta T = 1.6°K$. This small influence would not be accurately recorded by the monitoring instrumentation which had a range of 10 mV and a least count of 0.05 mV ($\approx 1°K$).

A comparison of configurations 1 and 2 (Figs. 41 and 42) shows a difference in their respective transient cooling cycles, with the latter configuration reaching lower temperatures at the end of the cooling period. This difference in behavior was caused by a small amount of energy unknowingly being emitted from the lamp system of Section A. The sharp leveling off of Section A temperatures during the cooling cycle strongly indicated that the lamps were not being completely turned off, even though visually the lamp bank appeared not to be on. Examination of the lamp controller unit at the start of configuration 2 testing disclosed that a bad diode was causing the system to operate incorrectly. The defective component was replaced and the controller operated properly during the remaining transient tests. Retesting of configuration 1 was not thought to be necessary since during the transient heating period the thermal behavior was very similar to that of configuration 2, which indicated thermal similarity between the two configurations. This similarity was verified by comparing results from the

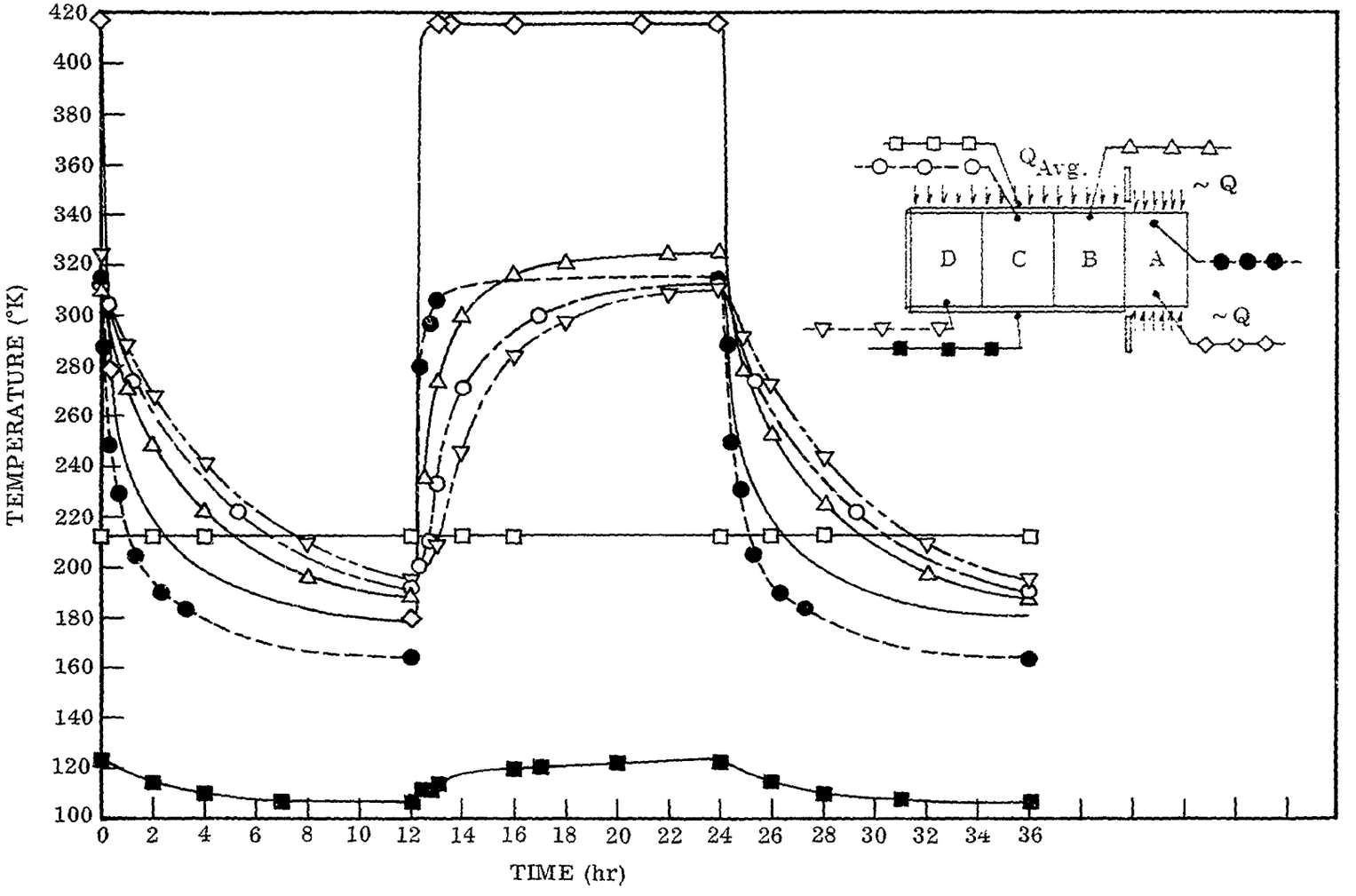


Fig. 41 Configuration 1 Transient Temperatures: Section A Cycled and Top Exterior of Sections B, C, and D Subjected to Average Heat Flux

LOCKHEED PALO ALTO RESEARCH LABORATORY
LOCKHEED MISSILES & SPACE COMPANY
A GROUP DIVISION OF LOCKHEED AIRCRAFT CORPORATION

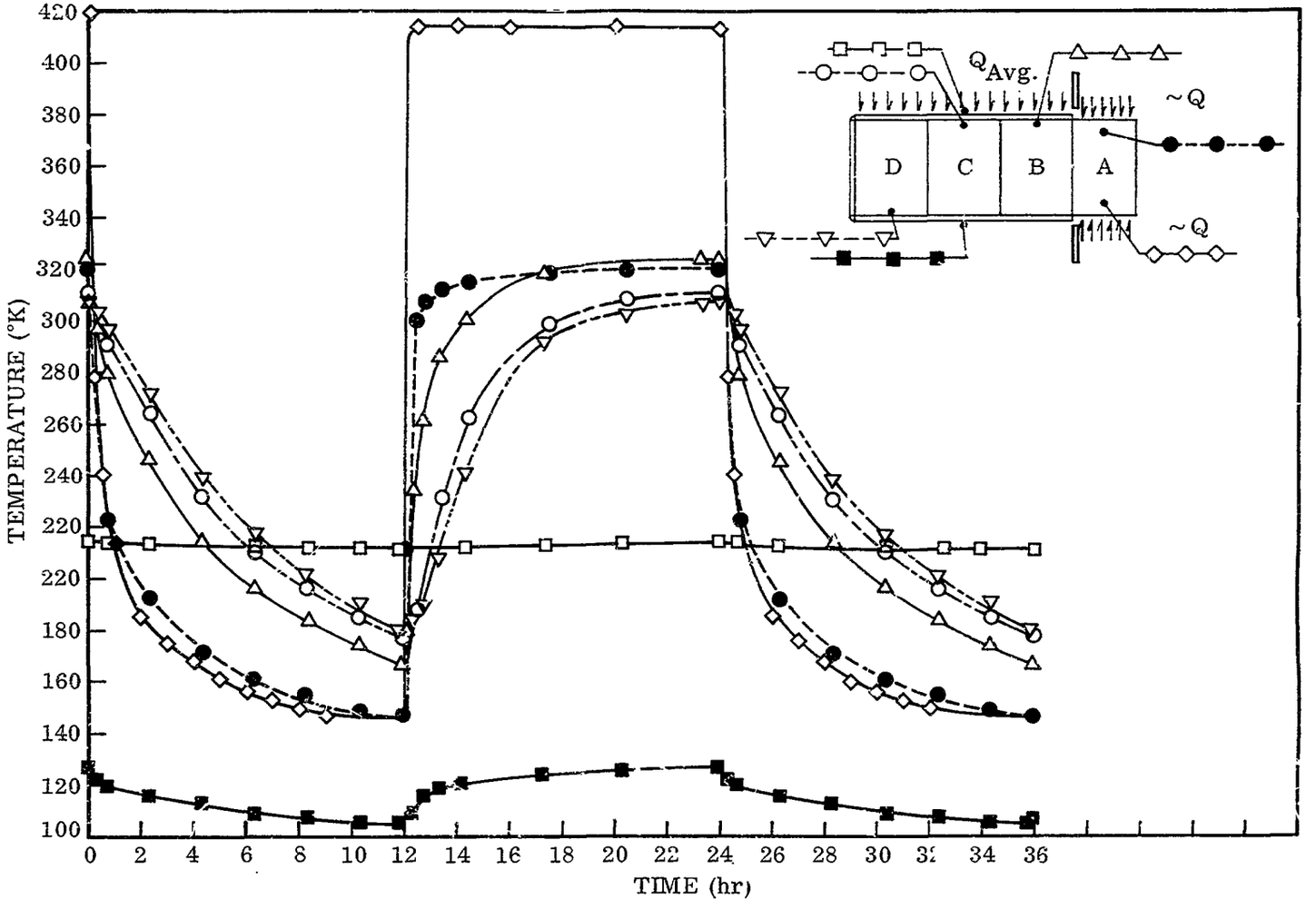


Fig. 42 Configuration 2 Transient Temperatures; Section A Cycled and Top Exterior of Sections B, C, and D Subjected to Average Heat Flux

LOCKHEED PALO ALTO RESEARCH LABORATORY
LOCKHEED MISSILES & SPACE COMPANY
A GROUP DIVISION OF LOCKHEED AIRCRAFT CORPORATION

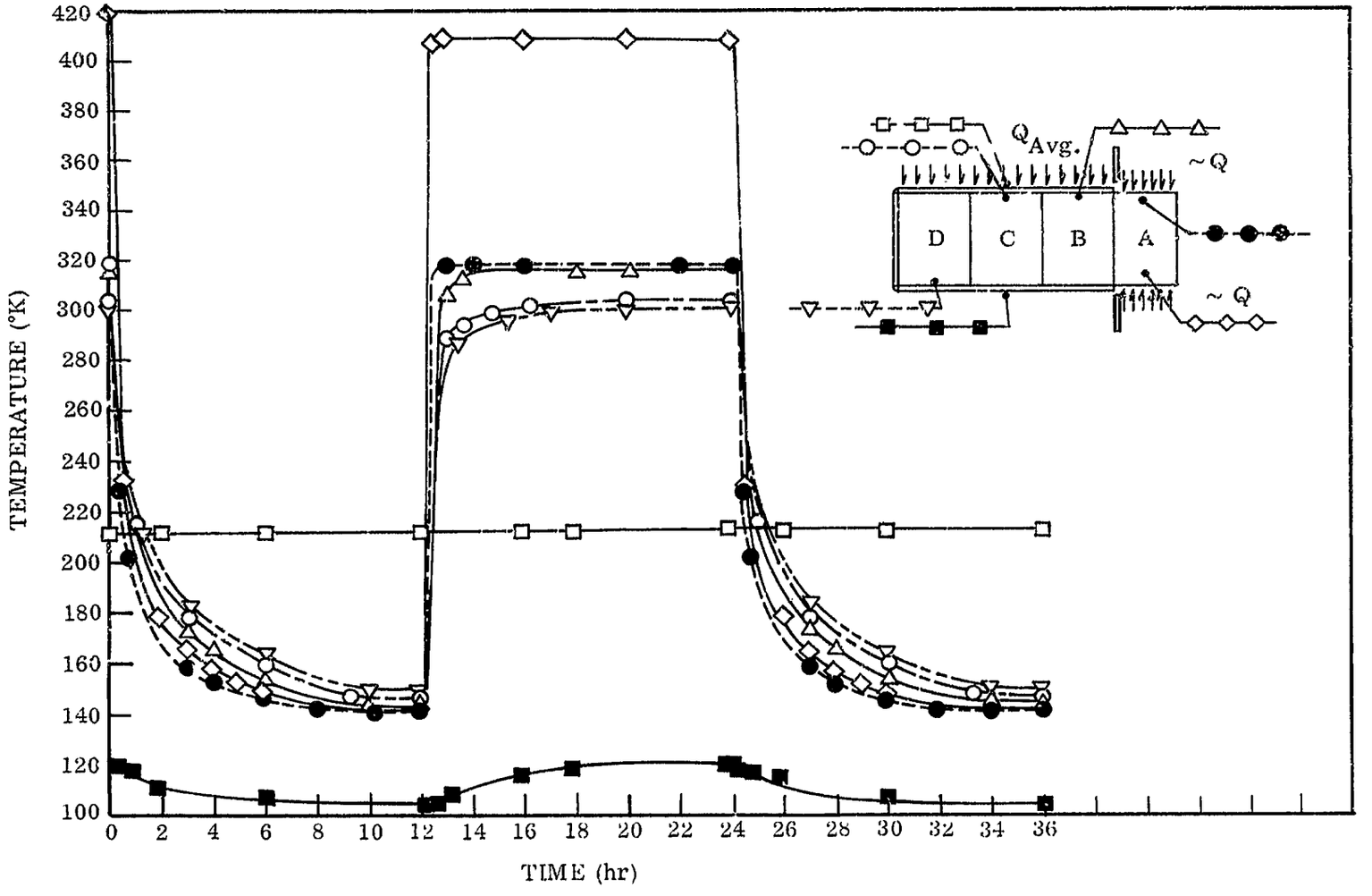


Fig. 43 Configuration 3 Transient Temperatures: Section A Cycled and Top Exterior of Sections B. C. and D Subjected to Average Heat Flux

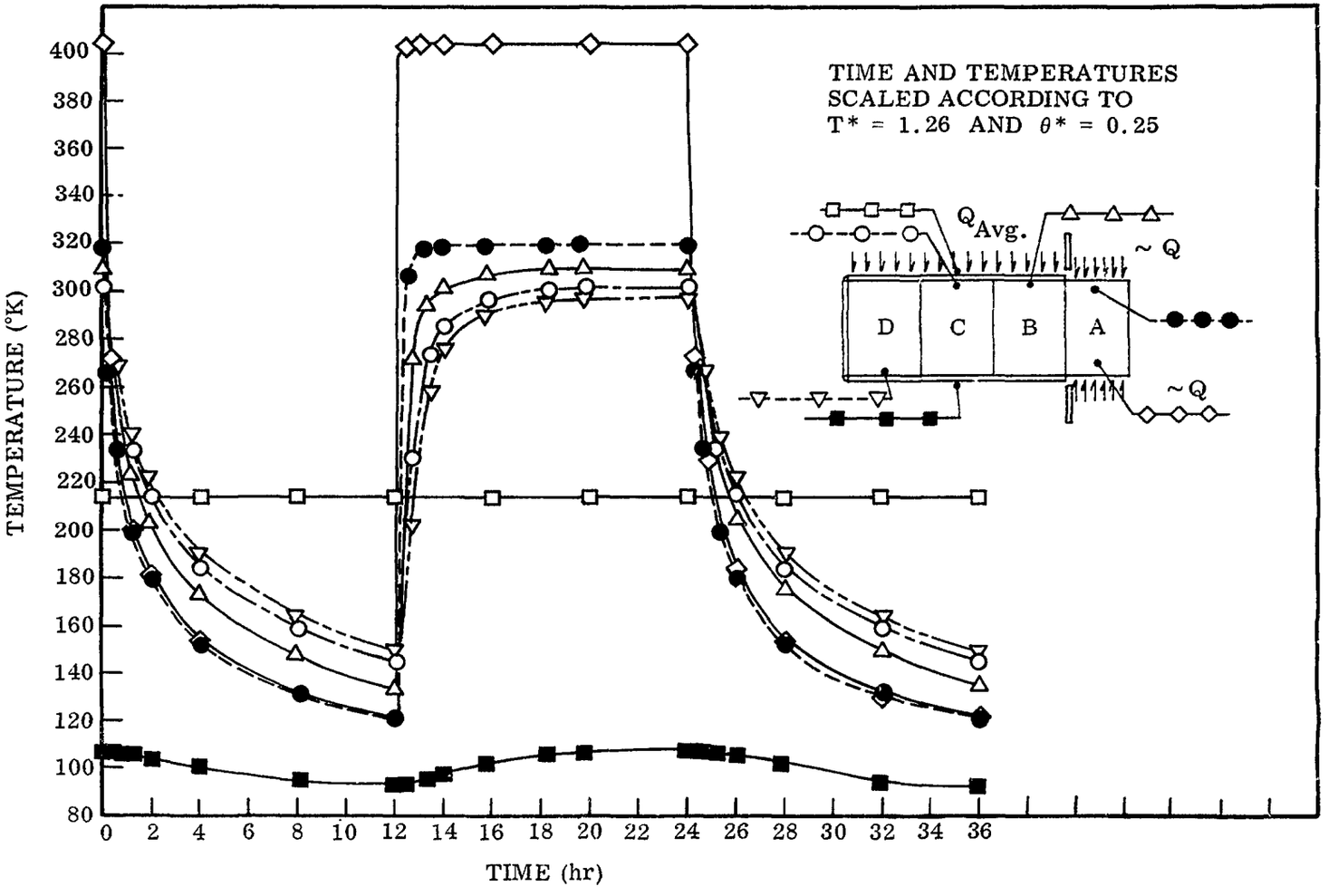


Fig. 44 Configuration 4 Transient Temperatures; Section A Cycled and Top Exterior of Sections B, C, and D Subjected to Average Heat Flux

transient tests involving cycling of the top exterior of Sections B, C, and D while maintaining Section A at constant temperature. These results are presented in Figs. 45 and 46, which show almost identical behavior between the two configurations.

In comparing thermal behavior of the external insulation wrap of configuration 2 (Fig. 42) with that of the internal wrap of configuration 3 (Fig. 43), a large difference in transient response of the internal surface temperatures can be seen. The internal surface temperatures of configuration 3 responded much more rapidly to cycling of Section A than did the internal temperatures of configuration 2. The difference in thermal behavior was due to a change in mass specific heat (mC_p) of the internal surface from one configuration to the other. For configuration 2, the mass specific heat was primarily that of the internal stainless steel skin, whereas for configuration 3, the mass specific heat influencing the immediate transient response was that of the first few layers of the multilayer insulation blanket plus a contribution by the black silicone paint. The rapid response of configuration 3 internal surfaces to changes in Section A temperatures was due to the low mC_p of the internal surfaces. Therefore, the results show that for this type of system an external wrap cannot be substituted for an internal wrap when transient performance is an important consideration. It was observed, however, that the internal wrap had insulating qualities through the blanket equal to those of the external wrap. This is illustrated in the transient results by noting the similarity in external surface temperature behavior for the two configurations as shown in Figs. 42 and 43 and by comparing internal surface thermal behavior of the two systems as presented in Figs. 46 and 47.

Figure 44 presents the transient thermal behavior of the half-scale insulation model (i.e., configuration 4). Both temperature and time scales have been scaled according to the modeling criteria in order to compare performance of the half-scale model directly to that of the full-scale insulation model. For these tests the ratio of time from the full- to half-scale model was $\theta^* = 1/4$ and the corresponding temperature ratio was $T^* = 1.26$. A comparison of Figs. 43 and 44 shows that the overall behavior of the full-scale system was portrayed quite reasonably by the model. In particular, at the end of each half-cycle, the interior temperatures, which were of

primary interest in this investigation, were accurately forecast. A close comparison of the transient cooling cycles in the two figures, however, shows that the cooling rate of the prototype as predicted by the model (Fig. 44) was not as rapid as that measured on the prototype (Fig. 43). An analysis of the data showed that this could be accounted for, in part, by the distortion in the insulation's thickness which was required in order to model the one-dimensional thermal conductivity as discussed in subsection 4.3. However, the difference in cooling rates was more than could be attributed to this one item alone. A following inspection of the model revealed that an error had been made in fabrication of Section A. While the section should have been one-half the thickness of the prototype, it was actually constructed having the same thickness as the prototype. This was somehow overlooked during assembly and checkout of the system. The additional mass of Section A resulted in failure of this section to have the proper time constant and, along with the additional mass of the extra thickness of insulation, caused slow cooling of the model. The influence of the additional mass of Section A on distortion of the time scale was approximately twice that which was attributed to the additional mass of insulation. While heating rates were also affected, the effects were not as pronounced since during heating the primary influence was due to the extra mass of insulation. The extra mass of Section A had very little influence during the heating portion of the cycle since the driving force for the heating cycle was furnished by an automatic control system powering tungsten lamps surrounding Section A rather than radiation to the chamber walls. This becomes apparent when a close comparison is made between the heating curves of Figs. 43 and 44. The transient behavior of Section A is essentially the same in both cases, whereas the heating rates for the half-scale model's interior surfaces are slower than for those of the prototype.

In spite of the error in fabrication of Section A, the results verified that the tube itself had been modeled as planned. Average temperatures and temperatures at the end of heating and cooling cycles were accurately portrayed for the interior surfaces.

Temperatures for the exterior surfaces were found to be lower than predicted from the model laws. The difficulties at the low temperatures for the exterior surfaces of

Sections B, C, and D and for Section A were due to test chamber conditions. Complete conformance with the model criteria requires that all temperatures, including those of the surrounds, be controlled to a single temperature ratio T^*. For this experiment, the ratio was $T^* = 1.26$. Therefore, the chamber wall should have been increased in temperature from 85 to 107°K for the half-scale model tests. This could not be accomplished with the liquid nitrogen cold wall system and resulted in a surrounds temperature for the half-scale test that was 22°K too low. The magnitude of the influence of this chamber condition is, of course, dependent upon the test object temperature and is most apparent at the lower model temperatures.

Figures 45 through 48 present the transient thermal histories of the four configurations when the top exterior surfaces of Sections B, C, and D are being temperature cycled and Section A is being maintained at a constant average temperature. Comparison of configuration 1 and 2 temperatures shows essentially no difference. Comparison of configuration 2 and 3 temperatures shows a slight difference in behavior but not enough difference to indicate significant changes in thermal performance between internal and external insulation wraps. Since the interior temperatures are primarily influenced by energy from Section A, large differences in transient behavior between the internal and external wraps do not show up in this test where the exterior is being temperature cycled. The figures show that fluctuations in exterior surface temperatures have only a minor influence on interior surface temperatures.

The transient behavior of the half-scale model for this test condition, for presentation purposes scaled in terms of prototype temperature and time according to $T^* = 1.26$ and $\theta^* = 1/4$, is given in Fig. 48. Comparing these data with those given in Fig. 47 verifies that the multilayer insulation thermal insulating properties were satisfactorily modeled. For this test condition, the error made in fabrication of Section A had no influence on the results since that section is held at a fixed average temperature. Similar to that which occurred for the previous test condition, temperatures of the exterior surfaces did not model correctly for the colder regions. The model predicted colder temperatures for the prototypes than were measured on the prototype due to the influence of the chamber wall temperatures which were not scaled according to the modeling criteria.

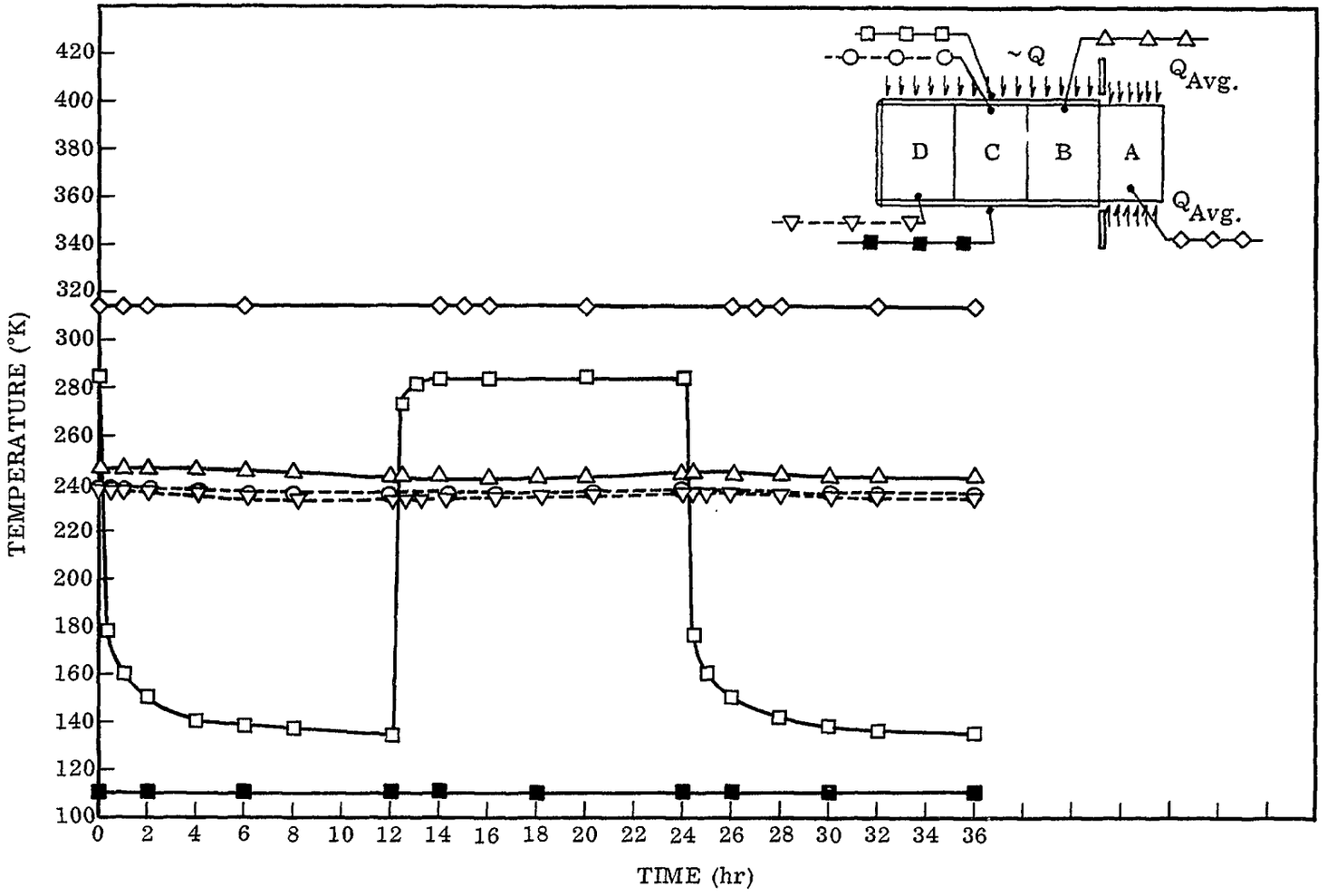


Fig. 45 Configuration 1 Transient Temperatures; Top Exterior of Sections B, C, and D Cycled and Section A Held at Fixed Average Temperature

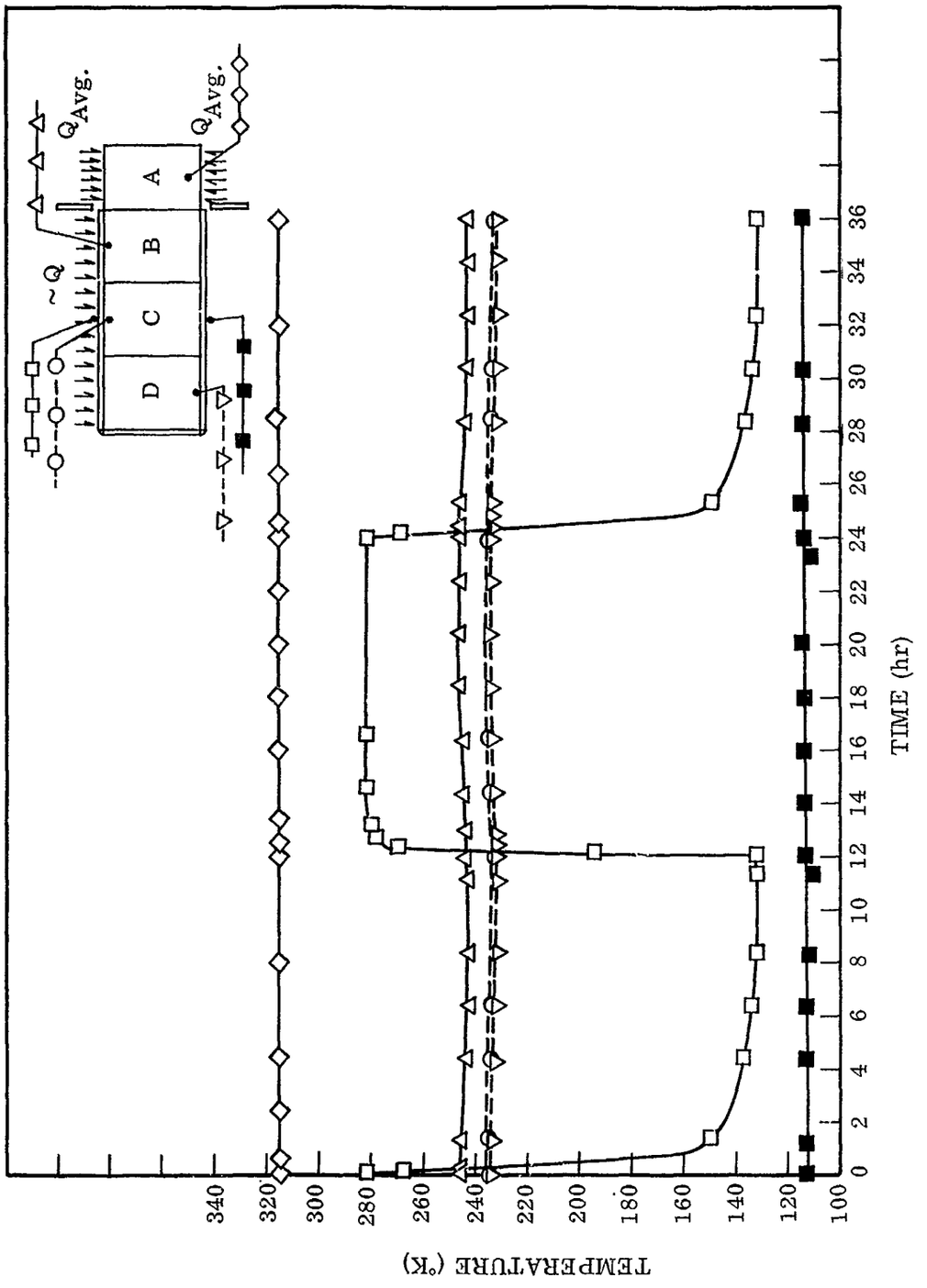


Fig. 46 Configuration 2 Transient Temperatures; Top Exterior of Sections B, C, and D Cycled and Section A Held at Fixed Average Temperature

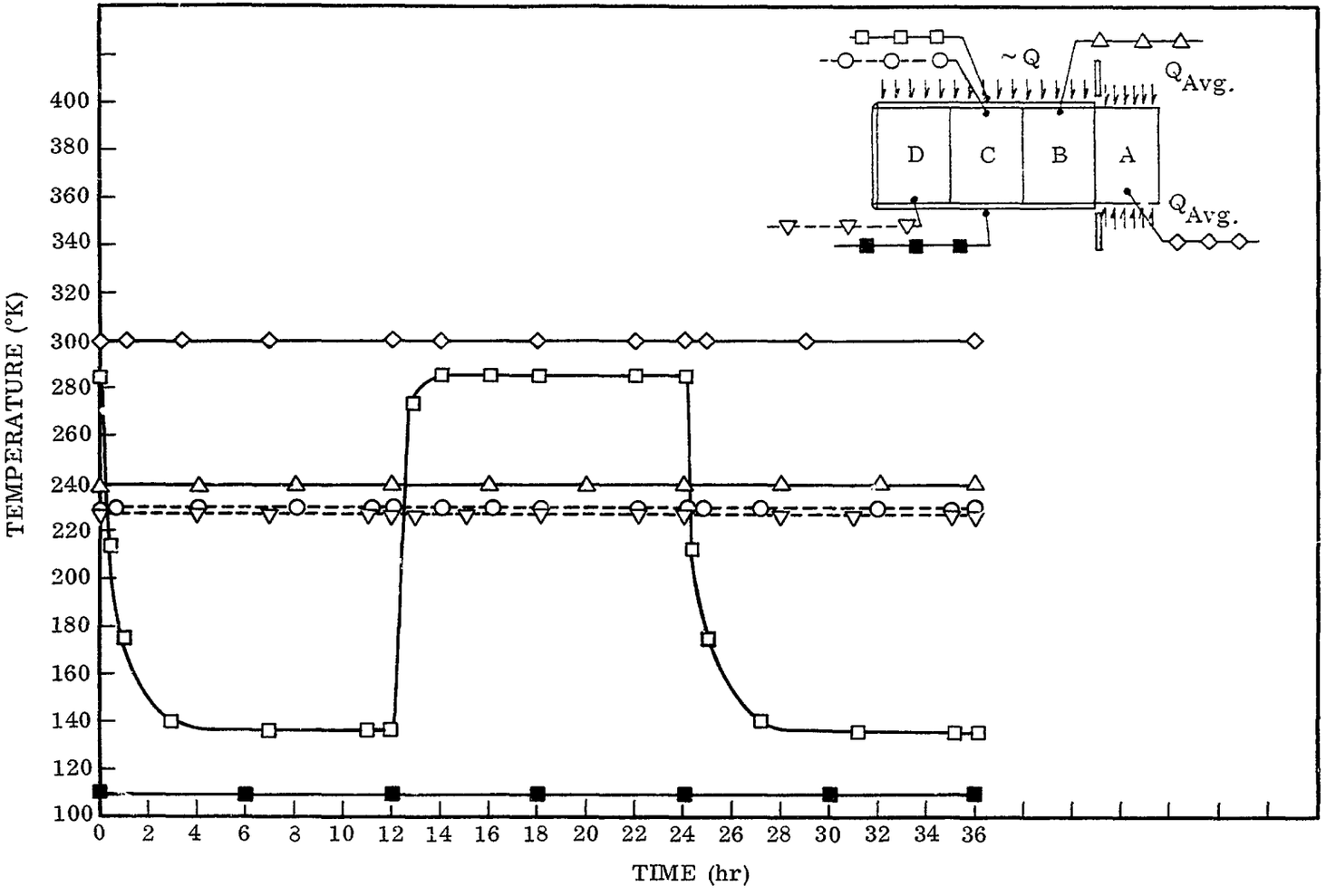


Fig. 47 Configuration 3 Transient Temperatures; Top Exterior of Sections B, C, and D Cycled and Section A Held at Fixed Average Temperature

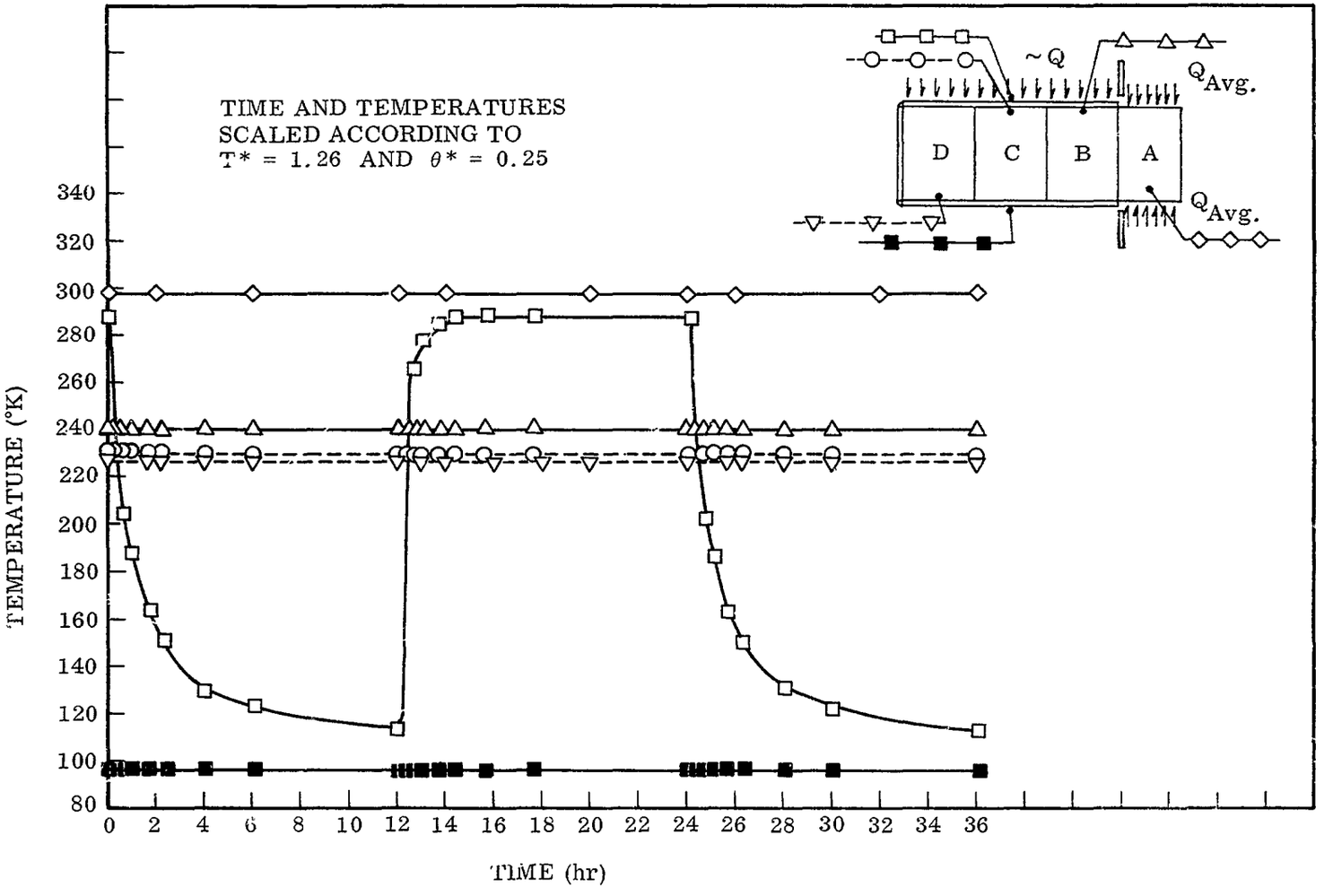


Fig. 48 Configuration 4 Transient Temperatures: Top Exterior of Sections B. C. and D Cycled and Section A Held at Fixed Average Temperature

A numerical comparison of the results for test configurations 3 and 4 is presented in Tables 10 and 11 where temperatures measured at the end of heating and cooling cycles have been tabulated. These temperatures were obtained just prior to initiation of the following heat or cool cycle and provide a measure of the absolute accuracy of model predictio ı. Inspection of the tables show that interior surfaces of the tube were modeled with a maximum difference of $\Delta T = -9°K$ and an average difference on the order of -4°K. Better accuracy was achieved for the interior of Sections C and D than for the interior of Section B at the end of the cooling cycle. Section B was thermally coupled much closer to Section A than were Sections C and D, and thus, this section for the model ran colder at the end of the cool cycle because of the influence of Section A. Heating cycle temperatures were very favorably predicted. Exterior surfaces are shown to have a maximum error of -22°K for the lowest exterior temperature due to the influence of the liquid nitrogen cooled chamber walls.

The figures presented in this section give data for only a few of the 42 temperatures monitored during each test. It should be noted that for all configurations the interior surfaces of Sections C and D were essentially isothermal around the circumference. The interior surface of Section B was nearly isothermal around the circumferences, with the maximum difference in temperature from top to bottom being approximately 5°K. This shows that the large temperature gradients existing on Section A during the first series of tests had very little effect in causing gradients on the blackened interior surfaces of the insulated sections.

4.7 CONCLUSIONS

Results from the multilayer insulation experiments have shown that steady state heat flow perpendicular to the insulation layers can be modeled effectively using a materials preservation approach. This was demonstrated by results from one-dimensional tests which showed that excellent correlation of temperatures was obtained between a prototype and half-scale model. The modeling criteria used for the insulation was $K^*/t^* = 1/L^*$ which introduced a distortion in the transient response of the model due to a necessary distortion in the insulation thickness ratio, t^*. This, however,

Table 10

MODELING RESULTS FOR SECTION A CYCLED AND TOP EXTERIOR AT CONSTANT HEAT FLUX
(T* = 1.26; Temperature – °K)

Location	Tp Full-Scale	Tm Half-Scale	Tm/T* Predicted	ΔT
End of Cooling Cycle				
Interior B	144	170	135	-9
Interior C	146	180	143	-3
Interior D	149	184	146	-3
Exterior C	210	269	213	3
Exterior C	105	117	93	-12
Top Section A	140	152	121	-19
Bottom Section A	142	155	123	-19
End of Heating Cycle				
Interior B	317	398	316	-1
Interior C	304	381	302	-2
Interior D	302	375	298	-4
Exterior C	213	270	215	2
Exterior C	121	136	108	-13
Top Section A	318	403	319	1
Bottom Section A	409	508	404	-5

Table 11

MODELING RESULTS FOR TOP EXTERIOR CYCLED AND SECTION A AT CONSTANT HEAD FLUX
(T* = 1.26, Temperature – °K)

Location	Tp Full-Scale	Tm Half-Scale	Tm/T* Predicted	ΔT
End of Cooling Cycle				
Interior B	239	304	241	2
Interior C	229	289	229	0
Interior D	227	285	226	-1
Exterior C	137	145	115	-22
Exterior C	110	121	96	-14
Top Section A	235	294	233	-2
Bottom Section A	300	376	298	-2
End of Heating Cycle				
Interior B	240	304	241	1
Interior C	231	291	231	0
Interior D	229	287	228	-1
Exterior C	285	363	288	3
Exterior C	111	123	97	-14
Top Section A	237	297	234	-3
Bottom Section A	300	376	298	-2

did not cause serious errors in the half-scale model's transient performance since, for the cyclic transients of interest to this program, the exterior thermal inputs resulted in very minor interior skin temperature fluctuations.

The results from the transient performance tests also showed that the heat flow perpendicular to the layers had been properly modeled. Temperatures at the ends of the transient heating and cooling cycles, as well as the average temperature of the system, were modeled with reasonable accuracy between prototype and half-scale model.

Transient testing was done primarily to study the prototype telescope's transient thermal behavior and to study the effects of thermal modeling on OTES thermal performance. In addition, these tests were run to investigate the influence of varying wrap configurations on the system's performance. The tests showed that the primary driving force which established temperature levels and influenced transient behavior of the interior surfaces of the insulated sections was that of radiant energy emitted from Section A. Heat input to the exterior of the insulated sections had very little influence on interior surface temperature response. The tests showed that distortion of the insulation's thickness scale ratio (t^*) and accompanying distortion of the system's total mass specific heat ratio ($\rho^* V^* C_p^*$) between insulation prototype and half-scale model caused the transient response of the model to be different than that of the prototype. However, exact modeling of the insulation's transient behavior was of minor importance to the performance of the complete telescope model since the temperature levels of critical optical components are established by the average temperatures for each cycle.

The investigation of various wrap configurations showed that the presence of gaps in the insulation blanket between cylindrical segments of the system had negligible effect on the overall thermal performance. Thus, the complete OTES thermal model could have been constructed using either a continuous or segmented insulation wrap even though a segmented wrap is planned for use on the OTES prototype telescope. The tests showed that a substantial difference in transient response can be expected when using an external instead of an internal insulation wrap on systems which have skin

structures with large mass specific heats. It was found, however, that the one-dimensional thermal conductivity was essentially the same for both the internal and external wraps.

The results obtained from testing the half-scale model confirmed that the techniques developed for selecting the insulation wrap configurations for smaller models were valid. Using these techniques the insulation wrap configuration for the 1/6.43-scale thermal model of the OTES prototype telescope was selected. Performance of the modeled insulation proved satisfactory as shown by results presented in the following sections which discuss the performance of the complete telescope thermal model.

Section 5
TELESCOPE MODEL

5.1 MODELING CRITERIA

Design of the telescope model required the use of both thermal and structural modeling criteria to establish length, temperature, time, and stress ratios. The derivation of criteria for thermal modeling in the radiation-conduction coupled space thermal environment has been presented by numerous authors (see, for example, Refs. 1, 4, 5) using slightly different approaches. In view of the ready availability of these presentations, the derivations will not be repeated herein. A somewhat general derivation of the thermal model criteria results in the following statement:

$$\frac{\rho^*V^*C^*T^*}{\theta^*} = A_I^*I^* = Q^* = \frac{K^*A_n^*T^*}{L^*} = A_i^*T^{*4} \qquad (5.1)$$

where the starred quantities are ratios of properties between the model and prototype at each geometrically similar point. Thus, $T^* = T_m/T_p$ for similar points on the model and prototype. The symbols used are defined as

$\rho^* = \rho_m/\rho_p$ = density ratio

$C^* = C_m/C_p$ = specific heat ratio

$V^* = V_m/V_p$ = volume ratio

$\theta^* = \theta_m/\theta_p$ = time ratio

$K^* = K_m/K_p$ = conductivity ratio

$L^* = L_m/L_p$ = length ratio

$A_I^* = A_{I_m}/A_{I_p}$ = area ratio of areas receiving radiation from external sources

$A_n^* = A_{n_m}/A_{n_p}$ = area ratio for areas perpendicular to conductivity path

$A_i^* = A_{i_m}/A_{i_p}$ = area ratio for areas interchanging radiant energy

$T^* = T_m/T_p$ = absolute temperature ratio

$Q^* = Q_m/Q_p$ = ratio of rate of energy dissipation within the model and prototype

$I^* = I_m/$ = intensity ratio of external sources of radiant energy

Equation (5.1) can be rearranged to provide any desired form as long as the indicated identities remain satisfied.

To establish the simple form presented in Eq. (5.1) required the assumption that certain requirements of thermal design will be met. These are:

(1) Complex radiation shape factors must be identical for the model and prototype. This requires that comparable surfaces have the same thermal radiation properties.

(2) The property ratios, i.e., C*, K*, ρ*, A*, etc., are single valued under all operating conditions for all geometrically similar locations.

(3) Geometric identity is required if point-by-point similarity is to be achieved.

When these assumptions are met, and the model designed so that the identities in Eq. (5.1) are satisfied for all elements of the model, then the model will theoretically provide a precise indication of prototype transient and steady state thermal behavior. For cases where transients are not involved, the term containing the specific heat need not be considered and may be dropped from the equation.

The criteria that must be satisfied for proper modeling of the structural behavior of a telescope system whose performance is closely tied to thermal stresses have not received as much attention in recent literature as those for thermal modeling. Therefore, a review of the basic considerations leading to establishment of the model criteria is offered as part of this report.

Two general approaches are available to formulate model laws for structural behavior. One is to derive them from an analytical solution of the structure. The other is to consider the governing equations from which the solution is derived. Using the second and more basic approach leads directly to the ratios required for use in this program.

The three-dimensional expression of Hooke's law is

$$
\begin{aligned}
e_x &= \frac{1}{E}(\sigma_x - \mu\sigma_y - \mu\sigma_z) + \alpha(\Delta T) \\
e_y &= \frac{1}{E}(\sigma_y - \mu\sigma_x - \mu\sigma_z) + \alpha(\Delta T) \\
e_z &= \frac{1}{E}(\sigma_z - \mu\sigma_x - \mu\sigma_y) + \alpha(\Delta T)
\end{aligned}
\tag{5.2}
$$

The shear stress is related to σ by

$$
\begin{aligned}
\frac{\partial \tau_{xy}}{\partial_y} &= -\frac{\partial \sigma_x}{\partial_x} - \frac{\partial \tau_{zx}}{\partial_z} \\
\frac{\partial \tau_{xy}}{\partial_x} &= -\frac{\partial \sigma_y}{\partial_y} - \frac{\partial \tau_{yz}}{\partial_z} \\
\gamma_{xy} &= \frac{\partial(1+\mu)}{E}\,\tau_{xy}
\end{aligned}
\tag{5.3}
$$

with similar relations for τ_{xz}, τ_{yz}, and γ_{xz}, γ_{yz}. These equations use the standard nomenclature where e_x, e_y, e_z and σ_x, σ_y, σ_z are strain and stress components in the x, y, and z directions, respectively. E is Young's modulus, α the coefficient of thermal expansion, ΔT a temperature change in the element from some reference base temperature, μ Poisson's ratio, τ_{xy} the shear component in a plane perpendicular to the x axis and in the y direction, and γ_{xy} the shearing strain.

From Eqs. (5.2) and (5.3), the model ratios are

$$e^* = \frac{\sigma_x^*}{E^*} = \frac{\sigma_y^*\mu^*}{E^*} = \frac{\sigma_z^*\mu^*}{E^*} = \alpha^*(\Delta T)$$

$$\frac{\tau_{xy}^*}{y^*} = \frac{\sigma_x^*}{x^*} = \frac{\tau_{zx}^*}{z^*} \qquad (5.4)$$

$$\gamma_{xy}^* = \frac{\tau_{xy}^*}{E^*} = \frac{\tau_{xy}^*\mu^*}{E^*}$$

In these relations, the asterisk again denotes a ratio between the model and prototype ($\tau^* = \tau m/\tau_p$) which must be identically satisfied for each point and is invariant over all test conditions. Since the great majority of complex structural models must be geometrically similar in three dimensions, Eqs. (5.4) reduce to

$$e^* = \frac{\sigma^*}{E^*} = \frac{\sigma^*\mu^*}{E^*} = \alpha^*(\Delta T)^*$$

$$\tau^* = \sigma^* \qquad (5.5)$$

$$\gamma^* = \frac{\tau^*}{E^*} = \frac{\tau^*\mu^*}{E^*}$$

Equations (5.5) clearly show that $\mu^* = 1$ to properly simulate the thermal stress behavior. This requirement is of particular importance where the three-dimensional stress condition must be duplicated in detail. For a problem where only longitudinal stresses are of concern, it is possible to relax this requirement.

Setting $\mu^* = 1$

$$e^* = \frac{\sigma^*}{E^*} = \alpha^*(\Delta T)^*$$

$$\tau^* = \sigma^* = \gamma^* E^* \qquad (5.6)$$

The scaling laws are derived from overall considerations in terms of lengths, forces, body forces, and boundary conditions. For example, the force at a section is proportional to the stress times the area $F \propto \sigma A$. Therefore $F^* = \sigma^* L^{*2}$ where L^* is the model scale factor, $L^* = L_m/L_p$. Forces, moments, linear deformations, and angular deformations are found as follows in Table 12:

Table 12
STRUCTURAL SCALING LAWS

Effect	Scaling Law
Forces: $F \propto \sigma A$	$F^* = \sigma^* L^{*2} = E^* L^{*2} \alpha^* (\Delta T)^*$
Moments: $M \alpha \sigma AL$	$M^* = \sigma^* L^{*3} = E^* L^{*3} \alpha^* (\Delta T)^*$
Linear Distortions:	$y^* = e^* L^* = L^* \alpha^* (\Delta T)^*$
Angular Distortions:	$\theta^* = \ ^*L^* = (\sigma^* L^*/E^*) = L^* \alpha^* (\Delta T)^*$

This listing relates the ratios of Eqs. (5.6) to those macroscopic structural changes which are of primary interest.

5.2 MODEL DESIGN

Design of the model was based upon the geometries and surface coatings specified in Section 3 after completion of initial thermal design. The results of the thermal studies showed that the primary mirror would be nearly uniform in temperature and undergo less than ±1°K peak-to-valley transients. The secondary mirror support rods were expected to have a considerable temperature difference from end to end (~ 25°K) and to experience considerable transients (~±7°K). The multilayer insulation would provide a nearly adiabatic wall with respect to energy entering the tube aperture and would effectively damp out external transients. These three operating conditions were used as primary guidelines during design of the telescope model.

5.2.1 Primary Mirror Design

The prototype primary mirror consisted of a three segment parabolic quartz mirror, approximately 2 meters in diameter, with a 6-meter focal length. The three segments of the primary would be formed from blanks having a nominal diameter of 1.14 meters.

A number of model approaches were considered for construction of the primary mirror within the limits of reasonable operating temperatures, length ratios, time constants, and ease of fabrication. Consideration was given to the use of both plastics and metals for purposes of obtaining a sufficiently high value of α^* (the ratio of thermal expansion coefficients) to permit direct strain measurements. However, the thermal conductivities of these materials exceeded allowable lower and upper limits of k^* that could be used in combination with the necessary scale ratio (less than 1/5 to fit in the test chamber) and maximum temperature ratio (no greater than 2). This can be seen by consideration of the steady state criteria

$$\frac{K^* A_n^* T^*}{L^*} = A_i^* T^{*4}$$

Using identical geometry, which was necessary for proper figuring of the mirror, gives $A_n^* = A_i^*$ and reduces the criteria to

$$K^* = L^* T^{*3}$$

The allowable span of length and temperature ratios fell in the ranges $1/7 < L^* < 1/5$, $1.5 < T^* < 2$. These limits restricted the selection of materials to $0.48 < K^* < 1.5$. Unfortunately, neither metals nor plastics fall within the necessary range which limited the material selection to glass.

A search of available information on the thermophysical properties of glasses was made and followed by numerous primary mirror designs. The best design called for the use of Pyrex in construction of the primary mirror. A comparison of the most

probable properties of fused quartz (Corning 7940) at 175°K and Pyrex at room temperature is presented in Table 13.

Table 13

PROPERTIES OF PYREX AND FUSED QUARTZ

Property	Quartz (175°K)	Pyrex (293°K)
Thermal Conductivity (W/°K M)	1.12×10^{-2}	1.13×10^{-2}
Specific Heat (J/g °K)	0.464	0.690
Density (gm/cm^3)	2.3	2.45
Thermal Expansion Coefficient (cm/cm-°K)	$\approx 2 \times 10^{-7}$	3.77×10^{-6}
K*		1.008
C_p^*		1.5
ρ^*		1.06

Selection of the length ratio was based upon considerations of chamber size in relation to prototype size, which, as previously stated, had to be in the range $1/7 \leq L^* \leq 1/5$, and upon the practical consideration that considerable reduction in cost could be achieved by purchase of glass blanks as off-the-shelf items. Both criteria were met by selecting a scale ratio $L^* = 1/6.43$. For this length ratio, and the use of pyrex, the ratios preserving the influences of radiation and conduction in Eq. (5.1) yield, for identical geometry

$$T^* = (K^*/L^*)^{1/3} = [(1.008)(6.43)]^{1/3} = 1.86$$

and

$$\theta^* = \rho^* C^* L^{*2}/K^* = (1.06)(1.5)/(6.43)^2(1.008) = 1/26$$

Design of the model primary mirror was in accord with the above ratios and was produced to the dimensions shown in Fig. 49. Three individual mirror segments were purchased, their edges cut to provide the necessary mating surfaces, waxed together,

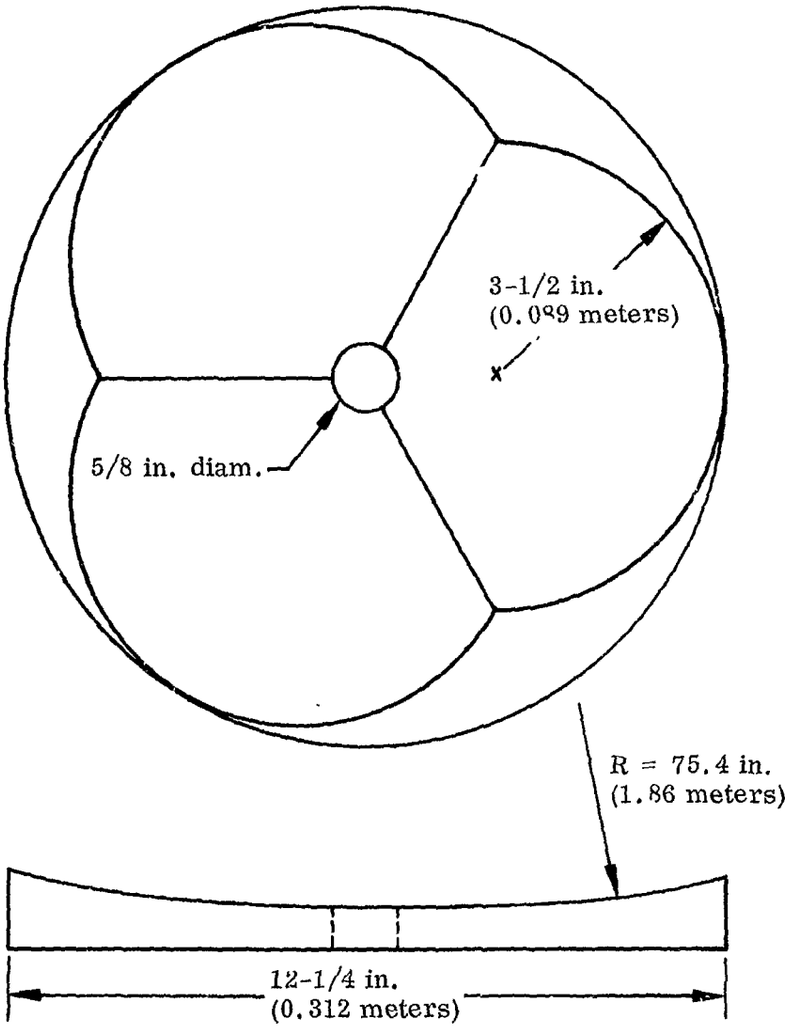


Fig. 49 Model Primary Mirror

their front surface ground to provide a 73.4-in. (1.86 M) radius of curvature. Thus, geometrically similar mirrors of high optical quality were used. Following final surface polishing, the mirrors were released from the wax and aluminized on all surfaces. Each segment had a final weight of 1375 grams.

5.2.2 Secondary Mirror Support Rod Design

Modeling of the secondary support rods had to be in accord with the length ratio, temperature ratio, and time constant selected for the primary optic. It was also desired to use a material with a large coefficient of thermal expansion so that thermal strain could be determined directly. Consideration was given to the use of pyrex solid rod; however, the required length ratio, $L^* = 1/6.43$, and 1-in. diameter of the prototype rod, would necessitate the use of a rod for the model having a diameter of 0.156 in. (0.396 cm). This size was deemed to be impractical for required model strength. Therefore, the design was directed toward the use of tubing necessitating geometrical distortion.

The general thermal model criteria for the support rods are

$$\frac{\rho^* V^* C^*}{\theta^*} = \frac{K^* A_n^*}{L^*} A^* T^{*3}$$

where the terms are as previously defined. For the thermal conditions predicted for the telescope tube, it is apparent that temperature gradients will be experienced along the rod length. However, gradients perpendicular to the rod axis will be extremely small. Therefore, geometric distortion of the rod thickness concurrent with preservation of the model criteria is allowable and a potentially useful procedure for increasing the rod strength.

Defining the cross-sectional area of the tube as A_k, outer surface area as A_o, inner diameter as d_i, outer diameter as d_o, and neglecting gradients through the tube thickness, gives

$$\frac{\rho^* C^* A_k^* L^*}{\theta^*} = \frac{K^* A_k^*}{L^*} = A_o^* T^{*3}$$

or

$$\frac{\rho^* C^* L^*}{\theta^*} = \frac{K^*}{L^*} = \frac{d_{o_m} d_{o_p}}{d_{o_m}^2 - d_{i_m}^2} L^* T^{*3}$$

Since the design requires conformance to the primary mirror ratios $T^* = 1.86$ and $\theta^* = 1/26$, material properties and available sizes were sought which provided these values. Thin wall aluminum, stainless steel, and titanium tubes were considered along with five varieties of laboratory glassware. During this selection process, the thermal effects of required instrumentation leads and black surface coatings were accounted for. The best match to the requirements

$$\theta^* = \rho^* C^* L^{*2} / K^* = 1/26$$

and

$$\frac{d_{o_m} d_{o_p}}{K^* \left(d_{o_m}^2 - d_{i_m}^2 \right)} = 1/L^{*2} T^{*3} = 6.43$$

was obtained with pyrex tubing with $d_o = 12$ mm, $d_i = 10$ mm, and a 2-mil coating of black Thermatrol paint. For this tube, including the surface coating, two lengths of 1-mil diameter constantan wire in the interior, and one length of 3-mil diameter copper wire along the outer surface, $\theta^* = 1/25.9$ and $d_{o_m} d_{o_p} / K^* \left(d_{o_m}^2 - d_{i_m}^2 \right) = 6.70$ at room temperature. These values were the optimum found and were considered satisfactory in terms of the experiment requirements. The tubing selected as appropriate for satisfaction of the thermal modeling requirements obviously fails to meet the structural modeling criteria given in Section 5 since geometric identity is not

provided in the model. The use of 12 mm o.d. tubing results in severe geometric distortion of the prototype except for length dimensions. For this reason the relation between forces, moments, and thermal stresses are not preserved in the model. However, since the support rod system is not constrained at the ends, thermal stresses in the rods will not result in introduction of forces or moments into the support system. Under these conditions, geometric distortion is allowable and rod elongation is related only to the thermal expansion characteristics. Therefore, for the system under consideration

$$y^* = L^*\alpha^*(\Delta T)^* = \alpha^*(1/6.43)(1.86) = \alpha^*/3.46$$

The thermal expansion coefficient of the Pyrex rods used for the model was determined experimentally with a quartz dilatometer over the temperature range 70 to 300°F (294 to 422°K). The results of the measurement are shown in Fig. 50. The experimental results compared favorably with published data and indicated an expansion coefficient $\alpha = 2.08 \times 10^{-6}$ in./in. °F (3.77×10^{-6} cm/cm °K). The expansion coefficient of fused silica at the prototype operating temperatures, as shown in Fig. 2, will be approximately 2×10^{-7} cm/cm °K resulting in $y^* = \alpha^*/3.46 = 5.45$.

5.2.3 Multilayer Insulation

Design of the model insulation was based upon the experience gained from the insulation studies presented in Section 4. The design for the 1/6.43 scale ratio is discussed in that section. It is of particular interest to point out that modeling of the perpendicular conductivity for an increased temperature ratio was found to be entirely possible through distortion of thickness using identical materials. Using this approach to obtain a required perpendicular K* results in distortion of the parallel K* whose value depends primarily on the solid conductivity of the materials

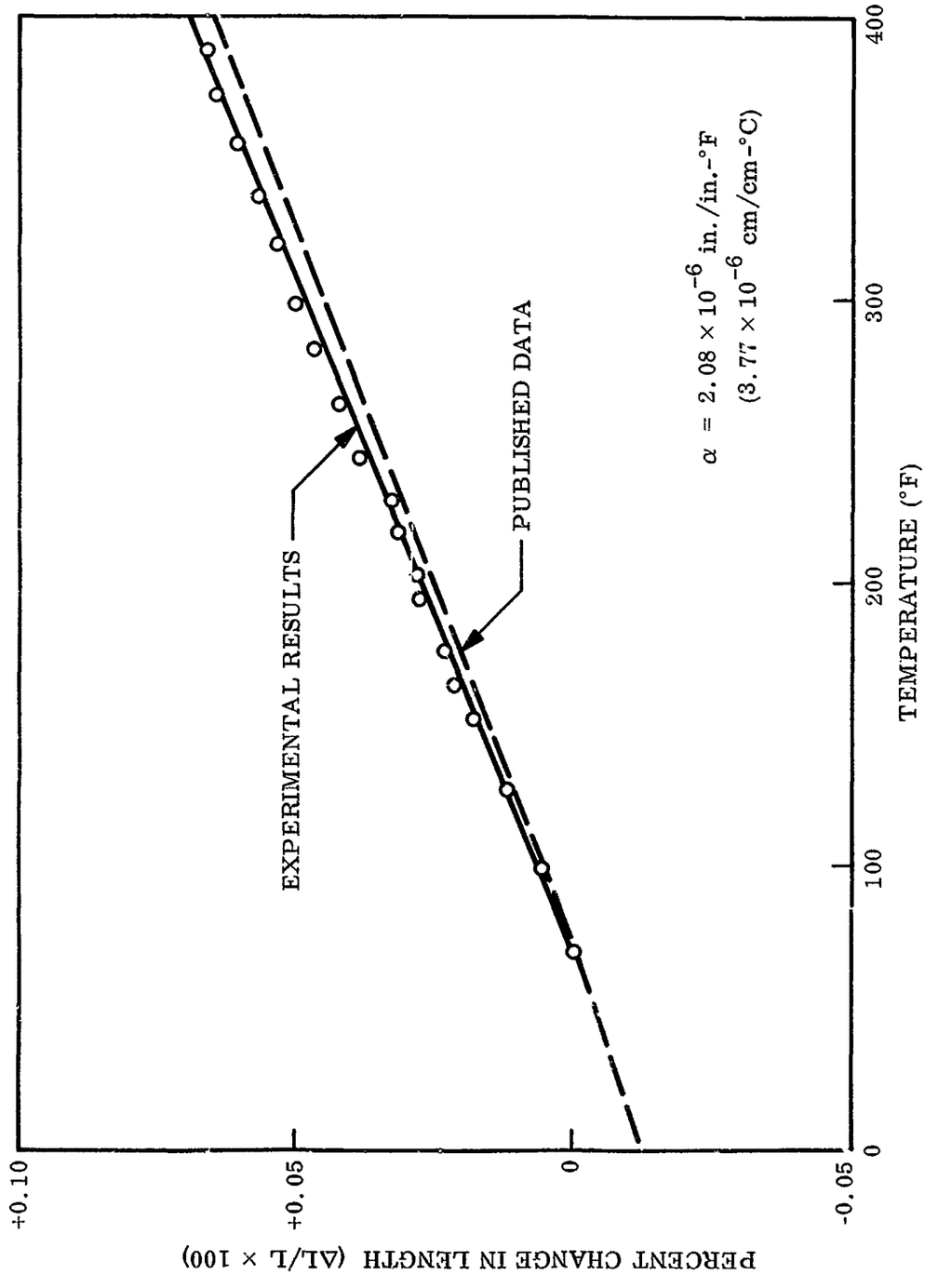


Fig. 50 Thermal Expansion of Pyrex

used. For similar materials using the same wrap density, the parallel conductivity will remain nearly constant giving a parallel K^* near unity.

For the telescope tube, it was of primary importance to model the insulation in such a manner that the average model interior temperature would provide reasonable predictions of prototype conditions. As previously indicated in Section 3, the analytical predictions allowed the conclusion that the average temperatures of the telescope interior would not be dependent on assumed changes in insulation conductivity for approximately one order of magnitude about the assumed value of 4.8×10^{-5} W/°K-meter. This permitted design of the model wrap to be based on the average temperatures predicted for the prototype and avoided the necessity to design for either maximum or minimum values. The test results presented in Section 4 show that for a temperature ratio greater than unity it is not possible to model the insulation so that K^* remains constant over a wide range of temperature. Thus, it is most desirable to model to a mean temperature and accept the variations about the mean. The prototype mean temperature selected for use in design of the model wrap was 122°K corresponding to a model mean temperature of 227°K.

The model wrap was based upon the use of identical materials and the properties determined from the experiments reported in Section 4. The previous choice of $L^* = 1/6.43$ and $T^* = 1.86$ required that the perpendicular conductivity model according to $K^*/t^* = 6.43$, where t^* is the ratio of insulation thickness for identical wrap densities. The closest approach to meeting these requirements was a 13-layer wrap with an expected $k^* = 2.36$ at the selected average temperature. Thus, $t^* = 13/36 = 1/2.78$ and $K^*/t^* = 6.56$ instead of the required 6.43.

The transient criteria for this study require that

$$\frac{\rho^* C^* V^*}{\theta^*} = A^* T^{*3} = L^*$$

It is apparent that the dependence of K^* on t^*, such that a specific thickness must be chosen to meet a specific K_m at a single temperature, allows adjustment of θ^* only through changes in ρ and C on the model. However, since identical materials are used in the model and prototype, the wrap itself cannot be varied to provide the necessary adjustments. In addition, for the insulation it was determined that the temperature dependence of C results in $C^* = 1.88$, thus

$$\theta^* = \rho^* C^* L^* t^* = 1/9.35$$

rather than 1/26 as required. The large value of θ^* for the insulation alone led to the necessity of considering the elimination of an external skin on the model and lumping the heat capacity of skin and insulation together. With this approach, the ratio of total heat capacitance becomes

$$(\rho^* V^* C^*)_{total} = \frac{(\rho_m V_m C_m)_{insul}}{(\rho_p V_p C_p)_{skin} + (\rho_p V_p C_p)_{insul}}$$

For the properties listed in Table 1 and the above model ratios, the computation yields $(\rho^* V^* C^*)_{total} = L^{*2}/3.58$ and $\theta^* = 1/23$. This value is more in line with the required time constant. Therefore, this approach was used for model construction.

Darkening of the tube interior was necessary and required the use of a 2-mil coating of black Thermatrol whose capacitance, when added to the insulation, resulted in an increase of the time ratio for $\theta^* = 1/17.8$.

The final design of the model insulation provided an overall skin system whose performance was expected to adequately simulate that of the telescope tube. While the distribution of heat capacitance was not identical to the prototype, this fact in itself would not alter the transient response. The most serious alteration of the transient behavior would be expected to be due to the differences in temperature dependence of specific heat and thermal conductivity for the model and prototype systems.

5.2.4 Manned Support Structure Interface

Modeling of the manned support structure interface was limited to the honeycomb disk and multilayer insulation between the manned section and telescope interior. The prototype manned section was assumed to be held at a uniform and constant temperature of 297°K (75°F) requiring a model temperature for that section of 562°K (534°F). This exceeds the useful upper temperature limit of aluminized mylar and required the use of a high-temperature insulation in construction of the model. The insulation system selected for use was alternate layers of double aluminized Kapton and Dexiglas. The temperature dependence of thermal conductivity for this system was known from test results obtained during completion of a separately sponsored program.

Utilizing the steady state modeling criteria, results of the thermal analyses, and available test results, led to the selection of an 18-layer wrap to model the conductance assumed for the analytical study.

The 2.54 cm (1 in.) aluminum honeycomb structure used for support of the primary optics was modeled using a disk of 4-mil, 304 stainless steel sheet. This properly preserved thermal gradients parallel to the sheet, though preservation perpendicular to the sheet was not attained. Since gradients in the latter direction were predicted as negligible, this distortion was considered allowable. For 304 stainless steel, the property ratios are $\rho^* = 116$, $C^* - 0.85$, and $k^* = 42.4$. The criteria for modeling where gradients through the skin are neglected is

$$\frac{\rho^* C^* L^{*2} t^*}{\theta^*} = \frac{k^* L^* t^*}{L^*} = L^{*2} T^{*3}$$

for t^* = skin thickness. The last two terms are applicable to proper preservation of the radiative-conductive heat flow and require $t^* = L^*/k^* = 1/272$.

In terms of model dimensions, the required thickness would be $t_m = 0.00368$ in. This result led to specification of 4-mil sheet stock with $k^*t^* = 1/5.9$ instead of $1/6.43$, and $\theta^* = \rho^* C^* t^* L^* = 1/16.3$. This design was considered adequate in

terms of the anticipated performance indicated by the thermal analysis. Those results indicated that the mounting plate would undergo only slight transient variations and further that the variations would not influence mirror performance.

5.2.5 Surface Coatings

Black Thermatrol paint was used as a coating for the interior and exterior surfaces of the tube sections. In accordance with the thermal design, a small band of aluminized mylar adjacent to the primary mirror was not painted. The stainless steel sheet manned interface structure was covered on the telescope side with one layer of aluminized mylar to decrease its emittance. All mirror surfaces were coated with opaque coatings of evaporated aluminum.

5.3 MODEL FABRICATION ASSEMBLY

The insulated telescope sections were first fabricated to the required sheet size and then attached to the inside of cylindrical wire cages having the necessary model diameter. These cages were constructed of 0.159-cm diameter (1/16-in.) stainless steel rod and furnished the necessary structural support. Use of wire for the cages and placement of the insulated sections on the inside minimized the thermal influence of the wire supports. Following fabrication and painting, each section was slipped into its neighbor to give a 1.27-cm (1/2-in.) overlap. The sections were attached to each other with nylon thread at each of the overlapping joints.

A 0.476-cm thick aluminum plate was attached to the chamber door support structure to serve both as a support from which to hang the telescope and to provide a uniform temperature region duplicating the manned support interface. The interface insulation, mirror support plate, primary mirror, secondary mirror support rods, and insulated tube were all supported from the aluminum plate.

The assembled model geometry is shown in Fig. 51. The primary mirror was supported from the mounting plate using nylon screws and a 0.159 cm thick phenolic suspension. The arrangement used is shown in Fig. 52. Lexan plugs were epoxied

PALO ALTO RESEARCH LABORATORY
MISSILES & SPACE COMPANY
DIVISION OF LOCKHEED AIRCRAFT CORPORATION

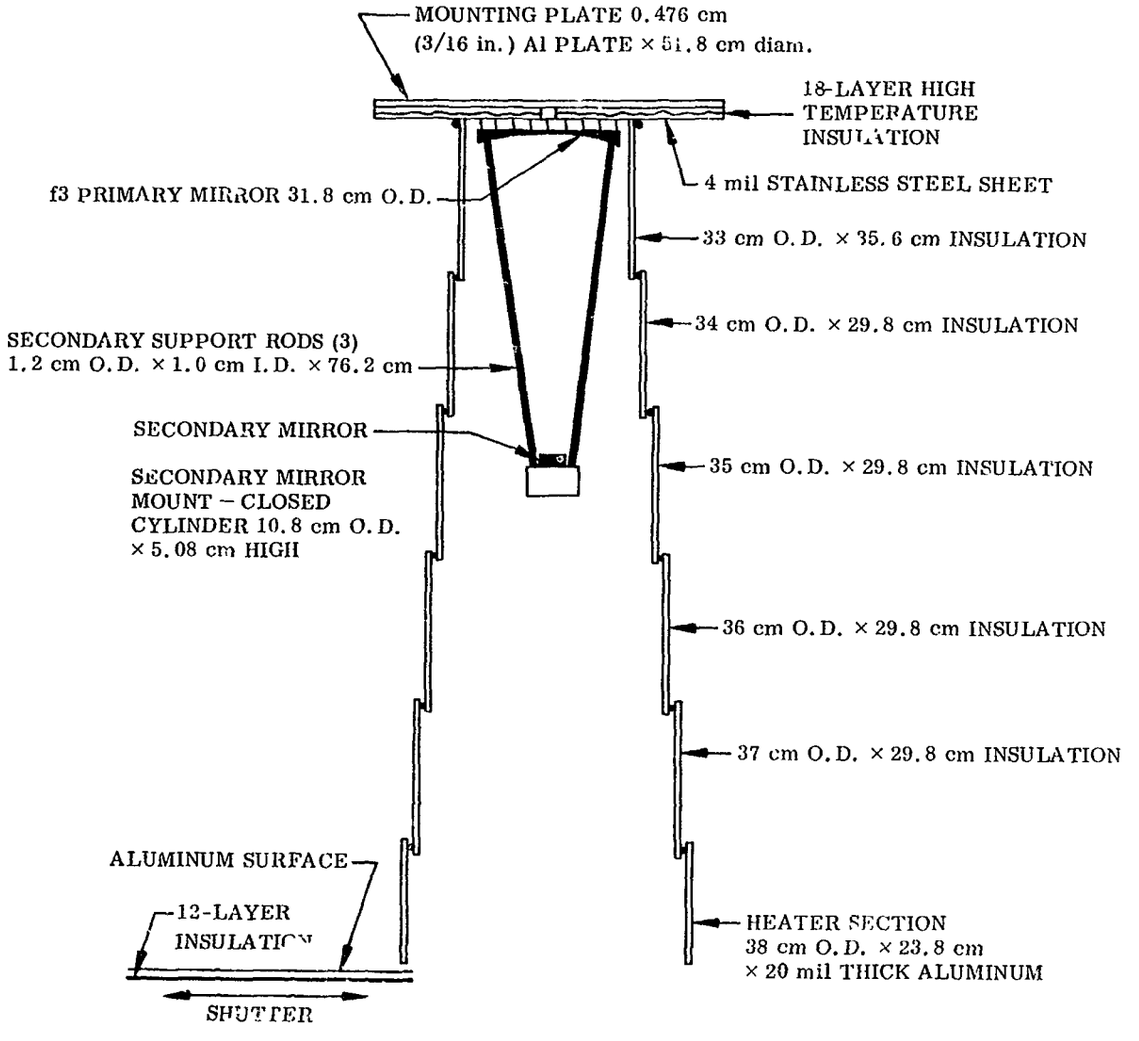


Fig. 51 Model Geometry

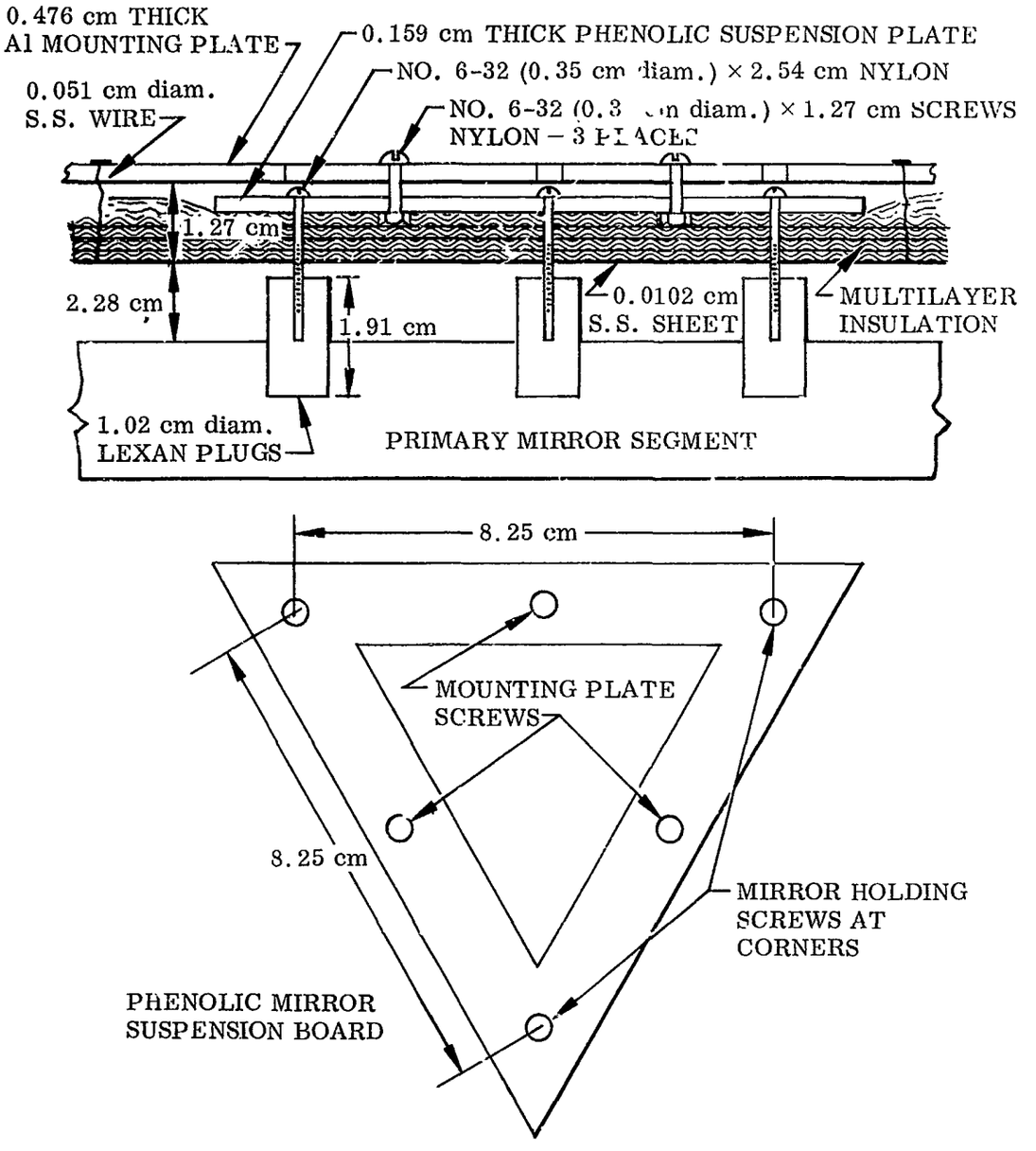


Fig. 52 Primary Mirror Suspension

into holes that were bored in the back of the mirror. These plugs furnished attachment points for suspension of the rather heavy mirror segments. The techniques used to mount the mirrors could not be based upon the prototype geometry since design of that mounting system had not yet been accomplished. However, it was assumed that low conductivity materials would be used on the prototype to achieve the necessary low temperatures; therefore, similar procedures were used on the model. The secondary mirror support rods were epoxied into phenolic mounts that were in turn attached to the stainless steel sheet using nylon screws. The telescope tube was suspended from the top aluminum plate with stainless steel wire. The top assembly of the sections was brought into firm contact with the aluminum surface of the stainless sheet, but was not bonded at that location.

5.3.1 Model Instrumentation

Instrumentation attached to the model included 73 3-mil-diameter copper-constantan thermocouples and three linear distortion gages for measurement of the desired thermal and structural behavior. Locations of the thermocouples on the model are shown on Fig. 53, with additional details of locations on the primary mirror and adjacent surfaces shown on Fig. 54. The numbers shown in the figures correspond to those used to report the experimental results and are not the same as the node numbers established in Section 3. The thermocouple locations shown do not correspond identically with the node locations indicated in Figs. 5 to 13. On the tube, the thermocouples were located exactly on the +x and -x axis, and on the mirror the locations were chosen for purposes of obtaining the best indication of the influence of radiation and conduction heat flow paths. In most cases the thermocouples were located sufficiently close to analytical nodes to permit a direct comparison of results even though identical geometric locations with node centers was not accomplished.

Thermal distortions were measured directly in the three secondary support rods where thermal transients were expected to cause measurable levels of distortion. Strain gaging of the primary mirror was not attempted in view of the predicted constant and uniform temperatures and insensitivity of strain-gaging to the anticipated changes in strain. It was expected that the thermally induced response of the gage itself would exceed its response to changes in mirror dimensions and that useful information would not be obtained. This expectation was borne out by the test data which indicated a nearly constant primary mirror temperature.

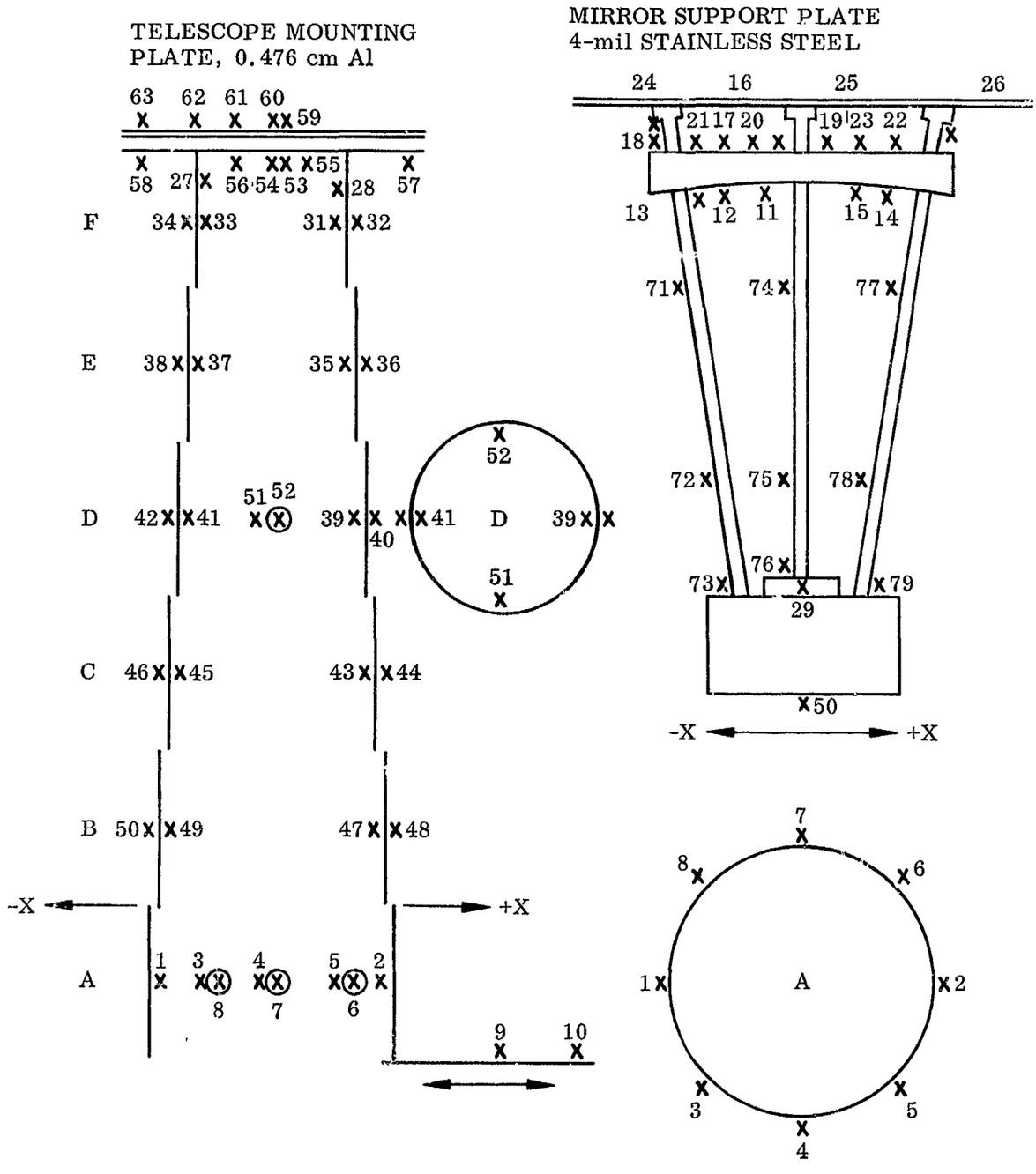


Fig. 53 Model Thermocouple Locations

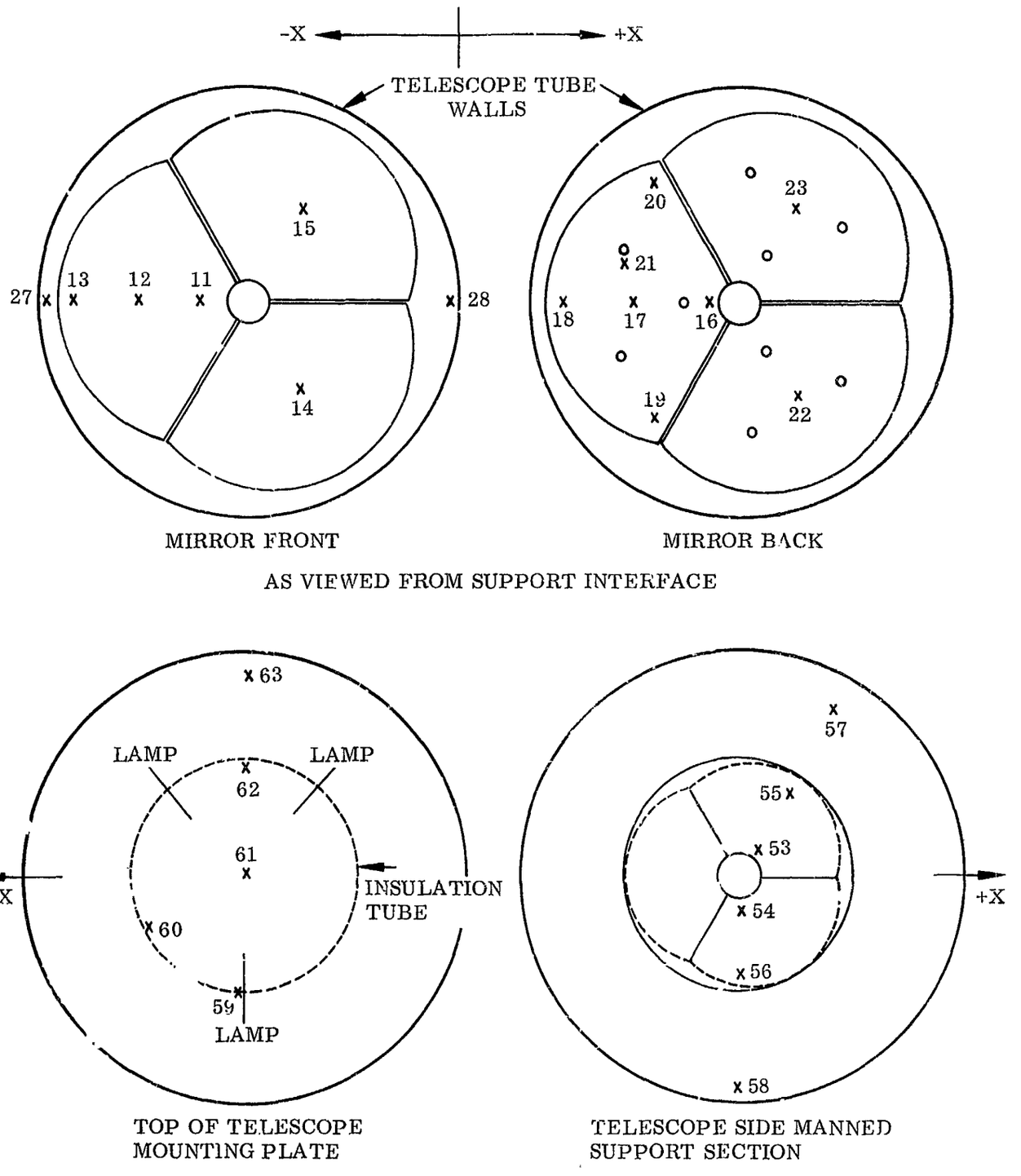


Fig. 54 Primary Mirror Thermocouples

Measurement of distortions of the secondary support rods was accomplished using a single strand of constantan strain wire inside of each pyrex tube that was stretched and bonded to the tube ends. A slack wire of the same spool was placed in the tube next to the prestrained wire to provide temperature compensation. The two wires provided two legs of a Wheatstone bridge whose change in resistance was measured for indications of thermal strain. Each of the support rods was calibrated in a uniform temperature air oven for determination of the bridge response to imposed thermal strain. The experimentally determined thermal expansion data as well as a dilatometer were used to establish elongation values during the calibrations. Calibrations using the dilatometer with imposed highly nonuniform temperature distributions in the rod compared within 5% to calibrations in the air oven with uniform temperatures. These results verified that the effectiveness of the temperature compensating leg of the bridge would be adequate and that the gage response was -36.1×10^{-5} cm/mV. The negative value was expected since the thermal expansion of constantan is larger than that for pyrex.

5.3.2 Chamber Installation

The entire model was suspended from stainless steel framing extending from the top of the vacuum chamber door. The support plate, primary mirrors, and secondary mirror structure were installed first, all instrumentation checked, and the tube slipped over the completed assembly. Figure 55 illustrates the appearance of the optical system following chamber installation.

The movable shutter system was supported by rails at the bottom of the tube and was moved in and out in a horizontal plane by a manually actuated crank and level system. The shutter and its supports are shown at the bottom of Fig. 56. The entire assembled system, as it appeared just prior to testing, is shown in Fig. 57.

Transient skin temperatures were provided by automatically controlled banks of tungsten filament lamps located adjacent to the skin regions. Five banks of lamps were used to achieve separate control of the simulated manned section the +x and -x sides of Sections B through F and the +x and -x sides of Section A. The lamps

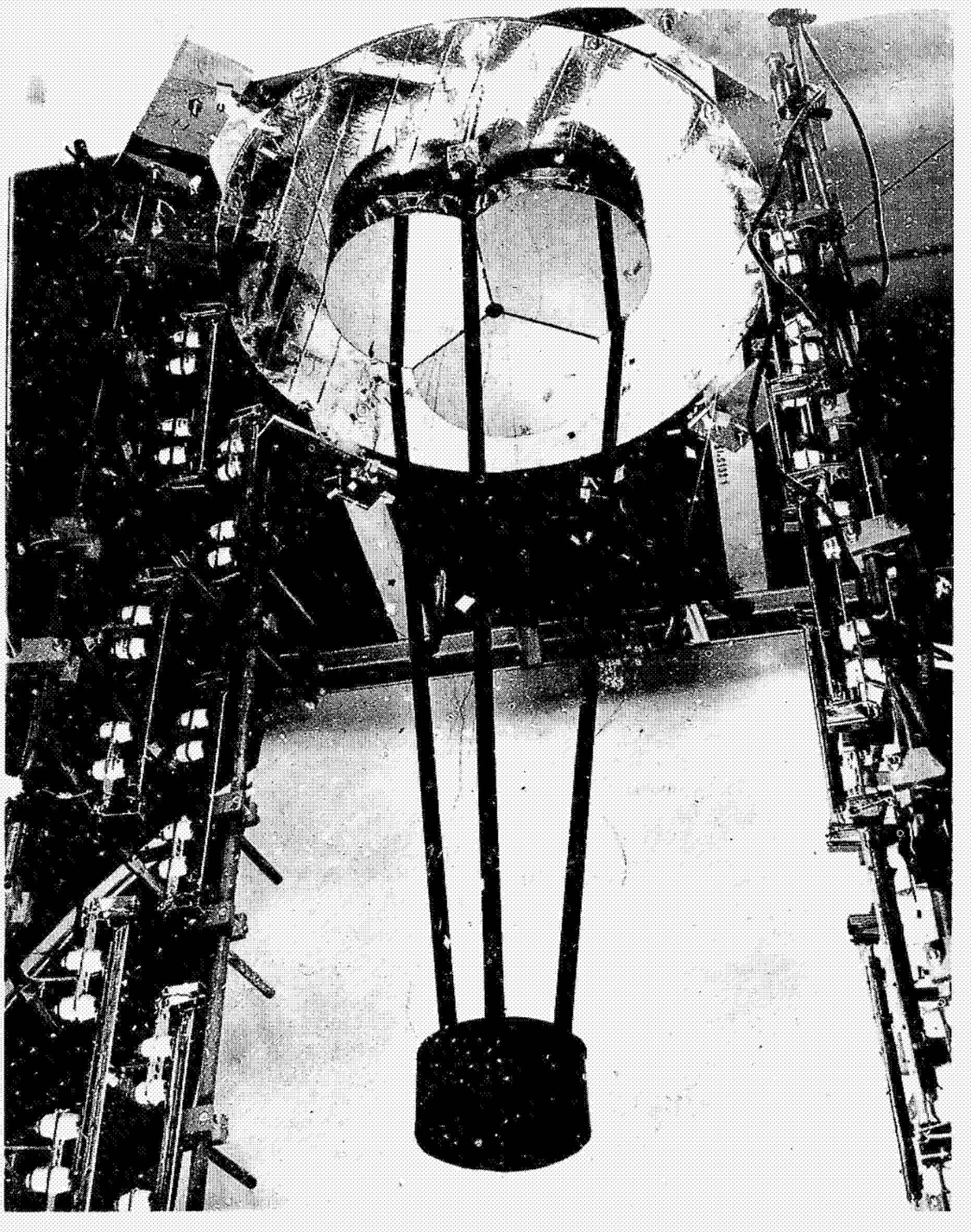


Fig. 55 Assembled Optical System

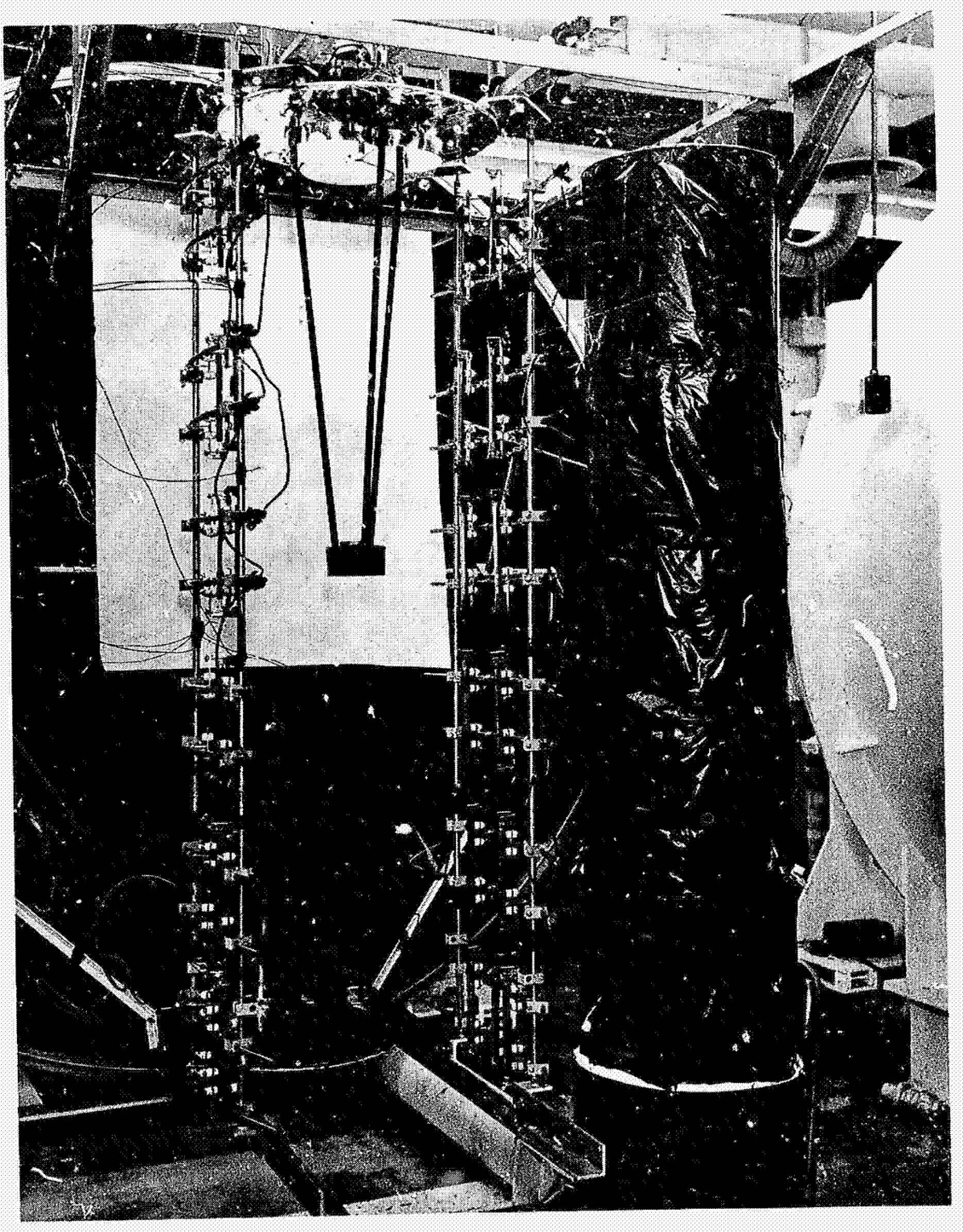


Fig. 56 Optical System, Lamp Bank Arrays, and Movable Shutter System

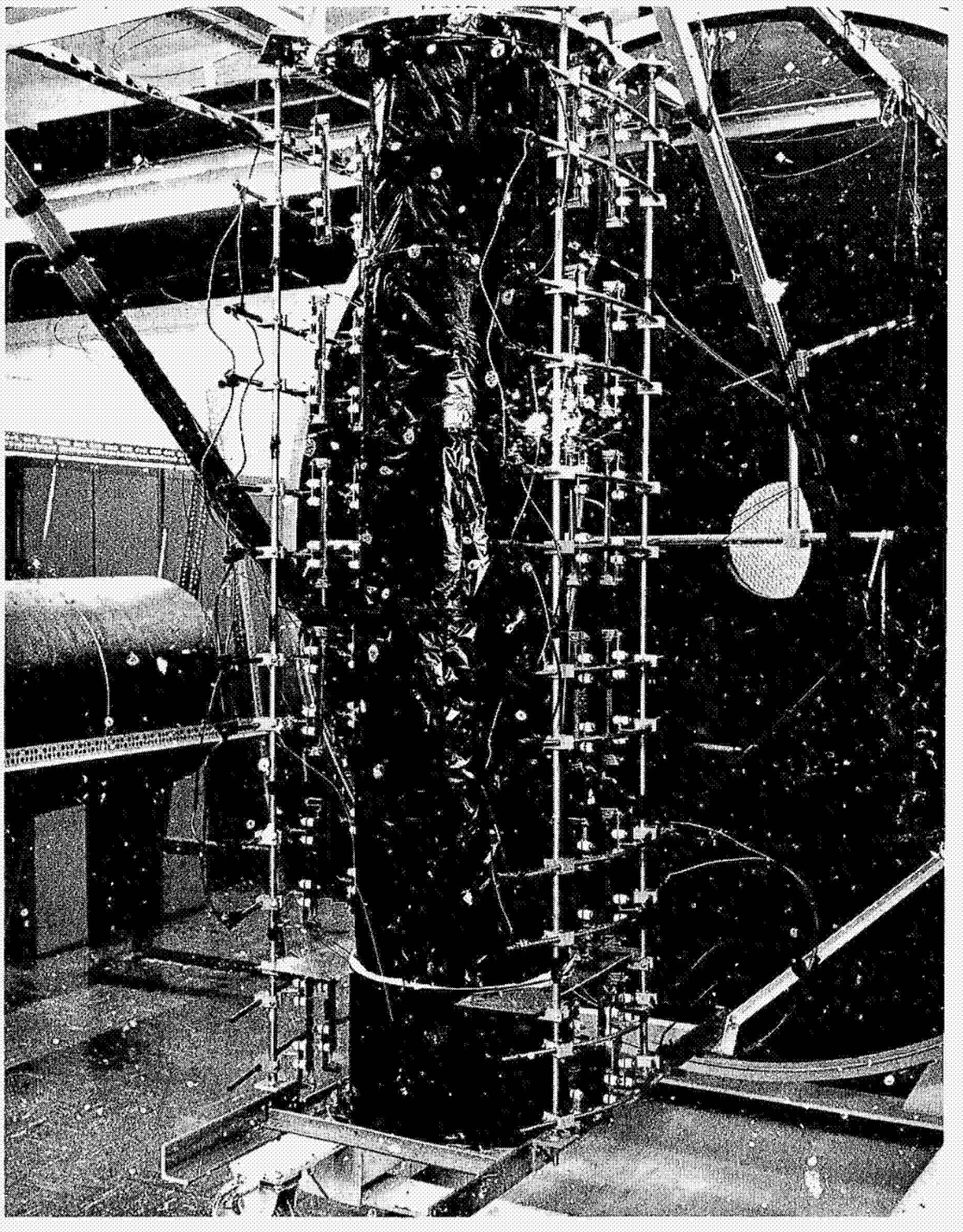


Fig. 57 Assembled Model Prior to Test

controlling side temperatures were automatically programmed to provide modeled skin transient temperatures in accordance with the analytical predictions presented in Section 3. Section A was programmed to model the results presented in Fig. 16, Sections B through F to model the temperatures in Fig. 17, and the top plate controlled to a constant temperature of 562°K modeling the assumed temperature of 297°K (75°F) for that region. The arrangement used to suspend the lamps is shown in Fig. 56.

5.4 CONTROL AND READOUT INSTRUMENTATION

Automatic controllers were used to provide separate control over the five lamp banks. A proportional set point controller was used to maintain the simulated manned section at a constant level near the required 562°K. The proportional band of this controller was ±10°K resulting in an actual temperature of 554°K for this section. The four separate banks of lamps used for transient skin temperatures were controlled with four automatic programmed temperature controllers having proportional, rate, and reset functions. The required millivolt signal to these controllers was furnished by card programmers whose cards carried the necessary transient cycles. The four systems were interconnected to drive at the same time scale and to recycle concurrently.

Readout of the thermometry and strain gage circuits was accomplished using a 300-point scanner with a scan rate of 1 point every 2 sec. The scanner output was read with a digital voltmeter having a sensitivity of ± microvolt and accuracy of ±3 microvolts. The resulting microvolt reading was both typed out for immediate use and punched into paper tape for complete data reduction using a previously prepared digital computer program. Scan cycles were initiated by a digital clock control unit and the initiation times chosen to provide sufficient data to permit a clear definition of the transient response. A complete 24-hr orbit for the prototype corresponded to 55.5 min for the model ($\theta^* = 1/26$). A scan rate of 1 point every 2 sec on the model corresponded to 1 point every 52 sec for the prototype. Therefore, each scan of 79 points required approximately 4,100 sec of prototype time.

5.4.1 Test Operation

During pumpdown of the chamber and chilling of the walls, the model was held at room temperature by leaving the shutter closed and manually adjusting the lamp banks. The transient cycles were then started and sufficient data taken to observe operating conditions.

Numerous difficulties were experienced with the external instrumentation that required delays for repair. Breakdowns occurred, one at a time, in three of the automatic temperature controllers, in the digital clock, and finally in the 300-point scanner. Considering that all of the instruments were in house less than 60 days, and that each breakdown was traced to failures of either diodes or transistors, it is adjudged that solid state instrumentation still has a way to go. No delays were caused by failure of the model or its associated mechanisms and thermometry.

A total of nine complete simulated orbital cycles were run on the model prior to recording of final data. At this point in the test, temperatures at comparative times were repeatable to within ±1°K with the primary mirror holding constant.

5.5 RESULTS

A complete tabular presentation of the transient results for the ninth cycle is included in Tables A-1 through A-18 in Appendix A. Graphical presentations taken from the tabular results are presented in this section in terms of prototype properties.

The measured temperatures of the +x and -x sides of Section A are shown in Fig. 58 and are compared to the required levels as dictated by the analytical study. The data points show that the front section automatic controllers provided the required temperature history with some minor differences. The maximum value required for the +x side was not achieved due apparently to insufficient lamp power during the maximum heat rate. As a result, less energy would have entered the tube. However, the energy involved was but a small part of that put in over the entire cycle.

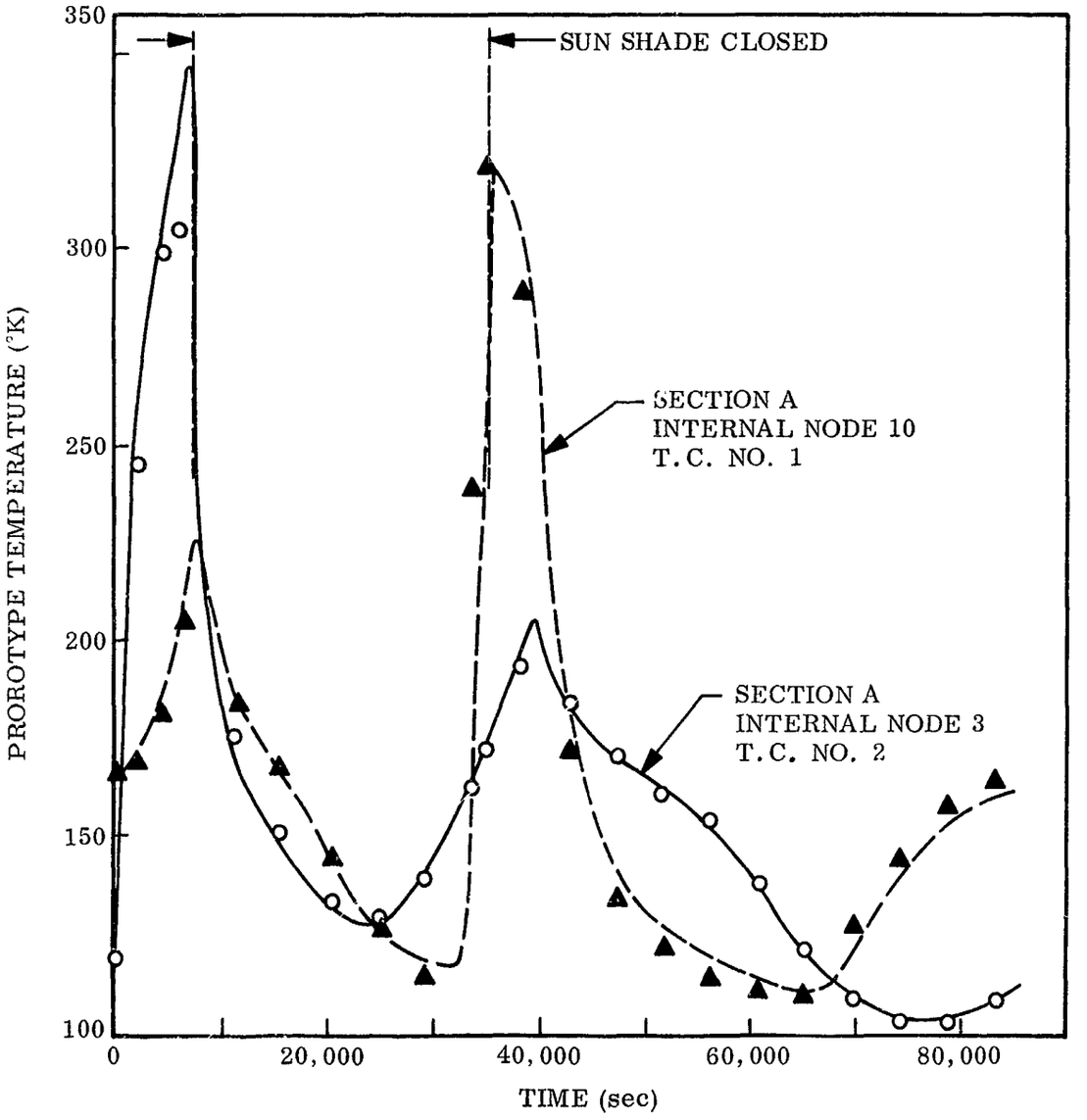


Fig. 58 Transient Thermal Behavior Section A. Points indicate experimental results. Curves show analytical predictions

The internal transient behavior of Sections B, C, and D is presented in Figs. 59 through 61. These figures are presented in terms of prototype conditions and compare measured results to analytical predictions. For these sections it is apparent that model average temperatures were lower than the predicted levels by approximately 25°K. This difference is observed to exist for all internal surfaces of the insulated tube. Transient excursions about the mean displayed similar peak-to-valley differences though the response of model internal surfaces was somewhat faster than that predicted analytically. The faster measured response was anticipated since in the analytical work all heat capacity of the insulation was placed at a surface node. Comparison of the figures indicates both lesser peak-to-valley excursions and an increase in average temperature for sections closer to the mirror. This is further demonstrated by the results presented in Fig. 62 where the primary mirror is seen to assume a temperature between that of the manned support interface and the average tube temperature. The mirror temperature is closer to the tube average internal temperature than it is to the support structure indicating that the reflecting surfaces and conductance paths between these latter two elements have provided the required thermal isolation. The conductive isolation is further demonstrated by comparison of the temperatures measured on the rear of the mirror surface. Those thermocouples located near mirror attachment points (T.C. Nos. 16 and 21) indicated temperatures nearly identical to those located at other locations on the mirror (for example, T.C. Nos. 17 to 20). Therefore, the presence of a measurable quantity of conducted energy was not observed.

The measured thermal history of one of the secondary support rods is indicated in Fig. 63. The base of the rods was at a temperature higher than the primary mirror due to conduction from the manned interface. This is shown by comparison of thermocouple 24 on the rod end and 27 adjacent to the mirror. Temperatures along the length of the rods removed from the primary were close to those of the adjacent tube sections indicating a strong thermal radiation link in this region.

Elongation of the rods as determined from the strain gage measurements is shown in Fig. 64. All three of the rods exhibited nearly identical elongations and temperature histories. These results were checked against computed elongations based upon the data of Fig. 63. The results of the computation are indicated by a dashed curve on

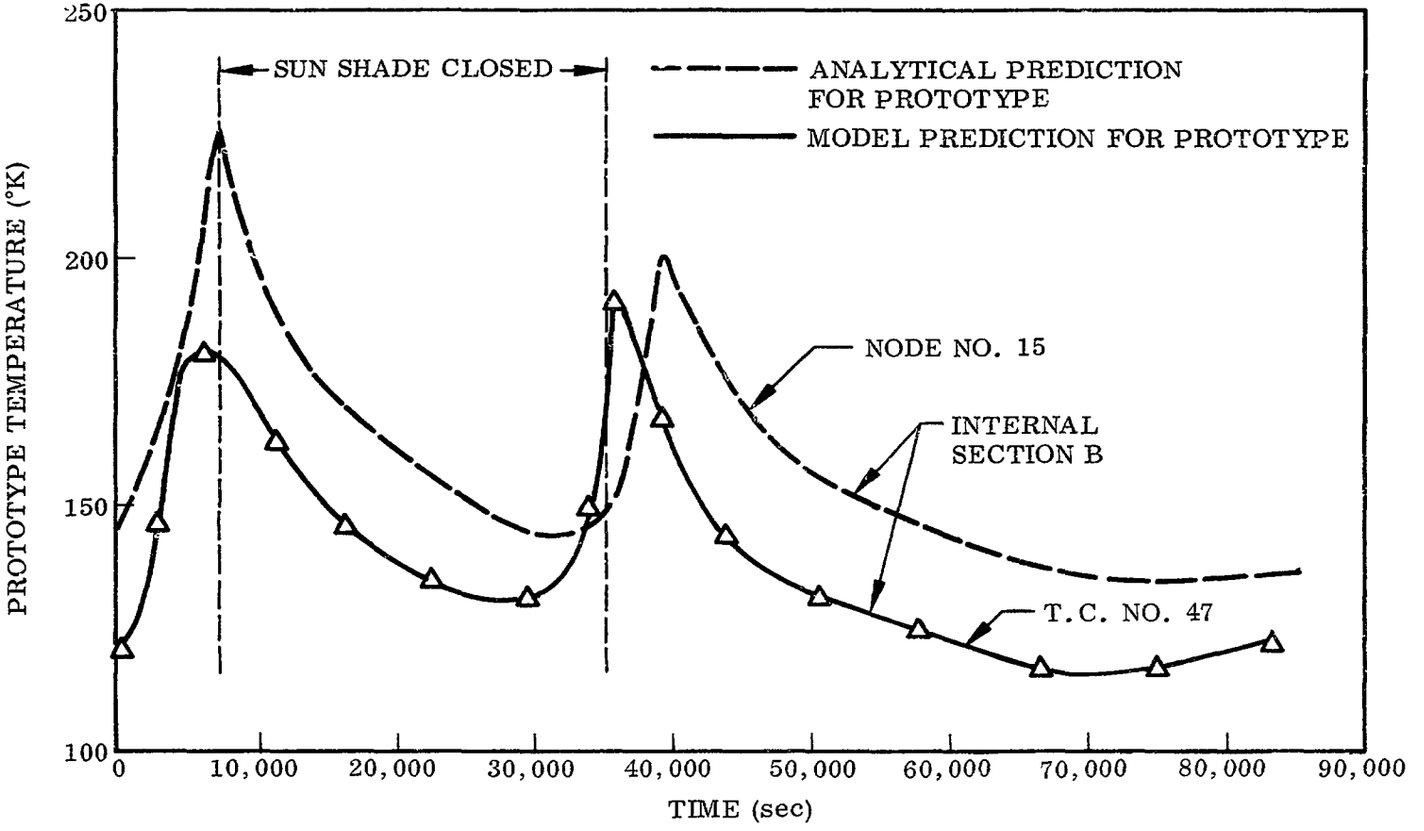


Fig. 59 Transient Thermal Behavior Section B

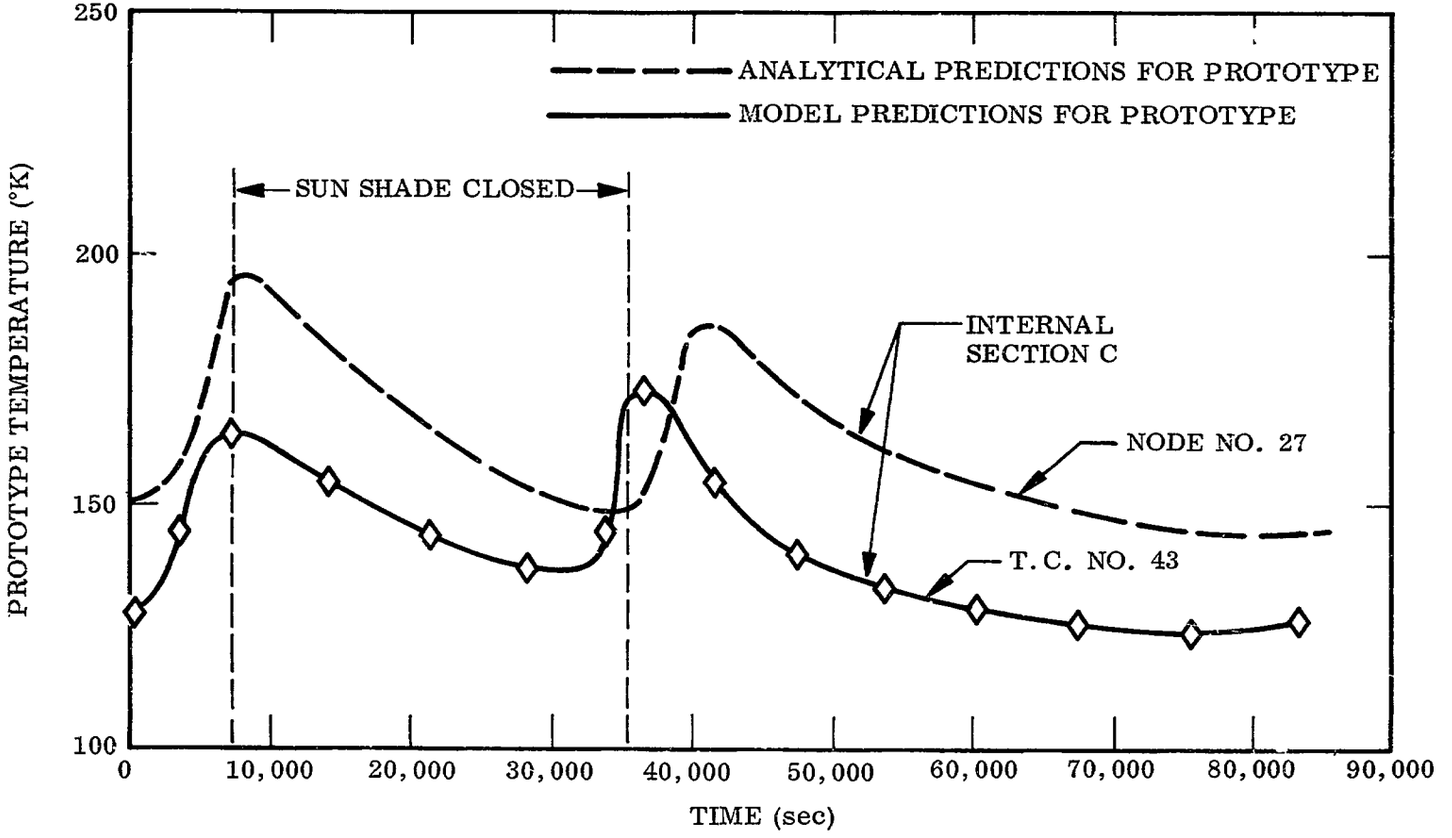


Fig. 60 Transient Thermal Behavior Section C

LOCKHEED PALO ALTO RESEARCH LABORATORY
LOCKHEED MISSILES & SPACE COMPANY
A GROUP DIVISION OF LOCKHEED AIRCRAFT CORPORATION

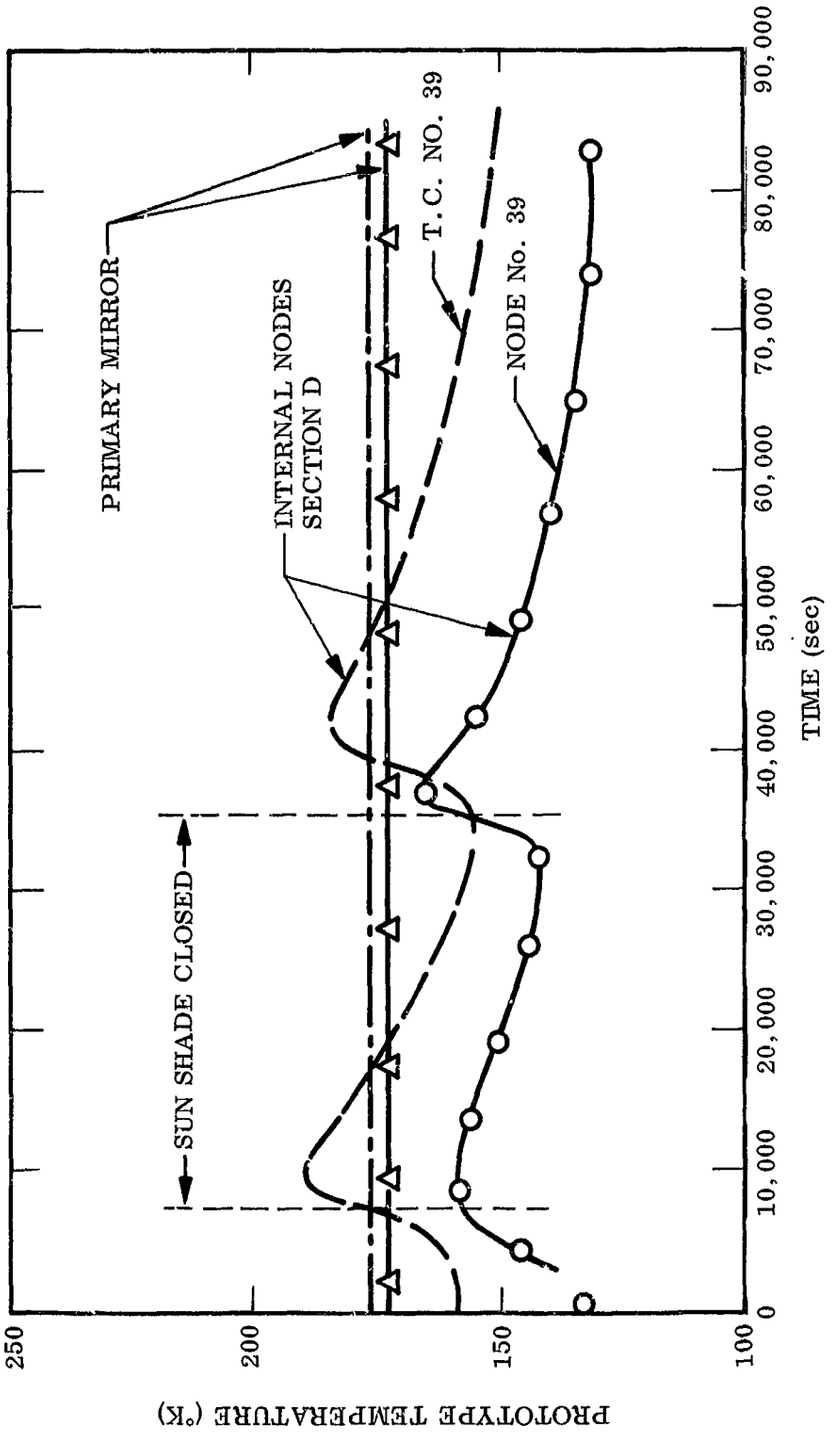


Fig. 61 Transient Thermal Behavior Section D and Primary Mirror

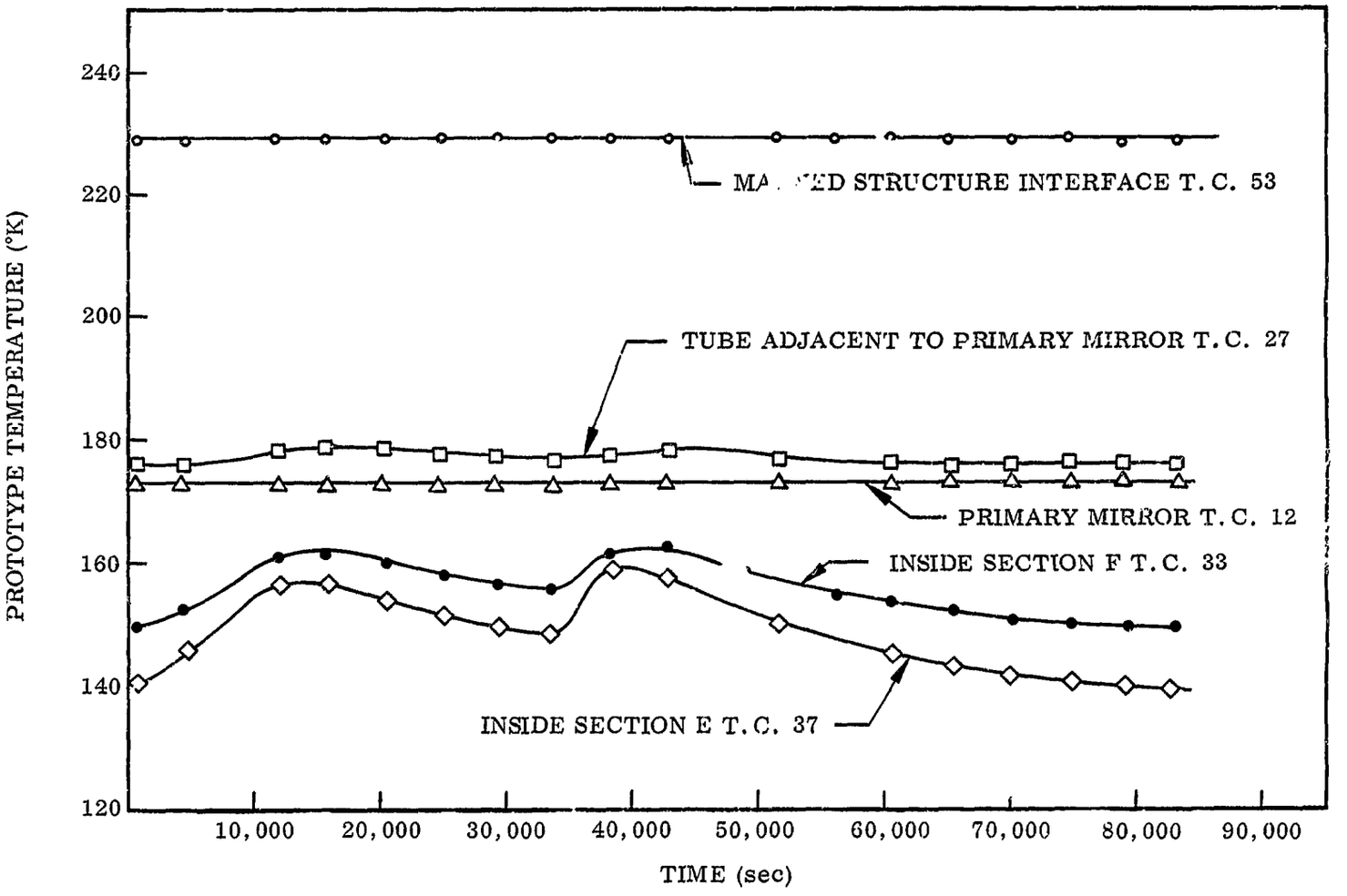


Fig. 62 Temperature History for Prototype Primary Mirror Surrounds

LOCKHEED PALO ALTO RESEARCH LABORATORY
LOCKHEED MISSILES & SPACE COMPANY
A GROUP DIVISION OF LOCKHEED AIRCRAFT CORPORATION

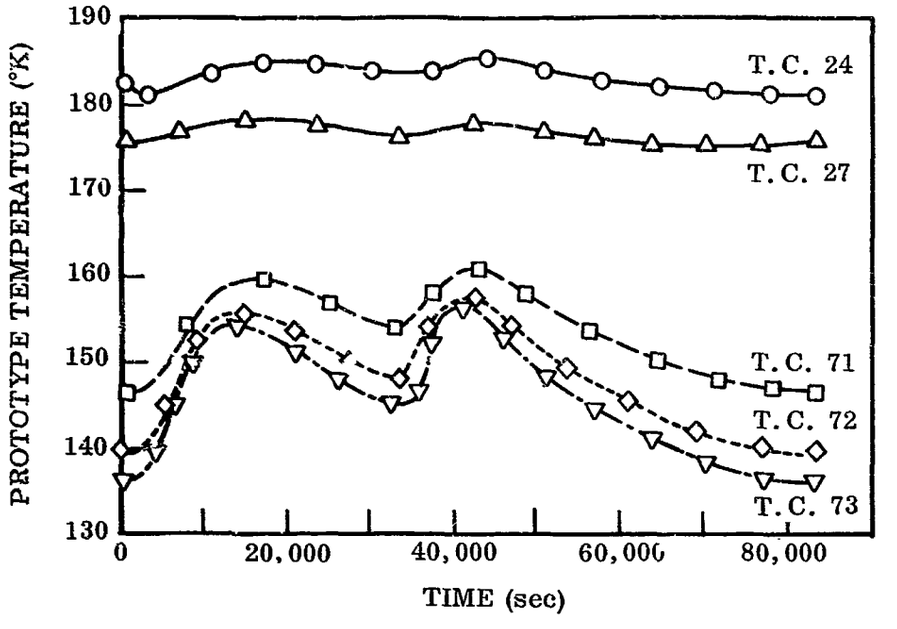


Fig. 63 Temperature History for Prototype Secondary Support Rods

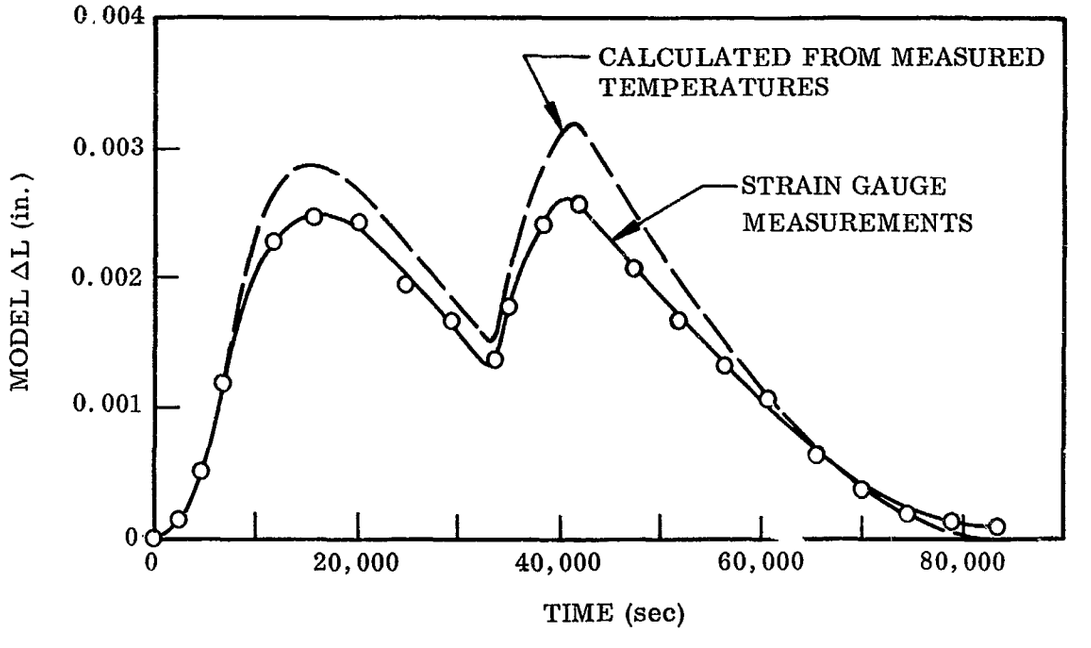


Fig. 64 Thermal Expansion of Model Secondary Support Rods

Fig. 64. Exact agreement between the measured and computed values was not obtained; however, this is due primarily to the fact that temperatures were measured at only four points on the rods requiring a gross estimate of the gradients existing at the hot end. Additional thermometry would have provided the means for a more precise comparison. An estimate of prototype rod elongation, through use of the previously stated model ratio $y^* = 5.45$, results in a maximum predicted change in rod length during orbit for the prototype of $y_p = 0.000188$ cm (0.00048 in.). This corresponds to a change in optical path between the primary mirror and exit optics of 0.000376 cm.

Temperatures on the primary mirror were predicted from the model laws to be constant with time to within ±0.5°K. Front-to-back temperature difference predictions indicated less than ±0.4°K and edge-to-edge temperature differences 0.15°K. These values fall well within the design goals of the prototype. The predicted values at selected times during the orbit are given in Table 14.

Table 14

PROTOTYPE PRIMARY MIRROR TEMPERATURE HISTORY TEMPERATURE – °K
(Determined From Mode Measurements)

Thermo-couple	Location	Time (sec)				
		0	20,300	33,800	42,900	60,900
11	Front Center	172.1	172.8	172.6	172.7	173.0
12	Front Middle	172.2	172.5	172.7	173.1	173.0
13	Front Edge	172.4	172.8	172.9	173.3	173.3
16	Rear Center	172.3	172.7	172.9	173.1	173.2
17	Rear Middle	172.9	172.9	173.4	173.7	173.5
18	Rear Edge	173.0	173.0	173.3	173.6	173.7
12	1 Front Middle	172.2	172.5	172.7	173.1	173.0
14	2 Front Middle	172.1	172.5	172.7	173.0	172.9
15	3 Front Middle	172.1	172.4	172.7	173.0	172.8
17	1 Rear Middle	172.9	172.9	173.4	173.7	173.5
22	2 Rear Middle	172.8	172.8	173.2	173.4	173.4
23	3 Rear Middle	172.8	172.8	173.3	173.5	173.4

Section 6
DISCUSSION

The previous sections have presented the details of work performed in completion of a model study whose purpose was to establish the feasibility of modeling the thermal and structural performance of space telescopes. The results obtained indicate that modeling procedures will provide realistic information on the space performance of telescope systems and also provide the means to study the influence of design changes prior to prototype construction and fabrication.

This study required the expenditure of considerable effort to establish a prototype thermal design, an effort which would normally be accomplished during preliminary hardware design prior to initiation of a model program. In this program, the work was necessary due to the selection of a conceptual prototype system that was not yet in preliminary design. Numerous factors important to the thermal performance of the selected telescope had to be somewhat arbitrarily set to allow completion of the model study. Among these factors was the selection of a specific synchronous orbit, the assumption of operating conditions for the sun shutter, and conductive isolation of the primary mirror system from its supporting structure. These factors may differ from those of the final hardware since the OTES program is still undergoing changes in terms of mission objectives.

The analytical work reported in Section 3 was sufficient to establish a satisfactory estimate of flight performance and allowed selection of a fixed design concept as a basis for thermal design of the model. The use of invariant material properties in the analytical study was a necessary simplification to allow its completion. This assumption would not be appropriate for use in the final hardware thermal analysis which should include laboratory measurements of thermal properties to determine their changes with temperature. Of particular importance in this regard are the thermal properties of the primary mirror suspension system, the thermal performance of

multilayer insulation at the anticipated flight temperatures, the expansion properties of the optical elements, and the thermal properties of the honeycomb materials used as structural elements. Verification of actual values of specific heat and thermal conductivity of the honeycomb is of particular importance since these vary considerably with changes in fabrication procedures. For final hardware design, the analytical study should also include additional nodes through the multilayer insulation for determinations of transient histories, more nodes of the secondary mirror support rods, and definition of the influence of attachments between insulated tube sections. Inclusion of these additional details would considerably enhance the results obtained from analytical predictions.

Although the scope of the analytical effort performed as part of this study was insufficient to include the above refinements, the results obtained were of considerable aid in directing the model design and test effort. It was shown that the telescope tube acted essentially as an adiabatic enclosure to solar energy entering the opening. It was observed that variations in thermal conductivity of the multilayer insulation had little effect on internal performance as long as the conductivity was within an order of magnitude of the design value. Further, within this range, thermal transients from the tube exterior would be effectively damped out and would not influence the internal transient. Predictions of transient performance showed that the primary mirror, due to its large thermal mass and highly reflective surface coatings, would remain at a constant temperature within $\pm 1°K$. These findings obtained from the analyses were important factors in the establishment of the thermal model procedure.

Design of the model was accomplished within the primary constraints imposed by test chamber size, materials availability, and the maximum allowable operating temperatures for materials used as insulation. During preliminary stages of model design it was determined that only a few materials could be used to model the primary mirror within the range of allowable scale ratios. The selection of Pyrex for this purpose essentially fixed the model ratios for all remaining components. As a result of this fix on the ratios of length, temperature, and time, it was found that the remaining components could not, in all cases, be designed to exactly meet all of the requirements.

The details of the designs presented for each component show that in each case the design achieved varied slightly from an exact match to the model criteria. However, it was possible to design within satisfactory limits in terms of the heat capacities involved and the influence of transients on thermal performance.

The use of multilayer insulation on all internal surfaces of the telescope tube posed a considerable problem since no previously completed programs could be used as a guide for thermal modeling of the insulation system. The effort devoted to multilayer insulation modeling was incorporated in the program scope to determine the feasibility of modeling the selected prototype wrap at an elevated temperature ratio while maintaining properties within the limits predicted as necessary by the analytical program. Previous experimental results have shown that changes in multilayer insulation conductivity occur for variable boundary temperatures, layer densities, and thickness. These variables would also exert an influence on the model wraps; however, data in the temperature range expected for model operation were not available requiring the design and performance of experiments to obtain the necessary information.

The experiments conducted on a full- and half-scale model of the prototype wrap, using an elevated temperature ratio for the model and the criteria $K^*/t^* = 1/L^*$, proved that one-dimensional modeling of the insulation system could be accomplished. The procedures employed in the full- and half-scale studies were then extrapolated to modeling of the telescope tube with $L^* = 1/6.43$ and $T^* = 1.86$. The success achieved is verified by the telescope model test results which showed satisfactory damping of external transients propagating to the tube interior and provision of an adiabatic interior to energy from the frontal section of the tube.

An equal degree of success was not experienced in achieving the desired thermal properties for modeling of the manned experiment section interface. The insulation in this location was analytically predicted to provide a temperature of 192°K for surface areas behind the primary mirror. The model measurements led to predicted temperatures for this region of 230°K, a difference of +38°K. Modeling of the insulation for this region was complicated by high model temperatures, 562°K (534°F) for

the manned section side, which exceeded the maximum allowable temperature of the Mylar insulation system. Material substitution was required and a system of alternate layers of aluminized Kapton and Dexiglas was selected. Experimental data were available on this system at considerably different boundary temperatures. Extrapolation of the data to model conditions led to wrap composed of 18 layers each of reflector and spacer material. The measured model temperature clearly indicate that either the thermal conductivity of the modeled wrap was too high or the analytical model was insufficient in predicting temperatures for this region. Additional orbit average computations of the manned interface region were completed following the test effort for purposes of clarifying the differences in computed and modeled results. The analyses indicated that the +38°K temperature error could be attributed to a model wrap thermal conductivity that was too high by a factor of 7. In view of the extrapolation procedure required for design of the high temperature model wrap, the lack of conductivity data in the temperature region of interest and overall adequacy of the analytical thermal model, it is concluded that the conductivity of the insulation on the manned interface was too high on the order of one-half to one order of magnitude. These results show that considerable work should yet be accomplished to better define the procedures necessary for modeling of multilayer insulation. At present, programs requiring modeling of multilayer insulated prototype systems should be supported by a parallel experimental measurement program of the model insulation properties.

The overall results obtained from the model test compared favorably with the analytical predictions for the system although the overall average temperature of the tube interior fell below that of the predictions by approximately 22°K. This lower temperature was apparently caused by several separate influences. First was the failure of the heating lamps to provide sufficient energy to drive the front section through maximum levels during the simulated orbit. This can be clearly seen by inspection of Figs. 58 to 60 where the -x side failed to heat to the required maximum. However, the effect of this operational difficulty would be minor since the amount of the total cycle involved was small. The second cause of low interior heating could have been that the interior coating of Section A had an emittance below that of the value used for analysis of the prototype. The coating used on the inside was black Thermatrol paint

whose accepted value of emittance is 0.95. Measurements made directly on the model following the experiment showed that the actual room temperature emittance of the paint on the interior of the section was 0.85 ± 0.02. Additional recent measurements on small samples of a freshly prepared black Thermatrol indicate emittances of 0.87 at room temperature with decreasing values of 0.82 following a cold soak at 150°K. It appears from this evidence that the heater section painted surface had an emittance that was too low and that exposure to the low- and high-temperature cycles used in the test resulted in a further decrease. A decrease in emittance from the design value of 0.95 to a value of 0.83 would correspond, on the basis of a simple fourth power extrapolation, to a change in temperature of the tube interior from the measured value of 150°K to a value of 156°K. While this change is less than the observed 22°K, it is apparent that a low paint emittance was a contributing factor. A third factor leading to a mismatch in energy entering the tube was the fact that an exact match of temperatures for Section A at each of the analytical node locations could not be accomplished experimentally. Surface temperatures for the analytical nodes were based upon the amount of absorbed solar energy entering the tube opening during selected orbit intervals. The absorbed energy was averaged over each node and equilibrium surface temperatures computed. The radiant heating lamps used to drive Section A on the model were adjusted to provide the required surface temperatures at node centers; however, the temperatures could not be maintained out to the edges of the section as required for a complete match to the analytical model. This mismatch would also contribute to a reduction of the tube interior temperatures. The use of heater blankets covering each node location on Section A instead of the radiant lamps would probably have resulted in a better distribution of energy over the section resulting in an improved comparison with the analytical results. Each node could then be individually controlled to match the required input temperature history. Unfortunately, facilities for use of this procedure were not available during conduct of the experimental program.

The transient behavior of the model verified the expected transient behavior of the prototype in that the peak-to-valley variations decreased for sections closer to the primary mirror and that the mirror remained at an essentially constant level. It was observed that the mirror equilibrium temperature was between that of the tube and the

manned support section mounting plate with the actual value being closer to that of the tube. This observation confirms that the structure used to attach the primary mirror to the manned support section was effective in isolating it from that section. The mirror temperature is determined primarily by radiation coupling to the tube. Assuming the primary mirror to be a radiation shield between the manned support structure and the tube, and assuming a mirror emittance of 0.03, a manned support structure emittance of 0.03, and an effective emittance of the extended tube to be 1.0, gives $T_m^4 = \left(T_s^4 + 2T_t^4\right)/3$ where the mirror emittance has been considered small compared to unity. In this relation, T_m is the mirror temperature, T_s is the support structure temperature, and T_t is an average effective tube temperature. For the assumed emittances, the mirror radiation coupling is twice as strong to the tube as it is to the high temperature support structure. Using the temperatures measured in the model for T_s and T_t gives T_m = 188°K which is high compared to measured mirror temperatures of 172°K. However, the extreme simplicity of the assumed radiation shield geometry fails to account for coupling at the outer edges and emission from spaces between the mirrors. Both of these effects would tend to reduce the primary mirror temperature.

The very small transient variations of the mirror were verified to be less than ±0.5°K in comparison to predicted variations on the order of ±1°K. The accuracy of this prediction is considerably enhanced by the use of an increased temperature ratio ($T^* = 1.86$) where observations of small differences are magnified by almost a factor of two through the model laws. Temperature differences across and through the mirrors were also found to fall well within the specified tolerance of ±1°K with model measurements indicating differences on the order of ±0.3°K.

The planned scope of the experimental program included monitoring of the primary mirror temperatures from initiation of the first simulated orbit to steady state conditions so that the time required for the mirror to adjust to new conditions could be predicted. The numerous difficulties experienced with monitoring instrumentation precluded satisfactory completion of this task. Sufficient data were obtained to indicate that the mirrors in the model would require approximately 24 hr to come to a new

equilibrium point following a change in orbital conditions. This would correspond to 624 hr for the prototype mirrors. This estimate of total time to equilibrium must be considered as approximate since it is based upon an extrapolation of data gathered during the last nine successive model cycles. In spite of the experimental difficulties experienced during this program, the work accomplished satisfactorily demonstrated that a model having a much shorter time constant than the prototype can be invaluable in providing information on long-term transient conditions at the expense of relatively short experimental run times.

Structural modeling observations were limited in scope to a determination of elongation of the secondary support rods. This limitation was imposed fundamentally by the design approach used in the prototype wherein a temperature range was selected where quartz has a near zero thermal expansivity. In addition, the thermal design provided for exclusion of thermal transients around the mean or gradients through the mirror. Since these design conditions result in zero or extremely small thermal expansion for the primary mirror, the possibility of physically modeling and measuring distortions on the mirror elements was virtually eliminated. The value of the model under these circumstances is limited to the provision of prototype temperatures which can be used for computation of optical performance. For example, the model herein indicated that the prototype primary mirror would operate through an average temperature range of 172.6 ± 0.4°K during its orbit. For a spherical optic, the change in focal length due to a uniform temperature rise is given by $\Delta f = \alpha f \Delta T$ where f is the focal length, α the thermal expansion coefficient, and T the temperature. At 172°K, the thermal expansion coefficient of fused quartz is approximately 2×10^{-7} cm/cm °K giving the f/3 2-meter diameter mirror a change in focal length of $\Delta f = 4.8 \times 10^{-7}$ meters. This change in focal length is easily compensated for by the active primary mirror mount. The change in optical path length of the prototype due to elongation of the secondary support rods during a single orbit was predicted to be 3.76×10^{-6} meters and can also be compensated for by the active mirror mount. The small magnitude of these changes shows the difficulties in obtaining direct measurements of changes in dimension on a small-scale model. Except for the secondary support rods where material substitution allowed the attainment of a $y^* = 5.45$, y^* being the ratio of changes in rod length

between the model and prototype, direct measurements of changes in optical component dimensions were not possible. This experience indicates that the best approach to obtaining optical performance characteristics from the thermal model of a space telescope is analytical wherein the predicted temperatures obtained from the model are used as input to a rigorous structural analysis.

Section 7

CONCLUSIONS

The conclusions reached as a result of the program reported in the previous sections are:

- Thermal modeling of large space telescope systems is a procedure that can be used to provide accurate information on the flight thermal performance of the system. On the basis of work completed, it is probable that the limiting scale ratio for these studies will be on the order of 1/7 due to difficulties in providing proper thermophysical properties in the model and in maintaining necessary manufacturing tolerances. Modeling at increased temperature ratios and decreased time ratios allows rapid and accurate observations of transient thermal histories.
- Structural modeling concurrent with thermal modeling of space flight systems is a potentially useful procedure for studies of changes in structural dimensions. For space telescopes the technique is limited to gross changes in the optical system unless optical bench evaluation techniques are incorporated into the experiment. The necessity to select materials that satisfy both the thermal and structural modeling criteria considerably restricts the model designer and necessitates compromises which detract from exact geometric simulation. For a model test similar to the one performed during this program, the best technique for evaluation of optical performance would be analytical using thermal data as input measured temperatures to establish changes in optical performance.
- Thermal modeling of multilayer insulation systems is presently limited to simulation of the perpendicular thermal conductivity. Using identical materials requires geometric distortion of thicknesses which results in loss of control over the parallel thermal conductivity. These conclusions are limited to scale and temperature ratios similar to those used in this program and may

not necessarily be true under other conditions. Modeling of multilayer insulation should receive considerably more attention to broaden the base of experience in this area.

- Completion of the analytical and experimental effort on the 2-meter OTES telescope showed that its conceptual thermal design will provide a time average temperature of the primary optic near 175°K. Variations of mirror average temperatures about the mean will be approximately ±0.5°K causing changes in focal length on the order of 5×10^{-7} meters. Thermal transients propagating down the tube will cause secondary support rod elongations on the order of 4×10^{-6} meters. These changes in dimensions can be compensated for by the primary mirror active mount.
- Th orbital conditions selected for this study were chosen because of the considerable variation of thermal inputs which were expected to cause large thermal transients. Time was insufficient to include experimental studies of other orbital conditions wherein the average primary mirror temperature would increase or decrease according to the γ angles and shutter operating cycles. Inclusion of these studies would have considerably increased the overall worth of the results in terms of changes in mirror average temperature.

Section 8

REFERENCES

1. R. E. Rolling, Thermal Scale Modeling in a Simulated Space Environment, N-05-66-1, Lockheed Palo Alto Research Laboratory, NASA, Marshall Space Flight Center, Jun 1966

2. D. L. Adkins, "Scaling of Transient Temperature Distributions of Simple Bodies in a Space Chamber," Thermophysics and Temperature Control of Spacecraft and Entry Vehicles, G. B. Heller, ed., New York, Academic Press, 1966

3. B. P. Jones, "Thermal Similitude Studies," J. Spacecraft and Rockets, Vol. 1, Jul 1964

4. B. T. Chao and G. L. Wedekind, "Similarity Criteria for Thermal Modeling of Spacecraft," J. Spacecraft and Rockets, Vol. 2, Mar 1965

5. P. L. Miller and J. A. Wiebelt, "Thermal Modeling in a Simulated Space Environment," Thermophysics of Spacecraft and Planetary Bodies, Progress in Astronautics and Aeronautics, Vol. 20, New York, Academic Press, 1967

6. K. W. Nutt and J. A. van der Bliek, "Some Aspects of Thermal Model Testing in Space Chambers," Thermophysics of Spacecraft and Planetary Bodies, Progress in Astronautics and Aeronautics, Vol. 20, New York, Academic Press, 1967

7. F. Gabron, R. W. Johnson, J. M. F. Vickers, and J. W. Lucas, "Thermal Scale Modeling of the Mariner IV Spacecraft," presented at AIAA 3rd Aerospace Sciences Meeting, New York, Jan 1966

8. F. Gabron and R. W. Johnson, "Thermal Scale Modeling of a Modified Prototype of the Mariner Mars 64 Spacecraft," AIAA Paper No. 65-386, presented at AIAA Second Annual Meeting, San Francisco, Jul 1965

9. R. K. Thompson, V. G. Klockzien, and G. E. Dufoe, "Analyses and Tests of Full-Size and Scaled Spacecraft Models in a Simulated Space Environment," AIAA/IES/ASTM Space Simulation Conference Proceedings, Houston, 1966

10. R. E. Rolling, "Thermal Modeling of a Truncated Cone in a Simulated Space Environment," AIAA/IES/ASTM Space Simulation Conference Proceedings, Houston, 1966

11. H. F. Wischnia, Interim Report Study for an Optical Technology Apollo Extension System, Perkin-Elmer Engineering Report No. 8319, submitted to NASA/Marshall under Contract NAS 8-20255, 15 Apr 1966

12. F. Gabron and A. A. Fowle, "Thermal and Structural Scale-Modeling of Optical Systems," AIAA/IES/ASTM Space Simulation Conference Proceedings, Houston, 1966

13. R. M. Coston, Handbook of Thermal Design Data for Multilayer Insulation Systems, LMSC-A847882, Vol. II, 25 Jun 1967; Final report prepared by Lockheed Missiles & Space Company for NASA/MSFC under Contract NAS 8-20353

14. K. N. Marshall and R. A. Breuch, "Optical Solar Reflector: A Highly Stable, Low α_s/ϵ Spacecraft Thermal Control Surface," J. Spacecraft and Rockets, Vol. 5, No. 9, Sep 1968

15. G. R. Cunnington, Jr., C. A. Zierman, A. I. Funai, and A. Lindahn, "Performance of Multilayer Insulation Systems for Temperatures to 700°K," NASA CR-907, Oct 1967; prepared by Lockheed Palo Alto Research Laboratory for NASA/Ames Research Center under Contract NAS 2-2441

Appendix A
TABULAR RESULTS

The numerical data obtained from the telescope model test program are presented in tabular form in this appendix. The tables were output by a data reduction computer program and contain all information used for preparation of the graphical results presented in Section 5.

The computer program was designed to accept a punched tape input from the data logging digital voltmeter scanning system, convert the digital output to thermocouple response, compute model temperatures by interpolation of input response tables, and convert the model temperatures to prototype temperatures.

Instrumentation of the model and test chamber required 79 separate thermocouples. Sixty-three (T.C. No. 1 to 63) were direct reading ice bath referenced thermocouples attached to various locations on the model. Two (T.C. No. 64 and 65) were direct reading ice bath referenced and attached to the lamp support posts. Nine (T.C. No. 71 to 79) were differential thermocouples hooked up as direct reading for data reduction purposes and mounted on the secondary mirror support rods. One (T.C. No. 70) was differential to T.C. No. 36, hooked up as direct reading for data reduction purposes, and mounted in the edge of the multilayer insulation in Section E.

The model time and prototype time listed at the beginning of each table is the time that the scan is started. Each point requires 2 sec for data logging which corresponds to 42 sec of prototype time. A complete scan of the system required 158 sec real time corresponding to 4068 sec of prototype time. These times must be accounted for in use of the data.

A listing of the thermocouple locations is presented for the convenience in using Tables A-1 through A-18.

THERMOCOUPLE LOCATIONS

T.C. No.	Locations
1	- x axis heat section
2	+ x axis heat section
3	- x heat section
4	heat section middle
5	+ x heat section
6	+ x heat section
7	heat section middle
8	- x heat ction
9	Shutter middle
10	Shutter edge
11	Mirror 1 front surface edge
12	Mirror 1 front surface middle
13	Mirror 1 front surface near center hole
14	Mirror 2 front surface middle
15	Mirror 3 front surface middle
16	Mirror 1 rear surface near center hole
17	Mirror 1 rear surface middle
18	Mirror 1 rear surface outer edge
19	Mirror 1 rear surface outer edge
20	Mirror 1 rear surface outer edge
21	Mirror 1 rear surface near mount
22	Mirror 2 rear surface middle
23	Mirror 3 rear surface middle
24	Quartz tube No. 1 near primary mirror
25	Quartz tube No. 2 near primary mirror
26	Quartz tube No. 3 near primary mirror
27	Inside tube surface near mirror 1
28	Inside tube surface between mirror 2 and 3
29	Secondary mirror
30	Secondary mirror support housing
31	Inside section F + x
32	Outside section F + x
33	Inside section F - x
34	Outside section F - x
35	Inside section E + x
36	Outside section E + x
37	Inside section E - x
38	Outside section E - x
39	Inside section D + x

THERMOCOUPLE LOCATIONS (Continued)

T.C. No.	Location	
40	Outside section D	+ x
41	Inside section D	- x
42	Outside section D	- x
43	Inside section C	+ x
44	Outside section C	+ x
45	Inside section C	- x
46	Outside section C	- x
47	Inside section B	+ x
48	Outside section B	+ x
49	Inside section B	- x
50	Outside section B	- x
51	Inside section D	
52	Inside section D	
53	Tube side of top plate near center	
54	Tube side of top plate near center	
55	Tube side of top plate near tube edge	
56	Tube side of top plate near tube edge	
57	Tube side of top plate outside	
58	Tube side of top plate outside	
59	Under lamp 3-1/4 in. from center	
60	Between lamps 3-1/4 in. from center	
61	Center hole top plate	
62	Between lamps 3-1/4 in from center of top plate	
63	Between lamps edge of top plate	
64	Lamp support structure	
65	Lamp support structure	
66	System monitor for zero level check of chamber	
67	System monitor for zero level check of telescope	
68	System monitor for zero level check of lamps	
69	System monitor for zero level check of scanner	
70	Edge of insulation blanket near T.C. No. 36	
71	Secondary support tube No. 1	
72	Secondary support tube No. 1	
73	Secondary support tube No. 1	
74	Secondary support tube No. 2	
75	Secondary support tube No. 2	
76	Secondary support tube No. 2	
77	Secondary support tube No. 3	
78	Secondary support tube No. 3	
79	Secondary support tube No. 3	

Table A-1

CYCLE NO. 9-17 TIME FROM START MODEL: 17 sec
TIME FROM START PROTO: 452 sec

PT. NO.	DEG F MODEL	DEG K MODEL	DEG K PROTOTYPE
1	97.58	309.43	166.36
2	-61.14	221.25	118.95
3	12.63	262.24	140.99
4	-65.05	219.08	117.79
5	-74.81	213.66	114.87
6	-71.66	215.41	115.81
7	-62.72	220.38	118.48
8	11.91	261.84	140.77
9	-77.90	211.94	113.95
10	-93.39	203.34	109.32
11	116.82	320.12	172.11
12	117.25	320.36	172.24
13	117.88	320.71	172.43
14	116.95	320.19	172.15
15	116.69	320.05	172.07
16	117.50	320.50	172.31
17	119.53	321.63	172.92
18	119.87	321.82	173.02
19	118.31	320.95	172.55
20	118.22	320.90	172.53
21	119.19	321.44	172.82
22	119.11	321.39	172.79
23	119.07	321.37	172.78
24	152.55	339.97	182.78
25	148.16	337.53	181.47
26	143.93	335.19	180.21
27	129.12	326.96	175.78
28	97.75	309.53	166.41
29	3.33	257.07	138.21
30	-32.12	237.38	127.62
31	35.92	275.18	147.94
32	-157.45	167.75	90.19
33	40.41	277.67	149.29
34	192.55	362.19	194.73
35	10.67	261.15	140.40
36	-172.48	159.40	85.70
37	8.07	259.70	139.63
38	185.04	358.02	192.48
39	-14.85	246.97	132.78
40	-182.59	153.78	82.68

Table A-1 (Cont.)

CYCLE NO. 9-17 CONT'D

PT. NO.	DEG F MODEL	DEG K MODEL	DEG K PROTOTYPE
41	-16.55	246.03	132.27
42	181.38	355.99	191.39
43	-34.35	236.14	126.96
44	-192.30	148.39	79.78
45	-36.17	235.13	126.41
46	186.77	358.98	193.00
47	-42.67	231.52	124.47
48	-190.50	149.39	80.32
49	-52.55	226.03	121.52
50	160.20	344.22	185.07
51	-12.95	248.03	133.35
52	32.21	273.11	146.84
53	307.49	426.05	229.06
54	295.92	419.62	225.60
55	321.87	434.04	233.36
56	315.96	430.75	231.59
57	127.20	325.89	175.21
58	127.28	325.93	175.23
59	538.81	554.56	298.15
60	533.77	551.76	296.65
61	538.81	554.56	298.15
62	533.46	551.59	296.55
63	516.41	542.12	291.46
64	-142.23	176.21	94.73
65	-171.03	160.20	86.13
66	32.30	273.17	146.86
67	32.30	273.17	146.86
68	32.30	273.17	146.86
69	32.35	273.19	146.88
70	-99.94	199.70	107.36
71	31.69	272.83	146.68
72	7.49	259.38	139.45
73	-3.91	253.05	136.05
74	30.33	272.07	146.27
75	8.21	259.78	139.67
76	-0.50	254.95	137.07
77	32.25	273.14	146.85
78	8.99	260.21	139.90
79	-3.51	253.27	136.17

Table A-2

CYCLE NO. 9-174 TIME FROM START MODEL: 174 sec
TIME FROM START PROTO: 4520 sec

PT. NO.	DEG F MODEL	DEG K MODEL	DEG K PROTOTYPE
1	153.20	340.33	182.97
2	530.94	550.19	295.80
3	96.10	308.61	165.92
4	71.60	295.00	158.60
5	226.08	380.82	204.74
6	248.87	393.48	211.55
7	77.56	298.31	160.38
8	96.23	308.69	165.96
9	-7.77	250.90	134.89
10	-33.94	236.37	127.08
11	116.36	319.86	171.97
12	117.50	320.50	172.31
13	118.56	321.09	172.63
14	117.25	320.36	172.24
15	116.95	320.19	172.15
16	117.46	320.48	172.30
17	119.49	321.61	172.91
18	119.28	321.49	172.84
19	117.92	320.74	172.44
20	118.22	320.90	172.53
21	119.15	321.42	172.81
22	119.11	321.39	172.79
23	119.03	321.35	172.77
24	148.20	337.55	181.48
25	147.46	337.14	181.26
26	145.20	335.89	180.59
27	130.58	327.77	176.22
28	99.44	310.47	166.92
29	4.15	257.53	138.46
30	24.76	268.98	144.61
31	46.15	280.86	151.00
32	-158.10	167.39	89.99
33	49.17	282.54	151.90
34	188.90	360.17	193.64
35	26.89	270.16	145.25
36	-173.66	158.75	85.35
37	27.55	270.53	145.44
38	180.55	355.53	191.14
39	27.22	270.34	145.35
40	-183.78	153.12	82.32

Table A-2 (Cont.)

CYCLE NO. 9-174 CONT'D

PT. NO.	DEG F MODEL	DEG K MODEL	DEG K PROTOTYPE
41	32.25	273.14	146.85
42	177.69	353.94	190.29
43	52.14	284.19	152.79
44	-188.95	150.25	80.78
45	62.65	290.03	155.93
46	182.64	356.69	191.77
47	86.29	303.16	162.99
48	-173.59	158.79	85.37
49	124.60	324.45	174.43
50	156.19	342.00	183.87
51	31.17	272.54	146.53
52	32.21	273.11	146.84
53	307.42	426.01	229.04
54	295.78	419.54	225.56
55	321.84	434.02	233.34
56	315.78	430.66	231.54
57	127.91	326.28	175.42
58	129.25	327.03	175.82
59	538.81	554.56	298.15
60	533.14	551.41	296.46
61	538.81	554.56	298.15
62	533.14	551.41	296.46
63	515.78	541.77	291.27
64	-135.96	179.69	96.61
65	-170.00	160.78	86.44
66	32.21	273.11	146.84
67	32.25	273.14	146.85
68	32.25	273.14	146.85
69	32.30	273.17	146.86
70	-100.70	199.28	107.14
71	38.08	276.38	148.59
72	17.94	265.19	142.58
73	9.66	260.59	140.10
74	36.62	275.57	148.15
75	18.42	265.46	142.72
76	14.02	263.01	141.40
77	38.87	276.82	148.83
78	20.14	266.41	143.23
79	11.00	261.34	140.50

Table A-3

CYCLE NO. 9-450 TIME FROM START MODEL: 450 sec
TIME FROM START PROTO: 11,720 sec

PT. NO.	DEG F MODEL	DEG K MODEL	DEG K PROTOTYPE
1	158.83	343.46	184.66
2	135.23	330.35	177.61
3	94.59	307.77	165.47
4	54.09	285.27	153.37
5	77.87	298.48	160.47
6	79.38	299.32	160.93
7	54.55	285.53	153.51
8	91.30	305.94	164.49
9	66.37	292.09	157.04
10	65.34	291.52	156.73
11	119.58	321.65	172.93
12	117.88	320.71	172.43
13	118.43	321.02	172.59
14	118.09	320.83	172.49
15	117.50	320.50	172.31
16	118.43	321.02	172.59
17	119.75	321.75	172.98
18	119.66	321.70	172.96
19	118.43	321.02	172.59
20	118.60	321.11	172.64
21	119.24	321.47	172.83
22	119.07	321.37	172.78
23	119.19	321.44	172.82
24	157.13	342.51	184.15
25	156.44	342.13	183.94
26	155.02	341.34	183.52
27	137.55	331.64	178.30
28	112.20	317.56	170.73
29	35.87	275.15	147.93
30	72.84	295.69	158.97
31	76.76	297.86	160.14
32	-162.12	165.16	88.79
33	78.89	299.05	160.78
34	139.09	332.49	178.76
35	65.56	291.64	156.80
36	-178.55	156.03	83.89
37	65.20	291.45	156.69
38	130.21	327.56	176.11
39	66.37	292.09	157.04
40	-189.58	149.90	80.59

Table A-3 (Cont.)

CYCLE NO. 9-450 CONT'D

PT. NO.	DEG F MODEL	DEG K MODEL	DEG K PROTOTYPE
41	67.58	292.77	157.40
42	127.20	325.89	175.21
43	72.04	295.25	158.73
44	-196.98	145.79	78.38
45	73.02	295.79	159.03
46	131.54	328.30	176.50
47	81.27	300.37	161.49
48	-184.48	152.74	82.12
49	78.00	298.56	160.51
50	107.95	315.19	169.46
51	67.44	292.69	157.36
52	32.11	273.06	146.81
53	308.03	426.35	229.22
54	296.53	419.96	225.79
55	322.23	434.24	233.46
56	316.03	430.79	231.61
57	128.58	326.65	175.62
58	129.08	326.93	175.77
59	538.81	554.56	298.15
60	533.14	551.41	296.46
61	538.81	554.56	298.15
62	533.14	551.41	296.46
63	515.78	541.77	291.27
64	-128.91	183.61	98.71
65	-168.48	161.62	86.89
66	32.16	273.09	146.82
67	32.16	273.09	146.82
68	32.11	273.06	146.81
69	32.11	273.06	146.81
70	-102.57	198.24	106.58
71	70.36	294.31	158.23
72	59.59	288.33	155.02
73	54.82	285.68	153.59
74	69.10	293.61	157.86
75	60.00	288.56	155.14
76	58.82	287.90	154.78
77	70.89	294.60	158.39
78	61.08	289.15	155.46
79	55.68	286.16	153.85

Table A-4

CYCLE NO. 9-605 TIME FROM START MODEL: 605 sec
TIME FROM START PROTO: 15,800 sec

PT. NO.	DEG F MODEL	DEG K MODEL	DEG K PROTOTYPE
1	103.68	312.82	168.18
2	47.84	281.80	151.51
3	49.72	282.85	152.07
4	10.72	261.18	140.42
5	19.71	266.17	143.10
6	20.99	266.88	143.49
7	11.67	261.71	140.70
8	47.61	281.67	151.44
9	57.55	287.19	154.40
10	56.68	286.71	154.15
11	118.52	321.06	172.62
12	118.09	320.83	172.49
13	119.49	321.61	172.91
14	118.05	320.81	172.48
15	117.84	320.69	172.41
16	118.81	321.23	172.70
17	119.79	321.77	173.00
18	119.75	321.75	172.98
19	118.52	321.06	172.62
20	118.64	321.14	172.65
21	119.28	321.49	172.84
22	119.07	321.37	172.78
23	119.28	321.49	172.84
24	159.64	343.91	184.90
25	158.62	343.35	184.59
26	157.29	342.60	184.20
27	138.46	332.15	178.57
28	114.66	318.92	171.46
29	44.31	279.84	150.45
30	53.68	285.05	153.25
31	77.51	298.28	160.37
32	-164.04	164.09	88.22
33	79.96	299.64	161.10
34	79.29	299.27	160.90
35	63.90	290.72	156.30
36	-181.05	154.64	83.14
37	62.78	290.10	155.97
38	69.10	293.61	157.86
39	54.68	285.60	153.55
40	-192.81	148.11	79.63

Table A-4 (Cont.)

CYCLE NO. 9-605 CONT'D

PT. NO.	DEG F MODEL	DEG K MODEL	DEG K PROTOTYPE
41	54.77	285.65	153.58
42	67.31	292.62	157.32
43	49.22	282.57	151.92
44	-200.89	143.62	77.21
45	48.85	282.36	151.81
46	71.24	294.80	158.50
47	46.42	281.01	151.08
48	-192.73	148.15	79.65
49	42.43	278.80	149.89
50	50.50	283.28	152.30
51	56.36	286.54	154.05
52	31.78	272.88	146.71
53	308.46	426.59	229.35
54	296.93	420.18	225.91
55	322.58	434.43	233.57
56	316.06	430.81	231.62
57	128.08	326.38	175.47
58	127.15	325.86	175.20
59	538.81	554.56	298.15
60	533.14	551.41	296.46
61	538.81	554.56	298.15
62	533.46	551.59	296.55
63	515.78	541.77	291.27
64	-128.73	183.71	98.77
65	-168.21	161.77	86.97
66	31.97	272.98	146.77
67	31.92	272.96	146.75
68	32.11	273.06	146.81
69	32.02	273.01	146.78
70	-103.33	197.81	106.35
71	75.11	296.95	159.65
72	62.65	290.03	155.93
73	55.77	286.21	153.87
74	74.09	296.38	159.35
75	63.14	290.30	156.07
76	58.66	287.92	154.80
77	75.47	297.15	159.76
78	63.99	290.77	156.33
79	55.95	286.31	153.93

Table A-5

CYCLE NO. 9-780 TIME FROM START MODEL: 780 sec
TIME FROM START PROTO: 20,300 sec

PT. NO.	DEG F MODEL	DEG K MODEL	DEG K PROTOTYPE
1	25.33	269.29	144.78
2	-4.60	252.66	135.84
3	-5.10	252.39	135.69
4	-27.27	240.07	129.07
5	-21.97	243.02	130.65
6	-20.51	243.83	131.09
7	-25.56	241.02	129.58
8	-5.99	251.89	135.43
9	35.02	274.68	147.68
10	27.22	270.34	145.35
11	119.11	321.39	172.79
12	118.14	320.85	172.50
13	119.11	321.39	172.79
14	118.05	320.81	172.48
15	117.80	320.66	172.40
16	118.69	321.16	172.67
17	119.62	321.68	172.94
18	119.92	321.84	173.03
19	118.60	321.11	172.64
20	118.43	321.02	172.59
21	119.03	321.35	172.77
22	119.03	321.35	172.77
23	119.15	321.42	172.81
24	160.24	344.24	185.08
25	158.42	343.23	184.53
26	156.96	342.42	184.10
27	137.55	331.64	178.30
28	113.81	318.45	171.21
29	44.82	280.12	150.60
30	34.74	274.52	147.59
31	72.93	295.74	159.00
32	-165.76	163.13	87.71
33	75.42	297.12	159.74
34	-35.28	235.62	126.68
35	56.86	286.81	154.20
36	-183.15	153.47	82.51
37	55.09	285.83	153.67
38	-47.80	228.67	122.94
39	[illegible].92	277.95	149.44
40	-195.54	146.59	78.81

Table A-5 (Cont.)

CYCLE NO. 9-780 CONT'D

PT. NO.	DEG F MODEL	DEG K MODEL	DEG K PROTOTYPE
41	40.41	277.67	149.29
42	-45.50	229.95	123.63
43	27.03	270.24	145.29
44	-204.59	141.56	76.11
45	26.51	269.95	145.13
46	-45.65	229.86	123.58
47	13.30	262.61	141.19
48	-198.85	144.75	77.82
49	11.15	261.42	140.55
50	-57.18	223.46	120.14
51	43.12	279.18	150.10
52	31.64	272.80	146.67
53	308.49	426.61	229.36
54	296.82	420.12	225.87
55	322.37	434.32	233.50
56	316.03	430.79	231.61
57	127.15	325.86	175.20
58	123.51	323.84	174.11
59	539.12	554.73	298.24
60	533.46	551.59	296.55
61	539.12	554.73	298.24
62	533.77	551.76	296.65
63	516.10	541.94	291.37
64	-131.74	182.03	97.87
65	-168.41	161.66	86.91
66	31.69	272.83	146.68
67	31.69	272.83	146.68
68	31.69	272.83	146.68
69	31.69	272.83	146.68
70	-104.27	197.29	106.07
71	72.40	295.44	158.84
72	57.41	287.12	154.36
73	48.99	282.44	151.85
74	71.38	294.88	158.54
75	58.05	287.47	154.55
76	51.82	284.01	152.69
77	72.93	295.74	159.00
78	58.86	287.92	154.80
79	49.22	282.57	151.92

Table A-6

CYCLE NO. 9-953 TIME FROM START MODEL: 953 sec
TIME FROM START PROTO: 24,800 sec

PT. NO.	DEG F MODEL	DEG K MODEL	DEG K PROTOTYPE
1	-40.94	232.48	124.99
2	-32.02	237.43	127.65
3	-53.19	225.67	121.33
4	-60.54	221.59	119.13
5	-50.80	227.00	122.04
6	-48.85	228.08	122.63
7	-58.24	222.86	119.82
8	-52.82	225.88	121.44
9	8.55	259.97	139.77
10	1.30	255.95	137.61
11	118.56	321.09	172.63
12	118.26	320.92	172.54
13	119.49	321.61	172.91
14	118.05	320.81	172.48
15	117.80	320.66	172.40
16	118.98	321.32	172.75
17	119.62	321.68	172.94
18	120.17	321.98	173.11
19	118.77	321.21	172.69
20	118.86	321.25	172.72
21	120.13	321.96	173.10
22	119.11	321.39	172.79
23	119.19	321.44	172.82
24	159.07	343.59	184.73
25	157.00	342.45	184.11
26	155.55	341.64	183.68
27	135.31	330.40	177.63
28	112.71	317.84	170.88
29	41.61	278.34	149.64
30	17.70	265.06	142.50
31	66.46	292.14	157.07
32	-127.09	184.62	99.26
33	68.74	293.41	157.75
34	-121.94	187.48	100.79
35	47.94	281.85	151.53
36	-144.65	174.86	94.01
37	45.87	280.71	150.92
38	-137.70	178.72	96.09
39	27.36	270.42	145.39
40	-154.18	169.56	91.16

Table A-6 (Cont.)

CYCLE NO. 9-953 CONT'D

PT. NO.	DEG F MODEL	DEG K MODEL	DEG K PROTOTYPE
41	26.56	269.98	145.15
42	-131.86	181.96	97.83
43	8.16	259.76	139.65
44	-143.18	175.68	94.45
45	7.25	259.25	139.38
46	-136.15	179.58	96.55
47	-14.10	247.39	133.00
48	-147.01	173.55	93.31
49	-13.75	247.58	133.11
50	-137.70	178.72	96.09
51	30.09	271.94	146.20
52	31.69	272.83	146.68
53	308.64	426.69	229.40
54	296.90	420.16	225.89
55	322.40	434.33	233.51
56	316.13	430.85	231.64
57	126.49	325.49	175.00
58	120.71	322.28	173.27
59	539.43	554.91	298.34
60	533.77	551.76	296.65
61	539.43	554.91	298.34
62	534.09	551.94	296.74
63	516.41	542.12	291.46
64	-135.84	179.76	96.64
65	-168.81	161.44	86.80
66	31.69	272.83	146.68
67	31.69	272.83	146.68
68	31.74	272.85	146.70
69	31.74	272.85	146.70
70	-98.10	200.72	107.91
71	66.41	292.12	157.05
72	49.27	282.59	151.93
73	40.05	277.47	149.18
74	65.47	291.59	156.77
75	49.95	282.97	152.14
76	42.75	278.97	149.99
77	67.00	292.44	157.23
78	50.68	283.38	152.35
79	40.23	277.57	149.23

Table A-7

CYCLE NO. 9-1128 TIME FROM START MODEL: 1,128 sec
TIME FROM START PROTO: 29,350 sec

PT. NO.	DEG F MODEL	DEG K MODEL	DEG K PROTOTYPE
1	-73.43	214.43	115.29
2	13.59	262.77	141.27
3	-76.30	212.83	114.43
4	-72.76	214.80	115.48
5	-37.88	234.18	125.90
6	-33.11	236.83	127.33
7	-69.29	216.73	116.52
8	-75.03	213.54	114.81
9	-13.15	247.92	133.29
10	-2.67	253.74	136.42
11	119.24	321.47	172.83
12	118.64	321.14	172.65
13	119.49	321.61	172.91
14	118.60	321.11	172.64
15	118.47	321.04	172.60
16	119.28	321.49	172.84
17	120.96	322.42	173.35
18	120.50	322.17	173.21
19	119.62	321.68	172.94
20	119.92	321.84	173.03
21	120.54	322.19	173.22
22	120.13	321.96	173.10
23	120.75	322.31	173.28
24	157.57	342.76	184.28
25	154.70	341.16	183.42
26	153.93	340.74	183.19
27	133.32	329.29	177.04
28	112.50	317.72	170.82
29	36.08	276.38	148.59
30	7.58	259.44	139.48
31	62.06	289.70	155.75
32	28.92	271.29	145.85
33	63.81	290.67	156.28
34	-154.58	169.35	91.05
35	41.83	278.46	149.71
36	31.60	272.78	146.65
37	40.09	277.50	149.19
38	-171.24	160.09	86.07
39	19.81	266.23	143.13
40	16.60	264.45	142.18

Table A-7 (Cont.)

CYCLE NO. 9-1128 CONT'D

PT. NO.	DEG F MODEL	DEG K MODEL	DEG K PROTOTYPE
41	18.04	265.24	142.60
42	-167.09	162.40	87.31
43	-0.30	255.06	137.13
44	50.45	283.25	152.29
45	-1.49	254.40	136.77
46	-171.17	160.13	86.09
47	-23.69	242.06	130.14
48	43.94	279.64	150.34
49	-18.40	245.00	131.72
50	-168.41	161.66	86.91
51	21.42	267.12	143.61
52	32.02	273.01	146.78
53	308.78	426.77	229.44
54	297.18	420.32	225.98
55	323.00	434.67	233.69
56	316.52	431.07	231.76
57	125.52	324.96	174.71
58	119.53	321.63	172.92
59	539.12	554.73	298.24
60	533.46	551.59	296.55
61	538.81	554.56	298.15
62	533.14	551.41	296.46
63	516.10	541.94	291.37
64	-139.88	177.51	95.44
65	-168.94	161.37	86.76
66	31.83	272.91	146.72
67	32.21	273.11	146.84
68	32.02	273.01	146.78
69	32.11	273.06	146.81
70	-44.29	230.61	123.99
71	60.76	288.98	155.37
72	42.02	278.57	149.77
73	32.16	273.09	146.82
74	59.68	288.38	155.04
75	42.61	278.90	149.94
76	35.26	274.81	147.75
77	61.30	289.28	155.53
78	43.12	279.18	150.10
79	32.91	273.51	147.05

Table A-8

CYCLE NO. 9-1302 TIME FROM START MODEL: 1,302 sec
TIME FROM START PROTO: 33,820 sec

PT. NO.	DEG F MODEL	DEG K MODEL	DEG K PROTOTYPE
1	348.16	448.64	241.21
2	87.64	303.91	163.39
3	147.34	337.08	181.22
4	-23.28	242.29	130.26
5	10.53	261.07	140.36
6	16.75	264.53	142.22
7	-19.50	244.39	131.39
8	151.78	339.55	182.55
9	-9.11	250.16	134.50
10	11.24	261.47	140.57
11	118.3[illegible]	320.95	172.55
12	118.90	321.28	172.73
13	119.49	321.61	172.91
14	118.69	321.16	172.67
15	118.90	321.28	172.73
16	119.45	321.58	172.89
17	121.26	322.59	173.43
18	120.84	322.35	173.31
19	119.75	321.75	172.98
20	120.21	322.01	173.12
21	120.84	322.35	173.31
22	120.42	322.12	173.18
23	120.92	322.40	173.33
24	156.15	341.97	183.86
25	153.24	340.35	182.99
26	152.19	339.77	182.67
27	131.83	328.46	176.59
28	110.04	316.36	170.08
29	33.76	273.98	147.30
30	4.20	257.56	138.47
31	58.41	287.67	154.66
32	103.68	312.82	168.18
33	59.95	288.53	155.12
34	-166.69	162.62	87.43
35	37.56	276.09	148.43
36	112.08	317.49	170.69
37	35.68	275.04	147.87
38	-185.31	152.27	81.87
39	19.47	266.04	143.03
40	94.46	307.70	165.43

Table A-8 (Cont.)

CYCLE NO. 9-1302 CONT'D

PT. NO.	DEG F MODEL	DEG K MODEL	DEG K PROTOTYPE
41	17.75	265.08	142.52
42	-181.96	154.13	2.87
43	13.78	262.88	141.33
44	130.08	327.49	176.07
45	11.67	261.71	140.70
46	-184.20	152.89	82.20
47	50.91	283.51	152.42
48	122.13	323.07	173.70
49	25.57	269.43	144.85
50	-172.69	159.28	85.64
51	21.42	267.12	143.61
52	32.25	273.14	146.85
53	308.60	426.67	229.39
54	297.18	420.32	225.98
55	322.58	434.43	233.57
56	316.63	431.13	231.79
57	125.73	325.07	174.77
58	118.64	321.14	172.65
59	534.72	552.29	296.93
60	532.52	551.06	296.27
61	538.18	554.21	297.96
62	532.83	551.24	296.37
63	514.83	541.24	290.99
64	-143.57	175.46	94.33
65	-169.54	161.04	86.58
66	32.16	273.09	146.82
67	32.16	273.09	146.82
68	32.21	273.11	146.84
69	32.25	273.14	146.85
70	-1.19	254.56	136.86
71	56.41	286.56	154.06
72	37.18	275.88	148.32
73	27.88	270.71	145.54
74	55.18	285.88	153.70
75	37.98	276.32	148.56
76	31.31	272.62	146.57
77	56.77	286.76	154.17
78	38.54	276.64	148.73
79	28.82	271.23	145.82

Table A-9

CYCLE NO. 9-1478 TIME FROM START MODEL: 1,478 sec
TIME FROM START PROTO: 38,400 sec

PT. NO.	DEG F MODEL	DEG K MODEL	DEG K PROTOTYPE
1	511.02	539.12	289.85
2	188.11	359.73	193.40
3	279.12	410.29	220.59
4	121.13	322.52	173.40
5	126.31	325.56	175.03
6	133.90	329.61	177.21
7	123.26	323.70	174.03
8	271.58	406.10	218.33
9	89.39	304.88	163.92
10	40.60	277.78	149.34
11	116.14	319.75	171.91
12	119.96	321.87	173.05
13	122.09	323.05	173.68
14	119.53	321.63	172.92
15	119.45	321.58	172.89
16	120.84	322.35	173.31
17	121.80	322.89	173.60
18	121.46	322.70	173.50
19	120.13	321.96	173.10
20	120.67	322.26	173.26
21	121.13	322.52	173.40
22	120.79	322.33	173.30
23	121.30	322.61	173.45
24	158.26	343.14	184.49
25	157.09	342.49	184.14
26	156.15	341.97	183.86
27	135.06	330.26	177.56
28	119.03	321.35	172.77
29	43.17	279.20	150.11
30	95.41	308.23	165.71
31	82.27	300.93	161.79
32	142.17	334.21	179.68
33	81.75	300.64	161.63
34	-171.17	160.13	86.09
35	73.78	296.21	159.25
36	152.02	339.68	182.62
37	73.56	296.09	159.19
38	-190.58	149.35	80.29
39	87.38	303.77	163.32
40	133.20	329.22	177.00

Table A-9 (Cont.)

CYCLE NO. 9-1478 CONT'D

PT. NO.	DEG F MODEL	DEG K MODEL	DEG K PROTOTYPE
41	88.38	304.32	163.62
42	-187.55	151.00	81.20
43	111.69	317.27	170.58
44	170.08	349.71	188.02
45	110.76	316.76	170.30
46	-185.45	152.19	81.82
47	153.64	340.58	183.11
48	162.45	345.47	185.74
49	127.53	326.07	175.31
50	-151.96	170.80	91.83
51	86.90	303.50	163.17
52	31.69	272.83	146.68
53	308.85	426.81	229.47
54	297.51	420.51	226.08
55	322.44	434.35	233.52
56	316.77	431.21	231.83
57	126.19	325.33	174.91
58	117.92	320.74	172.44
59	537.23	553.68	297.68
60	531.57	550.54	295.99
61	536.60	553.34	297.49
62	530.94	550.19	295.80
63	514.19	540.93	290.80
64	-146.11	174.05	93.57
65	-170.07	160.74	86.42
66	32.16	273.09	146.82
67	32.44	273.25	146.91
68	32.25	273.14	146.85
69	32.44	273.25	146.91
70	25.52	269.40	144.84
71	73.38	295.99	159.13
72	62.42	289.90	155.86
73	61.26	289.25	155.51
74	71.78	295.10	158.66
75	63.50	290.50	156.18
76	65.34	291.52	156.73
77	73.51	296.06	159.17
78	64.35	290.97	156.44
79	34.46	274.37	147.51

Table A-10

CYCLE NO. 9-1650 TIME FROM START MODEL: 1,670 sec
TIME FROM START PROTO: 42,900 sec

PT. NO.	DEG F MODEL	DEG K MODEL	DEG K PROTOTYPE
1	115.38	319.32	171.68
2	156.28	342.04	183.89
3	57.64	287.24	154.43
4	21.42	267.12	143.61
5	61.84	289.58	155.69
6	68.39	293.21	157.64
7	24.53	268.85	144.54
8	55.45	286.03	153.78
9	48.62	282.24	151.74
10	14.40	263.22	141.52
11	118.77	321.21	172.69
12	120.13	321.96	173.10
13	120.79	322.33	173.30
14	119.83	321.79	173.01
15	119.75	321.75	172.98
16	120.17	321.98	173.11
17	122.01	323.00	173.66
18	121.72	322.84	173.57
19	120.46	322.14	173.20
20	121.17	322.54	173.41
21	121.42	322.68	173.48
22	121.00	322.45	173.36
23	121.59	322.77	173.53
24	161.93	345.18	185.58
25	160.24	344.24	185.08
26	159.39	343.77	184.82
27	136.60	331.11	178.02
28	122.80	323.45	173.90
29	56.86	286.81	154.20
30	51.86	284.04	152.71
31	82.18	300.88	161.76
32	159.72	343.95	184.92
33	82.84	301.24	161.96
34	-177.17	156.79	84.30
35	68.79	293.44	157.76
36	169.80	349.56	187.93
37	66.91	292.39	157.20
38	-197.91	145.27	78.10
39	58.05	287.47	154.55
40	150.04	338.58	182.03

Table A-10 (Cont.)

CYCLE NO. 9-1650 CONT'D

PT. NO.	DEG F MODEL	DEG K MODEL	DEG K PROTOTYPE
41	56.41	286.56	154.06
42	-195.90	146.39	78.70
43	49.04	282.46	151.86
44	187.01	359.12	193.07
45	47.25	281.47	151.33
46	-195.68	146.51	78.77
47	39.95	277.42	149.15
48	180.20	355.33	191.04
49	37.65	276.14	148.46
50	-173.72	158.71	85.33
51	58.14	287.52	154.58
52	32.25	273.14	146.85
53	309.07	426.93	229.53
54	297.83	420.69	226.18
55	322.51	434.39	233.55
56	316.84	431.25	231.85
57	127.15	325.86	175.20
58	117.20	320.34	172.22
59	536.92	553.51	297.59
60	531.26	550.37	295.90
61	537.23	553.68	297.68
62	531.57	550.54	295.99
63	513.87	540.71	290.70
64	-149.43	172.21	92.58
65	-170.41	160.55	86.32
66	32.30	273.17	146.86
67	32.30	273.17	146.86
68	32.35	273.19	146.88
69	32.35	273.19	146.88
70	38.92	276.84	148.84
71	79.87	299.59	161.07
72	68.07	293.04	157.55
73	63.05	290.25	156.05
74	78.76	298.98	160.74
75	68.74	293.41	157.75
76	66.23	292.02	157.00
77	80.09	299.72	161.14
78	69.06	293.59	157.84
79	63.50	290.50	156.18

Table A-11

CYCLE NO. 9-1995 TIME FROM START MODEL: 1,995 sec
TIME FROM START PROTO: 51,900 sec

PT. NO.	DEG F MODEL	DEG K MODEL	DEG K PROTOTYPE
1	-49.74	227.59	122.36
2	89.91	305.17	164.07
3	-58.51	222.72	119.74
4	-53.03	225.76	121.38
5	3.33	257.07	138.21
6	9.28	260.38	139.99
7	-48.38	228.35	122.77
8	-56.60	223.78	120.31
9	-22.12	242.93	130.61
10	-37.93	234.15	125.89
11	119.58	321.65	172.93
12	119.87	321.82	173.02
13	120.42	322.12	173.18
14	119.70	321.72	172.97
15	119.53	321.63	172.92
16	120.33	322.07	173.16
17	121.92	322.96	173.63
18	121.88	322.93	173.62
19	120.46	322.14	173.20
20	121.21	322.56	173.42
21	121.30	322.61	173.45
22	121.21	322.56	173.42
23	121.55	322.75	173.52
24	157.69	342.83	184.32
25	155.38	341.55	183.63
26	154.53	341.07	183.37
27	133.24	329.24	177.01
28	116.78	320.10	172.10
29	45.18	280.32	150.71
30	4.40	257.66	138.53
31	64.17	290.87	156.38
32	126.49	325.49	175.00
33	65.47	291.59	156.77
34	-183.85	153.09	82.30
35	44.08	279.71	150.38
36	135.52	330.51	177.69
37	42.02	278.57	149.77
38	-206.52	140.49	75.53
39	20.94	266.86	143.47
40	116.23	319.79	171.93

Table A-11 (Cont.)

CYCLE NO. 9-1995 CONT'D

PT. NO.	DEG F MODEL	DEG K MODEL	DEG K PROTOTYPE
41	18.61	265.56	142.78
42	-205.33	141.15	75.89
43	-0.94	254.70	136.94
44	149.14	338.08	181.76
45	-2.52	253.82	136.46
46	-206.07	140.74	75.66
47	-26.21	240.66	129.39
48	142.95	334.64	179.91
49	-20.40	243.89	131.12
50	-193.74	147.59	79.35
51	22.36	267.64	143.89
52	31.92	272.96	146.75
53	308.28	426.49	229.29
54	297.11	420.28	225.96
55	321.66	433.92	233.29
56	315.99	430.77	231.60
57	127.53	326.07	175.31
58	115.81	319.56	171.81
59	536.60	553.34	297.49
60	530.94	550.19	295.80
61	537.23	553.68	297.68
62	531.57	550.54	295.99
63	513.56	540.53	290.61
64	-155.82	168.66	90.68
65	-171.86	159.74	85.88
66	32.16	273.09	146.82
67	32.07	273.04	146.79
68	32.25	273.14	146.85
69	32.16	273.09	146.82
70	24.95	269.08	144.67
71	63.81	290.67	156.28
72	45.41	280.45	150.78
73	36.67	275.59	148.17
74	62.56	289.98	155.90
75	46.28	280.94	151.04
76	39.53	277.18	149.02
77	64.04	290.80	156.34
78	46.51	281.06	151.11
79	37.09	275.83	148.29

Table A-12

CYCLE NO. 9-2165 TIME FROM START MODEL: 2,165 sec
TIME FROM START PROTO: 56,400 sec

PT. NO.	DEG F MODEL	DEG K MODEL	DEG K PROTOTYPE
1	-76.35	212.80	114.41
2	58.14	287.52	154.58
3	-79.61	210.99	113.44
4	-68.70	217.06	116.70
5	-16.90	245.83	132.17
6	-12.75	248.14	133.41
7	-64.08	219.62	118.08
8	-77.02	212.44	114.21
9	-43.98	230.79	124.08
10	-55.43	224.43	120.66
11	119.79	321.77	173.00
12	119.96	321.87	173.05
13	120.92	322.40	173.33
14	119.62	321.68	172.94
15	119.28	321.49	172.84
16	120.59	322.21	173.23
17	121.88	322.93	173.62
18	121.84	322.91	173.61
19	120.25	322.03	173.13
20	121.17	322.54	173.41
21	121.17	322.54	173.41
22	121.00	322.45	173.36
23	121.46	322.70	173.50
24	155.18	341.43	183.57
25	153.04	340.24	182.93
26	151.82	339.57	182.56
27	131.45	328.25	176.48
28	112.84	317.91	170.92
29	37.65	276.14	148.46
30	-7.13	251.26	135.09
31	57.09	286.94	154.27
32	79.56	299.42	160.98
33	58.50	287.72	154.69
34	-186.22	151.76	81.59
35	35.45	274.91	147.80
36	87.86	304.03	163.46
37	33.10	273.61	147.10
38	-209.41	138.88	74.67
39	10.57	261.10	140.37
40	69.42	293.79	157.95

Table A-12 (Cont.)

CYCLE NO. 9-2165 CONT'D

PT. NO.	DEG F MODEL	DEG K MODEL	DEG K PROTOTYPE
41	8.12	259.73	139.64
42	-208.89	139.17	74.82
43	-13.15	247.92	133.29
44	97.14	309.19	166.23
45	-15.25	246.75	132.66
46	-209.56	138.80	74.62
47	-40.99	232.45	124.97
48	92.38	306.54	164.81
49	-35.80	235.33	126.52
50	-199.14	144.59	77.74
51	12.44	262.13	140.93
52	31.83	272.91	146.72
53	307.78	426.21	229.15
54	296.68	420.04	225.83
55	321.13	433.63	233.13
56	315.67	430.60	231.50
57	126.65	325.58	175.05
58	115.38	319.32	171.68
59	536.92	553.51	297.59
60	531.26	550.37	295.90
61	537.55	553.86	297.77
62	531.89	550.71	296.08
63	513.56	540.53	290.61
64	-158.63	167.10	89.84
65	-172.55	159.36	85.68
66	32.02	273.01	146.78
67	32.11	273.06	146.81
68	32.07	273.04	146.79
69	32.07	273.04	146.79
70	1.69	256.16	137.72
71	56.18	286.43	154.00
72	36.24	275.36	148.04
73	27.12	270.29	145.32
74	55.00	285.78	153.64
75	36.95	275.75	148.25
76	30.00	271.89	146.18
77	56.59	286.66	154.12
78	37.32	275.96	148.36
79	27.26	270.37	145.36

Table A-13

CYCLE NO. 9-2340 TIME FROM START MODEL: 2,340 sec
TIME FROM START PROTO: 60,900 sec

PT. NO.	DEG F MODEL	DEG K MODEL	DEG K PROTOTYPE
1	-88.37	206.13	110.82
2	0.72	255.62	137.43
3	-93.10	203.50	109.41
4	-86.07	207.41	111.51
5	-49.69	227.62	122.38
6	-46.54	229.36	123.31
7	-81.69	209.84	112.82
8	-90.40	205.00	110.21
9	-63.80	219.78	118.16
10	-71.99	215.23	115.71
11	119.75	321.75	172.98
12	119.83	321.79	173.01
13	120.84	322.35	173.31
14	119.45	321.58	172.89
15	119.24	321.47	172.83
16	120.50	322.17	173.21
17	121.59	322.77	173.53
18	121.97	322.98	173.65
19	120.25	322.03	173.13
20	120.75	322.31	173.28
21	120.88	322.38	173.32
22	121.13	322.52	173.40
23	121.13	322.52	173.40
24	153.12	340.29	182.95
25	150.97	339.10	182.31
26	149.63	338.35	181.91
27	129.96	327.42	176.03
28	108.59	315.55	169.65
29	30.38	272.10	146.29
30	-17.30	245.61	132.05
31	50.82	283.45	152.39
32	15.79	263.99	141.93
33	52.45	284.36	152.88
34	-188.04	150.75	81.05
35	27.74	270.63	145.50
36	20.71	266.73	143.40
37	25.33	269.29	144.78
38	-212.37	137.24	73.79
39	1.26	255.92	137.59
40	3.24	257.02	138.18

Table A-13 (Cont.)

CYCLE NO. 9-2340 CONT'D

PT. NO.	DEG F MODEL	DEG K MODEL	DEG K PROTOTYPE
41	-1.44	254.42	136.79
42	-212.06	137.41	73.88
43	-24.80	241.45	129.81
44	22.78	267.88	144.02
45	-27.07	240.18	129.13
46	-212.75	137.03	73.67
47	-55.43	224.43	120.66
48	20.24	266.46	143.26
49	-52.87	225.85	121.42
50	-203.63	142.09	76.39
51	3.33	257.07	138.21
52	31.83	272.91	146.72
53	307.31	425.95	229.01
54	296.17	419.76	225.68
55	320.35	433.20	232.90
56	315.43	430.46	231.43
57	125.27	324.82	174.63
58	114.75	318.97	171.49
59	536.29	553.16	297.40
60	531.57	550.54	295.99
61	538.18	554.21	297.96
62	532.52	551.06	296.27
63	513.87	540.71	290.70
64	-161.39	165.56	89.01
65	-173.52	158.82	85.39
66	31.74	272.85	146.70
67	31.69	272.83	146.68
68	31.83	272.91	146.72
69	31.83	272.91	146.72
70	-28.59	239.34	128.68
71	49.68	282.82	152.05
72	28.40	271.00	145.70
73	18.80	265.67	142.83
74	48.44	282.13	151.68
75	29.06	271.36	145.90
76	21.70	267.28	143.70
77	49.95	282.97	152.14
78	29.39	271.55	145.99
79	18.95	265.75	142.88

Table A-14

CYCLE NO. 9-2515 TIME FROM START MODEL: 2,515 sec
TIME FROM START PROTO: 65,400 sec

PT. NO.	DEG F MODEL	DEG K MODEL	DEG K PROTOTYPE
1	-87.75	206.47	111.01
2	-53.78	225.35	121.15
3	-100.29	199.50	107.26
4	-104.09	197.39	106.12
5	-83.03	209.09	112.42
6	-80.56	210.47	113.15
7	-99.89	199.73	107.38
8	-97.76	200.91	108.02
9	-82.25	209.53	112.65
10	-87.87	206.41	110.97
11	119.32	321.51	172.86
12	119.62	321.68	172.94
13	120.50	322.17	173.21
14	119.32	321.51	172.86
15	119.03	321.35	172.77
16	120.50	322.17	173.21
17	121.09	322.49	173.38
18	121.67	322.82	173.56
19	119.83	321.79	173.01
20	120.42	322.12	173.18
21	120.59	322.21	173.23
22	120.67	322.26	173.26
23	120.71	322.28	173.27
24	151.34	339.30	182.42
25	149.14	338.08	181.76
26	147.42	337.12	181.25
27	128.49	326.61	175.60
28	105.26	313.70	168.65
29	23.25	268.14	144.16
30	-26.92	240.27	129.18
31	44.86	280.15	150.62
32	-93.05	203.53	109.42
33	47.16	281.42	151.30
34	-137.02	179.10	96.29
35	20.47	266.60	143.33
36	-93.68	203.18	109.24
37	17.89	265.16	142.56
38	-153.20	170.11	91.46
39	-6.73	251.48	135.21
40	-104.91	196.94	105.88

Table A-14 (Cont.)

CYCLE NO. 9-2515 CONT'D

PT. NO.	DEG F MODEL	DEG K MODEL	DEG K PROTOTYPE
41	-10.20	249.56	134.17
42	-156.47	168.29	90.48
43	-35.85	235.30	126.51
44	-103.45	197.75	106.32
45	-38.13	234.04	125.83
46	-158.04	167.42	90.01
47	-68.53	217.15	116.75
48	-101.23	198.98	106.98
49	-67.88	217.51	116.94
50	-159.74	166.48	89.50
51	-5.25	252.31	135.65
52	31.64	272.80	146.67
53	306.81	425.67	228.86
54	295.70	419.50	225.54
55	319.93	432.96	232.77
56	315.14	430.30	231.34
57	123.77	323.98	174.18
58	114.75	318.97	171.49
59	537.86	554.03	297.87
60	532.20	550.89	296.18
61	538.81	554.56	298.15
62	533.14	551.41	296.46
63	514.51	541.06	290.89
64	-164.17	164.02	88.18
65	-174.34	158.36	85.14
66	31.60	272.78	146.65
67	31.69	272.83	146.68
68	31.64	272.80	146.67
69	31.64	272.80	146.67
70	-66.90	218.05	117.23
71	43.76	279.53	150.29
72	20.99	266.88	143.49
73	11.05	261.36	140.52
74	42.48	278.82	149.90
75	21.84	267.36	143.74
76	14.02	263.01	141.40
77	44.22	279.79	150.42
78	22.64	267.80	143.98
79	11.58	261.65	140.67

Table A-15

CYCLE NO. 9-2690 TIME FROM START MODEL: 2,690 sec
TIME FROM START PROTO: 70,000 sec

PT. NO.	DEG F MODEL	DEG K MODEL	DEG K PROTOTYPE
1	-31.19	237.89	127.90
2	-96.38	201.68	108.43
3	-72.32	215.04	115.62
4	-108.65	194.86	104.76
5	-107.54	195.48	105.09
6	-105.03	196.87	105.85
7	-105.09	196.84	105.83
8	-70.83	215.87	116.06
9	-94.37	202.80	109.03
10	-99.71	199.83	107.43
11	119.41	321.56	172.88
12	119.70	321.72	172.97
13	120.00	321.89	173.06
14	119.36	321.54	172.87
15	119.15	321.42	172.81
16	120.08	321.94	173.08
17	121.26	322.59	173.43
18	121.76	322.87	173.58
19	119.92	321.84	173.03
20	120.67	322.26	173.26
21	120.75	322.31	173.28
22	120.79	322.33	173.30
23	120.79	322.33	173.30
24	150.00	338.56	182.02
25	148.20	337.55	181.48
26	146.23	336.46	180.89
27	128.83	326.79	175.70
28	104.15	313.08	168.32
29	16.56	264.42	142.16
30	-33.58	236.57	127.19
31	40.46	277.70	149.30
32	-133.60	181.00	97.31
33	43.53	279.41	150.22
34	26.32	269.84	145.08
35	15.07	263.60	141.72
36	-142.55	176.03	94.64
37	12.54	262.19	140.96
38	18.61	265.56	142.78
39	-14.25	247.31	132.96
40	-152.09	170.73	91.79

Table A-15 (Cont.)

CYCLE NO. 9-2690 CONT'D

PT. NO.	DEG F MODEL	DEG K MODEL	DEG K PROTOTYPE
41	-16.45	246.08	132.30
42	14.64	263.36	141.59
43	-42.62	231.55	124.49
44	-156.47	168.29	90.48
45	-44.82	230.32	123.83
46	22.78	267.88	144.02
47	-72.32	215.04	115.62
48	-152.29	170.62	91.70
49	-74.75	213.69	114.89
50	4.11	257.50	138.44
51	-11.75	248.69	133.71
52	31.97	272.98	146.77
53	306.85	425.69	228.87
54	295.78	419.54	225.56
55	320.46	433.26	232.93
56	314.93	430.18	231.28
57	123.39	323.77	174.07
58	115.38	319.32	171.68
59	538.49	554.38	298.06
60	532.83	551.24	296.37
61	539.43	554.91	298.34
62	533.46	551.59	296.55
63	515.14	541.41	291.08
64	-163.97	164.13	88.24
65	-174.48	158.29	85.10
66	32.11	273.06	146.81
67	32.02	273.01	146.78
68	31.88	272.93	146.74
69	32.07	273.04	146.79
70	-84.10	208.50	112.10
71	39.01	276.90	148.87
72	15.17	263.65	141.75
73	4.83	257.91	138.66
74	37.70	276.17	148.48
75	16.22	264.23	142.06
76	7.87	259.60	139.57
77	39.39	277.11	148.98
78	16.70	264.50	142.20
79	5.17	258.09	138.76

Table A-16

CYCLE NO. 9-2860 TIME FROM START MODEL: 2,860 sec
TIME FROM START PROTO: 74,500 sec

PT. NO.	DEG F MODEL	DEG K MODEL	DEG K PROTOTYPE
1	31.97	272.98	146.77
2	-106.43	196.09	105.43
3	-32.85	236.97	127.40
4	-96.67	201.52	108.34
5	-111.80	193.11	103.82
6	-109.47	194.40	104.52
7	-94.02	202.99	109.13
8	-33.16	236.80	127.31
9	-97.82	200.88	108.00
10	-105.03	196.87	105.85
11	134.98	330.21	0 177.53
12	120.21	322.01	173.12
13	119.66	321.70	172.96
14	119.45	321.58	172.89
15	119.15	321.42	172.81
16	97.71	309.50	166.40
17	120.75	322.31	173.28
18	122.13	323.07	173.70
19	119.92	321.84	173.03
20	120.68	322.33	173.32
21	120.67	322.26	[illegible]
22	120.84	322.35	173.31
23	120.86	322.36	173.32
24	149.51	338.28	181.87
25	147.25	337.03	181.20
26	145.37	335.98	180.64
27	129.50	327.17	175.90
28	101.03	311.35	167.39
29	10.86	261.26	140.46
30	-36.17	235.13	126.41
31	37.51	276.06	148.42
32	-147.13	173.48	93.27
33	41.38	278.21	149.57
34	126.44	325.47	174.98
35	11.67	261.71	140.70
36	-159.54	166.59	89.56
37	9.86	260.70	140.16
38	118.90	321.28	172.73
39	-17.30	245.61	132.05
40	-168.34	161.70	86.93

Table A-16 (Cont.)

CYCLE NO. 9-2860 CONT'D

PT. NO.	DEG F MODEL	DEG K MODEL	DEG K PROTOTYPE
41	-19.05	244.64	131.53
42	116.91	320.17	172.13
43	-43.25	231.20	124.30
44	-175.59	157.67	84.77
45	-45.13	230.15	123.74
46	123.31	323.73	174.05
47	-65.16	219.02	117.75
48	-172.07	159.63	85.82
49	-71.49	215.50	115.86
50	98.10	309.72	166.52
51	-14.60	247.11	132.86
52	32.02	273.01	146.78
53	306.95	425.75	228.90
54	295.70	419.50	225.54
55	320.78	433.43	233.03
56	314.72	430.06	231.22
57	123.01	323.56	173.96
58	118.05	320.81	172.48
59	539.75	555.08	298.43
60	534.09	551.94	296.74
61	540.69	555.61	298.71
62	535.03	552.46	297.02
63	516.10	541.94	291.37
64	-159.74	166.48	89.50
65	-174.41	158.33	85.12
66	32.11	273.06	146.81
67	32.21	273.11	146.84
68	32.35	273.19	146.88
69	32.11	273.06	146.81
70	-91.61	204.33	109.85
71	35.40	274.89	147.79
72	11.44	261.58	140.63
73	0.53	255.52	137.37
74	34.13	274.18	147.41
75	11.91	261.84	140.77
76	3.33	257.07	138.21
77	35.96	275.20	147.96
78	12.39	262.11	140.92
79	0.63	255.57	137.40

Table A-17

CYCLE NO. 9-3040 TIME FROM START MODEL: 3,040 sec
TIME FROM START PROTO: 79,000 sec

PT. NO.	DEG F MODEL	DEG K MODEL	DEG K PROTOTYPE
1	75.20	297.00	159.68
2	-111.14	193.48	104.02
3	-4.11	252.94	135.99
4	-81.52	209.94	112.87
5	-103.80	197.55	106.21
6	-101.23	198.98	106.98
7	-79.01	211.33	113.62
8	-5.45	252.20	135.59
9	-94.43	202.76	109.01
10	-104.27	197.29	106.07
11	116.99	320.22	172.16
12	120.25	322.03	173.13
13	121.13	322.52	173.40
14	119.36	321.54	172.87
15	119.24	321.47	172.83
16	131.95	328.53	176.63
17	121.63	322.80	173.55
18	122.26	323.14	173.73
19	120.25	322.03	173.13
20	121.05	322.47	173.37
21	121.09	322.49	173.38
22	120.96	322.42	173.35
23	121.13	322.52	173.40
24	149.10	338.05	181.75
25	146.97	336.87	181.11
26	144.88	335.71	180.49
27	130.00	327.44	176.05
28	99.91	310.73	167.06
29	6.52	258.85	139.16
30	-35.34	235.59	126.66
31	36.24	275.36	148.04
32	-153.53	169.93	91.36
33	40.14	277.52	149.20
34	170.48	349.93	188.14
35	10.24	260.91	140.27
36	-167.55	162.14	87.17
37	7.92	259.62	139.58
38	161.97	345.20	185.59
39	-17.50	245.50	131.99
40	-177.03	156.87	84.34

Table A-17 (Cont.)

CYCLE NO. 9-3040 CONT'D

PT. NO.	DEG F MODEL	DEG K MODEL	DEG K PROTOTYPE
41	-18.95	244.69	131.56
42	160.64	344.47	185.20
43	-40.31	232.83	125.17
44	-185.45	152.19	81.82
45	-42.36	231.69	124.57
46	165.62	347.23	186.69
47	-54.68	224.84	120.88
48	-183.01	153.55	82.55
49	-63.91	219.71	118.13
50	139.46	332.70	178.87
51	-14.90	246.94	132.77
52	32.16	273.09	146.82
53	306.99	425.77	228.91
54	295.60	419.44	225.51
55	320.92	433.51	233.07
56	314.72	430.06	231.22
57	123.77	323.98	174.18
58	121.63	322.80	173.55
59	539.43	554.91	298.34
60	533.46	551.59	296.55
61	540.06	555.26	298.53
62	533.77	551.76	296.65
63	516.10	541.94	291.37
64	-153.53	169.93	91.36
65	-173.86	158.63	85.29
66	32.25	273.14	146.85
67	32.30	273.17	146.86
68	32.25	273.14	146.85
69	32.21	273.11	146.84
70	-96.21	201.77	108.48
71	33.33	273.74	147.17
72	8.94	260.19	139.89
73	-2.23	253.98	136.55
74	32.07	273.04	146.79
75	9.61	260.56	140.09
76	0.92	255.73	137.49
77	33.80	274.00	147.31
78	10.05	260.80	140.22
79	-2.03	254.09	136.61

Table A-18

CYCLE NO. 9-3210 TIME FROM START MODEL: 3,210 sec
TIME FROM START PROTO: 83,500 sec

PT. NO.	DEG F MODEL	DEG K MODEL	DEG K PROTOTYPE
1	98.40	309.89	166.61
2	-95.17	202.35	108.79
3	12.82	262.35	141.05
4	-69.62	216.54	116.42
5	-92.07	204.07	109.72
6	-89.16	205.69	110.59
7	-67.39	217.78	117.09
8	11.34	261.52	140.60
9	-87.58	206.56	111.06
10	-100.41	199.44	107.23
11	116.44	319.91	172.00
12	120.25	322.03	173.13
13	122.09	323.05	173.68
14	119.36	321.54	172.87
15	119.32	321.51	172.86
16	121.46	322.70	173.50
17	121.42	322.68	173.48
18	122.26	323.14	173.73
19	120.13	321.96	173.10
20	120.84	322.35	173.31
21	121.09	322.49	173.38
22	121.00	322.45	173.36
23	120.88	322.38	173.32
24	148.28	337.60	181.50
25	146.52	336.62	180.98
26	144.75	335.64	180.45
27	130.87	327.93	176.31
28	98.87	310.15	166.75
29	3.38	257.10	138.23
30	-32.90	236.94	127.39
31	35.68	275.04	147.87
32	-157.19	167.89	90.27
33	40.00	277.44	149.16
34	190.78	361.21	194.20
35	9.90	260.72	140.17
36	-172.41	159.44	85.72
37	7.73	259.52	139.52
38	182.13	356.40	191.61
39	-16.40	246.11	132.32
40	-182.24	153.98	82.78

Table A-18 (Cont.)

CYCLE NO. 9-3210 CONT'D

PT. NO.	DEG F MODEL	DEG K MODEL	DEG K PROTOTYPE
41	-17.45	245.53	132.00
42	180.12	355.29	191.01
43	-35.85	235.30	126.51
44	-191.58	148.79	79.99
45	-38.19	234.01	125.81
46	185.12	358.07	192.51
47	-45.65	229.86	123.58
48	-189.93	149.71	80.49
49	-56.28	223.96	120.41
50	157.81	342.90	184.35
51	-13.50	247.72	133.18
52	32.25	273.14	146.85
53	307.06	425.81	228.93
54	295.60	419.44	225.51
55	321.13	433.63	233.13
56	314.82	430.12	231.25
57	125.40	324.89	174.67
58	125.27	324.82	174.63
59	539.12	554.73	298.24
60	533.46	551.59	296.55
61	539.43	554.91	298.34
62	533.46	551.59	296.55
63	515.78	541.77	291.27
64	-145.86	174.19	93.65
65	-172.90	159.17	85.57
66	32.35	273.19	146.88
67	32.30	273.17	146.86
68	32.35	273.19	146.88
69	32.35	273.19	146.88
70	-98.91	200.27	107.67
71	32.35	273.19	146.88
72	7.87	259.60	139.57
73	-3.61	253.21	136.14
74	30.75	272.31	146.40
75	8.41	259.89	139.73
76	-0.45	254.97	137.08
77	33.00	273.56	147.07
78	9.32	260.40	140.00
79	-2.97	253.57	136.33

PALO ALTO RESEARCH LABORATORY
MISSILES & SPACE COMPANY
DIVISION OF LOCKHEED AIRCRAFT CORPORATION